Fatigue Analysis of Discharge Area of 26kl Tank Container under Railway Transportation

Shuo Zhang

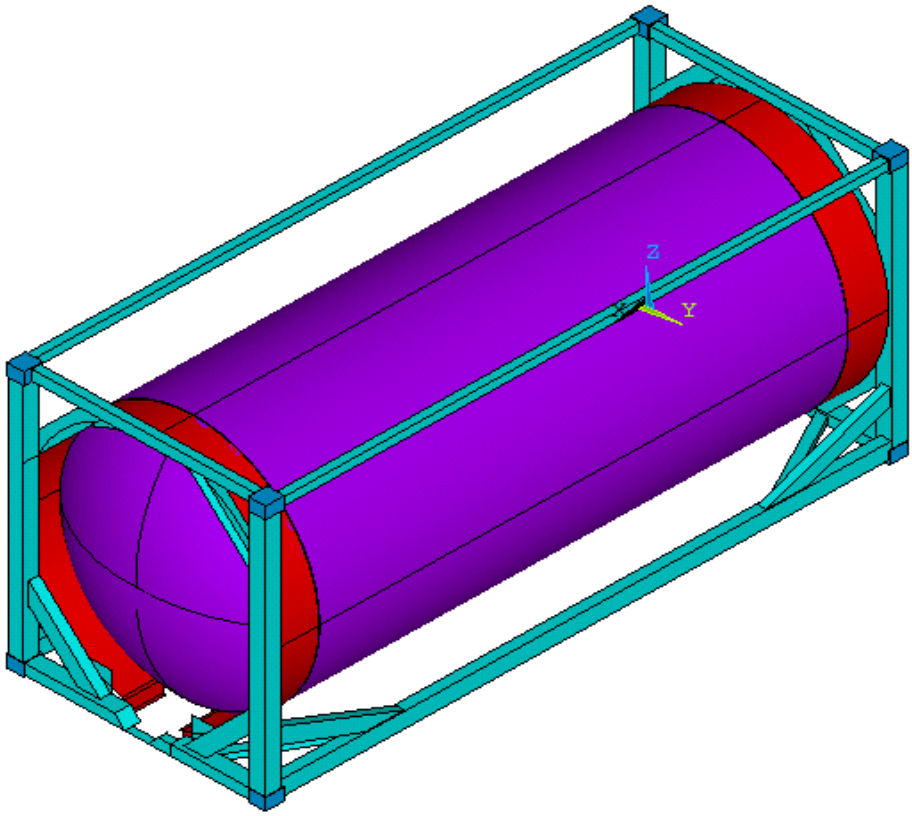

TU Delft

TRIFLEET
LEASING EXCELLENCE

Fatigue analysis of discharge area of 26kl tank container under railway transportation

By

Shuo Zhang

in partial fulfilment of the requirements for the degree of

Master of Science
in Faculty of Mechanical, Maritime and Materials Engineering

at the Delft University of Technology,
to be defended publicly on Wednesday May 30, 2018 at 10:00 AM.

Supervisor:	Dr. ing. A. Romeijn	TU Delft
Thesis committee:	Dr. C. (Christos) Kassapoglou	TU Delft
	Dr.Ir. J.H. den Besten	TU Delft
	Patrick Broeders	Trifleet leasing

Preface

This thesis work, as part of the project ‘Strength Analysis of 26k NT Tank’, was initiated by a previous student Ji Bao and later taken over by me. In this thesis, I tried to combine theoretical knowledge of fatigue and FEM modelling technique to calculate fatigue damage for designated hotspots as well as to improve the existing work done by the previous student. This thesis has been written to obtain the long-awaited and much anticipated degree of Master of Science at the Delft University of Technology.

I would like to express my gratitude to many people without whose help I wouldn’t be able to finish my study. First of all, I’d like to thank Professor Arie Romeijn for providing me with guidance and encouragement whenever I was stuck with my work. Secondly, a special acknowledgment goes out to Mr. Patrick Broeders, who brought this thesis project to me and helped me realize my shortcomings during my work. I would also like to thank Ji Bao for his work and his help during the master study, Xiaozhe Wang for his helpfulness, all my colleagues for their kindness. Last but not least, I want to thank my parents for supporting me no matter what happened. I hope they are proud of me now.

Table of Contents

List of Figures

List of Tables

Abstract

Tank containers are intermodal containers for the transport of liquids, gases, and powders as bulk cargo However, hazardous vibration during transportation would generate fatigue damage at discharge area. This thesis aims at calculating fatigue damage at discharge area of a specified tank container.

The calculation is performed in time domain. With FEM models and measured input, hot spot stress is calculated for each hot spot. Probability distributions projects the stress distribution to a longer period thus fatigue damage for 20 years is calculated.

The available data consists of acceleration and velocity of the container during a typical train transportation. A global model and a local model are established with FEM software package. Experimental data from the Lloyd register are used to verify the global model.

In conclusion, during the typical transportation period, fatigue will occur at one of the hotspots.

Chapter 1 Introduction

1.1 Motivation

Tank containers are intermodal containers for the transport of liquids, gases, and powders as bulk cargo. Tank containers should be manufactured according to ISO standards. Due to its high reliability, high level of safety and cost-effectiveness, tank container is one of the most popular way of transportation.

A tank container mainly consists of two important structural parts, namely the vessel and the frame. The vessel is typically made of stainless steel surrounded by insulation and protection layer. It sits in the middle of steel frames. The vessel and the frame are connected by skirt panels through welding. The size of tank containers varies with their capability. According to ISO standards, a 26000litre(26kl) IMO-1 UN portable tank is normally 6059mm in length, 2438mm in width and 2591mm in height. The tank container of interest in this thesis is a 26kl NT tank container. Figure 1-1 shows an example of tank container. Details of this tank container and FEM model will be listed in chapter 4.

Figure 1- 1 Example of tank containers

Although a lot of research have been carried out by previous scholars, most of them focus on the fatigue theory and the analytical solution of fatigue calculation, resulting in a lack of applicable calculation examples in engineering field, especially in the field of tank containers. Trifleet Leasing, as the world's largest privately owned and owner-managed global tank container leasing company initiated this project and completed the first stage of the project in 2016 with a master student Ji Bao. To solve the remainder of problems and overcome the limitations of Ji's work, this thesis was initiated.

1.2 Scope of work

Fatigue of tank container induced by vibration in railway transportation is a complicated topic. Fatigue life estimation can be affected by several factors. To name a few, modelling of the structure, choice of stress component, etc. Different results will be reached by various approaches. The aim of this thesis is to gain insight about the origin of fatigue in railway transportation, i.e. the vertical acceleration induced by different road conditions and come up with a calculation process for fatigue life of designated hotspots.

The thesis consists of the following work:
An investigation of vertical acceleration of railway transportation under different rail/wheel conditions.
A calculation of fatigue life of discharge area of the tank container.
An estimation of fatigue life of the tank container under combined utility (road transportation and railway transportation).

1.3 Outline of work

In chapter 2 fundamentals of fatigue and fracture is introduced. It describes crack initiation period and fatigue propagation period, hot spot stress method, rain-flow counting method, S-N curves, the Miner's rule and a few other related concepts. Chapter 3 lists a few calculations for the vertical acceleration based on railway transportation. Chapter 4 demonstrates the results of static loading tests according to ISO standards, which are used as verifications for the ANSYS model of the tank container. Chapter 5 illustrates detailed calculation of fatigue damage on a few designated hot spots. Chapter 6 lists several other works that are based on this thesis, and recommendations on future improvement. Figures and tables of interest will be listed in the chapters and extra information will be listed in appendix.

Chapter 2 Fundamentals about Fatigue

2.1 Fatigue of structure

Fatigue failures in metallic structures are a well-known technical problem. When a specimen or structure is exposed to cyclic loads, a fatigue crack nucleus can be initiated on a microscopically small scale. After that the crack will gradually grow to a macroscopic size. In the end the specimen or structure will fail at the last cycle of fatigue life.

Fatigue can occur even if the stress amplitude is significantly lower than the yielding stress, which applies to most encountered conditions, where the tank container is transported under mild and moderate vibrations. Hence it is of great importance to study the structural response from the perspective of fatigue.

In general, fatigue crack nuclei are more prone to be initiated at surface of specimen. However, in a welded structure, fatigue can also start from welded joints mainly for two reasons. On the one hand, imperfections in welding makes it easier for nuclei to initiate. Fatigue crack initiation is more likely to initiate from imperfections as resistance is lower. On the other hand, welded structures usually have the maximum mean stress level, making the weld joint a favorable location for cracks to start from.

Fatigue is typically divided into two periods: crack initiation period and crack growth period. At the beginning, cyclic loading introduces slip bands on the surface of the specimen. Crack nuclei start in slip bands as soon as a cyclic stress is above fatigue limit. Micro cracks will occur at nucleation site but remain invisible for a large part of total fatigue life. The period of micro crack growth is slow and erratic until some micro cracks grow away from nucleation site, which symbolizes the start of crack growth period. Figure 2-1 indicates various steps of fatigue life. Detailed information on these two periods are discussed in chapter 2.1.1 and 2.1.2.

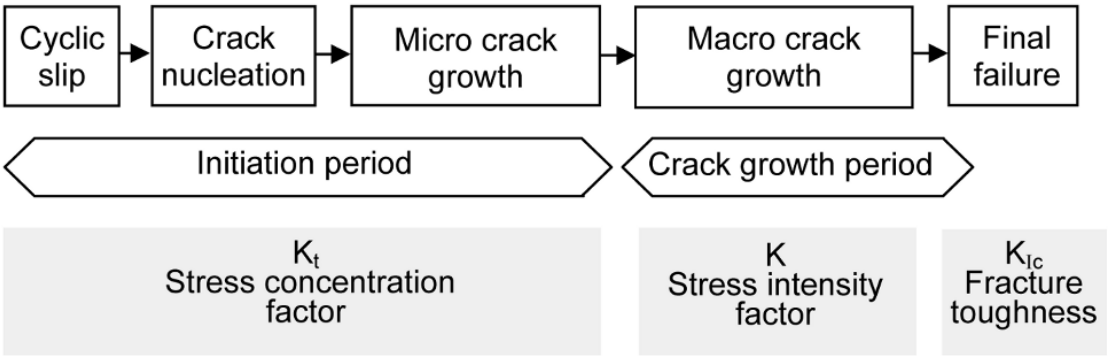

Figure 2- 1 Different phases of fatigue life and relevant factors (Schijve, 2009)

2.1.1 Crack initiation period

Fatigue crack initiation results from cyclic slip. When a specimen or structure is loaded under cyclic loading, even if the stress amplitude is below yielding stress, it will generate cyclic plastic deformation. Due to the low stress level, such deformation only occurs at grain level. In fact, this microplasticity is more likely to happen at material surface due to a lack of restraint and a favorable environment (gas, liquid) on one side. After it appeared on the surface, microplasticity will propagate to deeper layer.

At different grains, shear stress distribution is not homogeneous, which enables the slip band to grow. The size and shape of grains, crystallographic orientation of the grains, and elastic anisotropy of the material can affect the distribution of shear stress. When cyclic slip occurs at grains with favorable conditions, slip steps will appear at the material surface, which means a layer of new material is exposed to the environment. This layer of new material, covered by an oxide layer, forms monolayers which are difficult to remove. Together with strain hardening during the occurrence of slip, it will cause a larger shear stress during unloading, which presents a reverse slip at an adjacent plane that is parallel to the initial slip. Both the presence of new

material and strain hardening process are irreversible. In the end, intrusions and extrusion are formed. The whole process is shown in figure 2-2

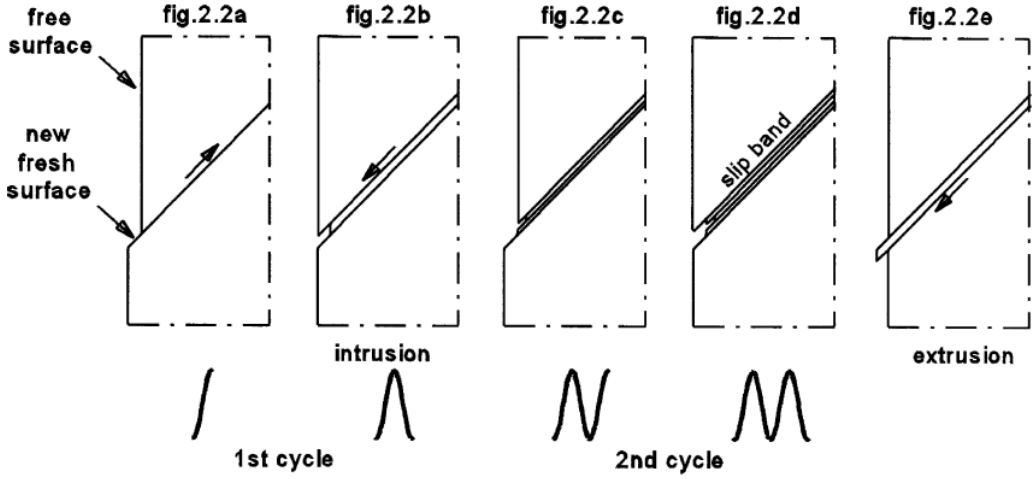

Figure 2- 2 Cycle slip leads to crack nucleation (Schijve, 2009)

As a conclusion, in the fatigue initiation period, fatigue is a surface phenomenon (Schijve, 2009).

2.1.2 Crack growth period

Once a crack appears and enters inner layer of particle, crack growth period will start. As cracks grow deeper inside the material, it will encounter boundaries of grains. This constraint will change the direction of crack propagation, generating multiple slip planes. Moreover, it serves as a barrier to slip bands, which means the crack growth will slow down when slips reaches boundaries of grains. In general, cracks will grow perpendicular to loading direction. This process is shown in figure 2-3. It illustrates that the orientation of crack propagation is different from slip band orientation.

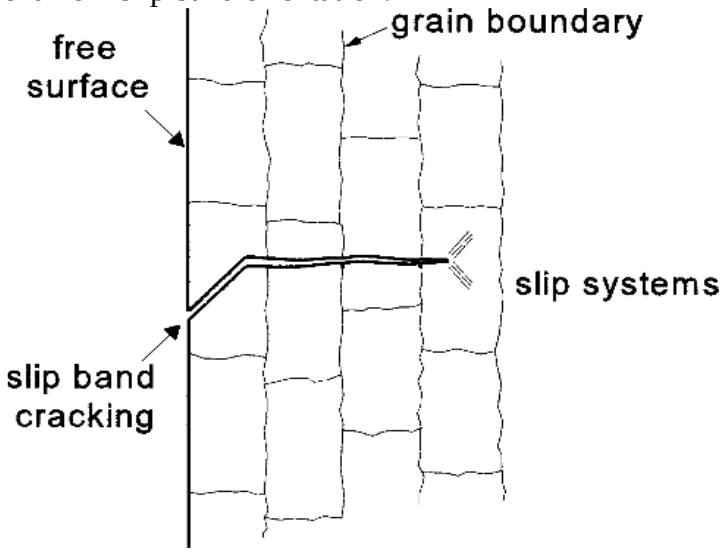

Figure 2- 3 Cross section of micro crack (Schijve, 2009)

In fracture mechanics, crack propagation can be induced by three ways of applying forces
Mode I opening mode
Mode II sliding mode
Mode III tearing mode
The three modes are depicted in figure 2-4

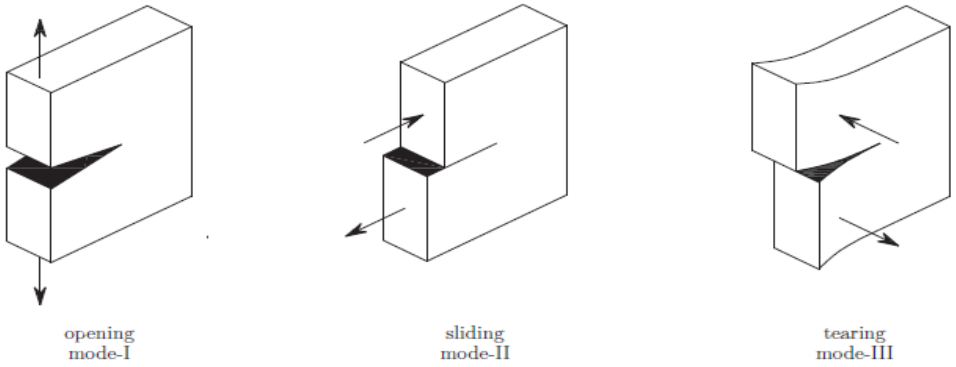

Figure 2- 4 Crack surface displacement modes (Besten, 2015)

In this thesis, the opening form is mainly mode I

2.2 Stress concept

For the calculation of fatigue damage, different stress concepts can be applied. The welded notch stress consists of two components, namely the equilibrium equivalent stress and the self-equilibrium stress. The former is the superposition of membrane stress induced by axial loading and bending stress caused by bending moment. This part is mainly related to global geometry. The self-equilibrating stress, or the non-linear part, is related to local geometry or the notch influence.

According to the abovementioned stress components, one can typically apply the nominal stress, the hot spot stress or the effective notch stress to calculate fatigue life of a structure. The latter concept is more accurate than the former but the calculation is more complex as well. Nominal stress is the membrane stress component. It is derived by classic theories such as the beam theory. Naturally it doesn't include the influence of welding or local geometry change. When the joint corresponds to a tabulated structural detail, fatigue resistance class (FAT) can be found easily by looking up in tables. The hot spot stress includes all the stress raising effects such as global geometry and local components, except for that induced by local weld profile (Hobbacher, 2008). The self-equilibrating stress is excluded in this concept. Hot spot stress concept is suggested when nominal stress is not clearly defined due to complex geometric effects. Figure 2-5 shows the relationship between difference stress concepts.

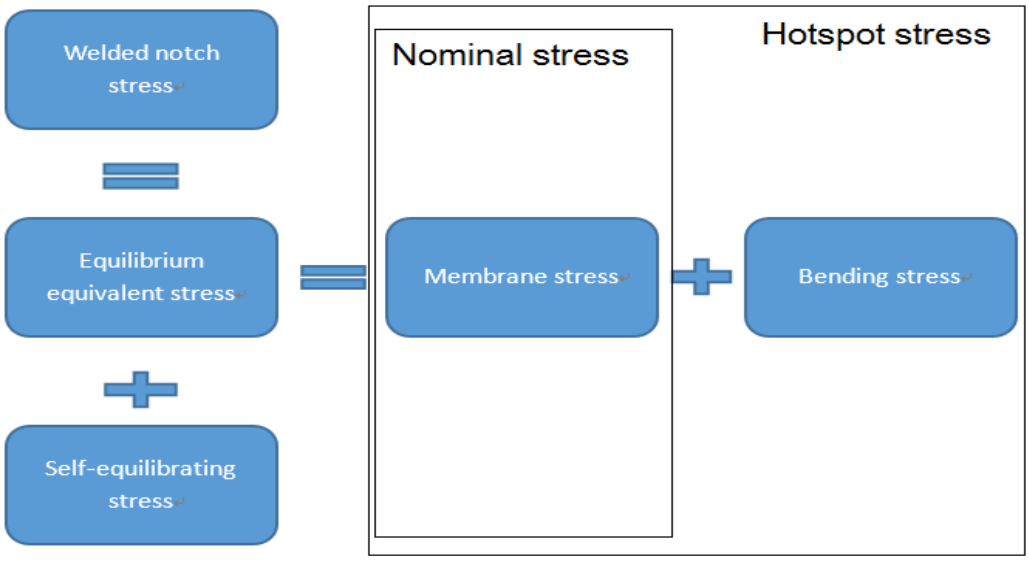

Figure 2- 5 Weld toe notch stress components

In this thesis, hot spot stress concept is applied. For each hot spot, hot spot stress is calculated with extrapolation method.

2.3 Hot spots

A hot spot is a point in a structure where a fatigue crack may initiate due to the combined effect of structural stress fluctuation and the weld geometry or a similar notch (Hobbacher, 2008).

Usually, location of hot spots for welded structure can be decided easily. For more complex geometries the hot spot needs to be determined accurately. Sometimes the identification the hot spots can be difficult. For plated structures the hot spots at weld toes can be generalized in three types. Figure 2-6 shows these three types of hotspots with more details.

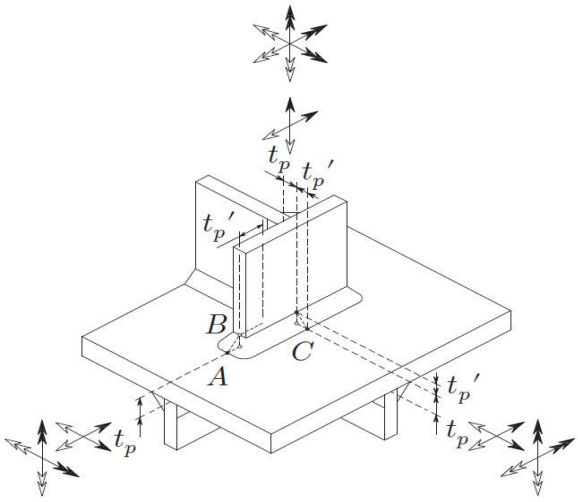

Figure 2- 6 Hot spot type classification (Besten, 2015)

Type A: At the weld toe on a plate at the end of an attachment, called type A.
Type B: At the weld toe on an attachment at the end of an attachment, called type B.
Type C: Along the weld seam, either on a plate or an attachment, called type C.

The hot spots that are analyzed in this thesis are type A hot spots.

2.4 Counting method

Cycle counting is an important part of fatigue damage calculation. When it comes to loading counting, one can easily count the number of cycles for constant amplitude (CA) loading because for each time step, the difference between maxima and minima is same. However, for various amplitude (VA) loading, for each successive combination, $\sigma_{max} - \sigma_{min}$is different. Therefore, VA loading must be transferred into CA loading by counting methods to characterize the features of loading.

By the same logic, counting methods also can be applied to the counting of resultant stress history. Real structures usually experience an irregular stress history and therefore a cycle counting procedure has to be employed to decompose the complex irregular history into a series of simple events equivalent to individual cycles in a constant amplitude stress history (G. Glinka, 1987). In FEM modelling software, the stress history is presented as a sequence of values at each time step. After rainflow counting method, we can obtain the stress amplitudes that occurred during the calculation and the corresponding times of occurrence. Thus Miner's rule can be applied to calculate the accumulated damage.

Several counting methods are proposed, while the most common method is the rain-flow counting method. This method is first proposed by T. Endo in 1967. Later a variation of the rain-flow counting method went out. Details about the original rain-flow counting method is introduced in chapter 2.4.1

2.4.1 Rainflow counting method

To perform this method, a time trace of peaks and valleys of stress level is required. Turn the time trace 90 degrees clockwise and treat it as a pagoda roof on which water drips. That explains the name of rain-flow counting method. Consider each peak as a source of water that "drips" down and start counting the number of half cycles by looking for terminations in the flow occurring when either It reaches the end of the time history, or It merges with a flow that started at an earlier tensile peak, or It flows when an opposite tensile peak has greater magnitude. Then repeat these counting steps for valleys. Assign a magnitude to each half-cycle equal to the stress difference between its start and termination. Pair up half-cycles of identical magnitude (but opposite sense) to count the number of complete cycles. Typically, there are some residual half-cycles.

According to ASTM-E1049-85 (ASTM, 2005), the numerical rules are as follows:

Let X and Y denote the range under consideration and the previous adjacent range, respectively. Let S be the starting point of the stress time trace and follow the steps below.

1. Read next peak or valley. If out of data, go to step 6.
2. If there are less than 3 points, go to step 1. Create X and Y using the 3 most recent peaks and valleys that have not been discarded.
3. Compare the absolute values of X and Y.

•$|x| < |y|$, go to step 1.

•$|x| \geq |y|$, go to step 4.

4. Check whether range Y contains point S.

• If so, go to step 5.

• If not, count range Y as 1 cycle and discard both points of Y. Go to step 2.

5. Count range Y as 0.5 cycle and discard the first point of Y. Move S to the second point of Y and go to step 2.
6. Count each range that has not been discarded as 0.5 cycle.

An example (Rainflow-counting algorithm, 2017) is illustrated in figure 2-7 and 2-8. Figure 2-7 illustrates the original time trace of loading, while figure 2-8 shows the counting from peaks and valleys respectively. Counting result is listed in table 2-1

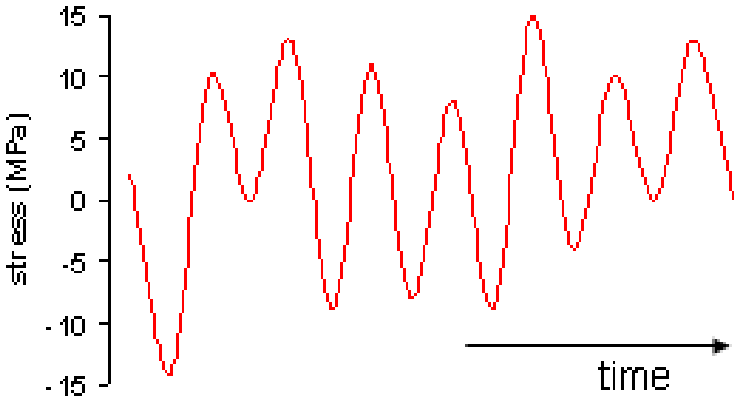

Figure 2- 7 Example of rain-flow counting (time trace)

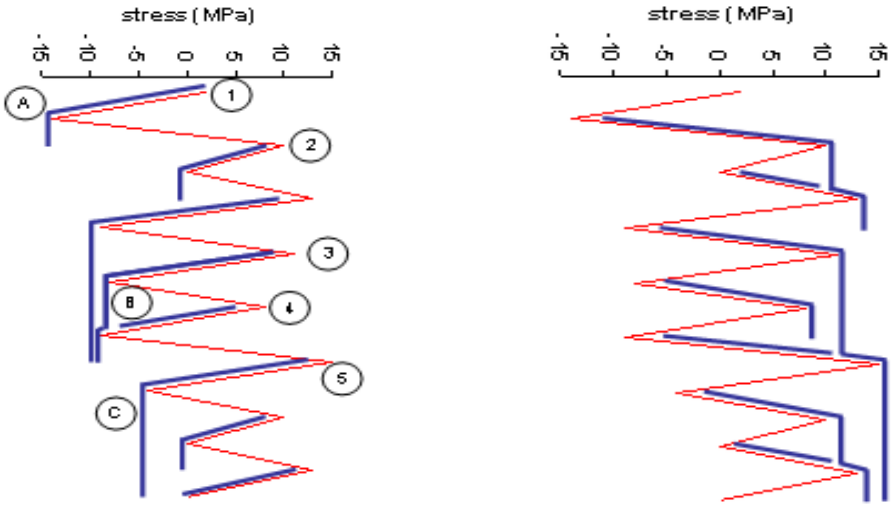

Figure 2- 8 Example of rain-flow counting (counting from peaks and valleys)

Stress(MPa)	Whole cycles	Half cycles
10	2	0
13	0	1
16	0	2
17	0	2
19	1	0
20	0	1
22	0	1
24	0	1
27	0	1

Table 2- 1 Resultant CA stress of rain flow counting example (Rainflow-counting algorithm, 2017)

2.5 S-N curve

An SN curve is a plot of applied stress range versus the number of cycles to failure for a given material. Typically both the stress and number of cycles are displayed on logarithmic scales. A Basquin relation between the number of cycles and the stress range is given as

$$N = C(\Delta\sigma)^{-m}$$

Where N is the number of cycles to failure for a given stress range $\Delta\sigma$, C is a constant and m is the negative inverse slope of the S-N curve. On log-log scale, the line is represented by

$$log^N = log^C - mlog^{(\Delta\sigma)}$$

The International Institute of Welding (IIW) has defined a few FAT classes. A detailed description and the value for C, m can be found with respect to each FAT class. In this master thesis, the structure detail matches with the description 'Cover plate ends and similar joints' (Hobbacher, 2008), therefore, as recommended, S-N curve for FAT class 100 for hot spot stress is used.

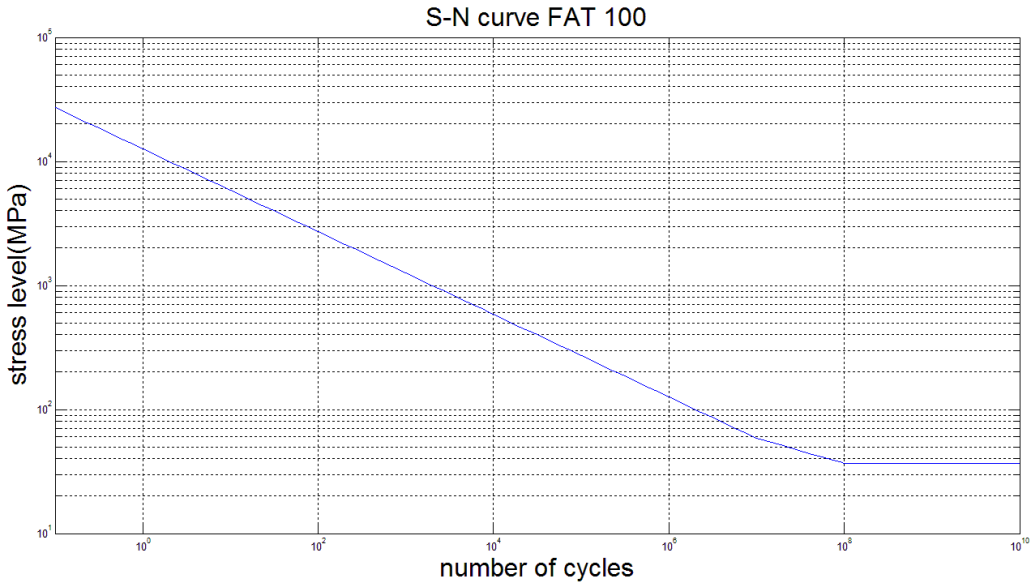

Figure 2- 9 S-N curve FAT 100

2.6 Damage calculation and the Palmgren-Miner rule

Fatigue damage calculation is usually done based on CA stress. However in reality, a structure usually experiences VA stress. A VA stress can be transferred into a CA stress through some counting methods. To determine the cumulative fatigue damage, several methods are proposed and the most widespread one is the Palmgren-Miner rule.

The Miner rule states that if there are k different stress levels and the average number of cycles to failure at the ith stress, S_i, is N_i, then the damage fraction, C, is:

$$\sum_{i=1}^{k} \frac{n_i}{N_i} = C$$

Where n_i is the number of cycles accumulated at stress S_i. C is the fraction of life consumed by exposure to the cycles at the different stress levels. In general, when the damage fraction reaches 1, failure occurs. However, the definition of failure for a physical part varies. It could mean that a crack has initiated on the surface of the part. It could also mean that a crack has gone completely thru the part. In this thesis, we assume that when damage reaches 1, it means failure occurs.

As a simple cumulative damage model, it has two main limitations. The first one is that the critical damage that causes failures is not a fixed value. It follows a certain distribution. The second one is that it is not necessary for the damage to accumulate linearly.

Chapter 3 Numerical Solution

Currently, tank containers are mainly transported by truck, railway and sea. Compared with truck transportation, railway transportation is safer and cheaper, and less dependent on natural conditions. Compared with sea transportation, railway transportation is faster and more convenient, as the starting point and destination are usually accessible through railway network. Thus railway transportation is of great importance to container shipment. The existence of defects in the railway system is the main source of abnormal vibration. As the speed of transportation and axel load increase, the hazardous vibration induced by wheel flat or railway imperfection intensifies significantly, causing failure and fatigue damage to not only the railway but also the tank container supporting structures. Thus a comprehensive study of the rail-wheel system in the presence of wheel flat is necessary. In case measured data from different companies differ from each other significantly, the numerical solution can be used to validate the measured data. Besides, for the situation where field experiments are not feasible due to local regulations, the numerical model can be used for prediction of the impact force and vertical acceleration.

Figure 3-1 shows the situation where a tank container is transported by railway. Once loaded in the right way, the tank container, as well as the railway car, is subjected to accelerations from three directions, namely the longitudinal direction, the lateral direction and the vertical direction. In this part of the thesis, the vertical acceleration of the system is of great interest and the behavior of the vertical acceleration under different conditions is investigated.

Figure 3- 1 Illustration of container transported by railway

3.1 The complete numerical model

The whole system mainly consists of two parts, the vehicle and the track system.

The vehicle is modelled as a quarter car supported on a bogie, while the side frame is supported on two wheel sets. The primary suspension connecting the wheels and the bogie frame is modelled as a parallel combination of a linear spring and a viscous damping element. The secondary suspension connecting the bogie frame and the car body is considered as the same. The mass of the car body M_c, bogie mass M_t, wheel mass M_w and moment of inertial of the bogie J_t are coupled through the suspension elements. In total, the vehicle is represented by a 5-DOF system that includes the car body vertical motion ,$w_c(t)$, the bogie vertical and pitch motions, $w_t(t)$ and $\psi_t(t)$, respectively, and vertical motions of the wheels, $w_{w1}(t)$and $w_{w2}(t)$. The primary suspension stiffness and damping elements are represented by K_{s1} and C_{s1} respectively, while K_{s2} and C_{s2} represent the stiffness and viscous damping coefficient due to secondary suspension.

The track system includes three layers. They are the railway, the sleepers and the ballasts. The railway is modeled as an Euler-Bernoulli beam and the conventional beam theory is used to analyze its deflection response under a moving load. For the convenience of calculation, it is considered as a beam with finite length and it is discretized as 60 evenly distributed nodes. On each node the railway is supported on the sleepers, the ballasts and subgrades. The railway is considered to be symmetric with respect to its centerline. Each sleeper, together with respective discretized railway element and ballast are connected by spring and viscous damping element. Between each adjacent ballast block lies a connecting spring and viscous damping element to simulate the shear coupling of the ballasts. The motion of the railway coupled with the sleepers and ballasts is denoted as $w_r(t)$. The sleeper and ballast mass are denoted as M_s and M_b. K_p, C_p, K_b, C_b are the railpad and ballast stiffness and damping coefficients respectively. K_w and C_w describes the shear stiffness and damping coefficient of ballasts. The subgrade shear stiffness and damping coefficient are K_f and C_f (Rajib Ul Alam Uzzal, December 2008).

The car system and the track system are coupled by the contact force at the rail-wheel interface. Details of the model is illustrated in figure 3-2

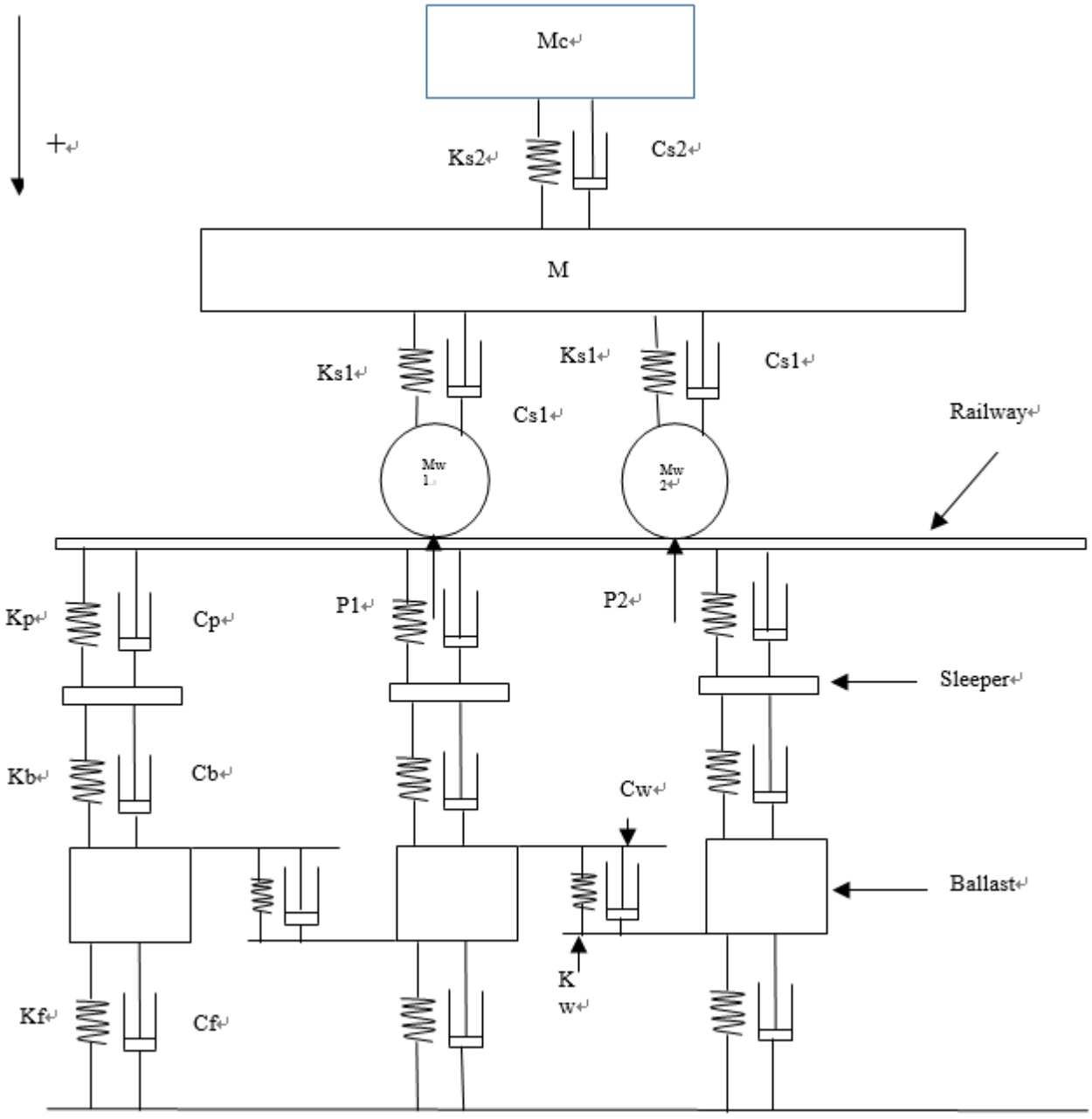

Figure 3- 2 Illustration of the numerical model

3.1.1 Equations of motion of the car system

The force from primary suspension is considered to be loaded on the center of bogie mass. For each part of the system, gravity is considered as the external load. For the wheel, an additional component of the external load is the contact force, which is generated as the wheel touches the railway. Thus the equations of the motion of the car system is summarized below.

For the car body bounce motion,

$$M_c \ddot{W}_c + C_{s2} \dot{W}_c + K_{s2} W_c - C_{s2} \dot{W}_t - K_{s2} W_t - m_c g = 0$$

For the bogie bounce motion,

$$M_t \ddot{W}_t + K_{s1}(W_t + l_f \varphi_t - W_{w1}) + K_{s1}(W_t - l_r \varphi_t - W_{w2}) + K_{s2}(W_t - W_c)$$
$$+ C_{s1}(\dot{W}_t + l_f \dot{\varphi}_t - \dot{W}_{w1}) + C_{s1}(\dot{W}_t - l_r \dot{\varphi}_t - \dot{W}_{w2}) + C_{s2}(\dot{W}_t - \dot{W}_c) - m_t g = 0$$

For the bogie pitch motion,

$$J_t \ddot{\varphi}_t + K_{s1} l_f (W_t + l_f \varphi_t - W_{w1}) - K_{s1} l_r (W_t - l_r \varphi_t - W_{w2})$$
$$+ C_{s1} l_f (\dot{W}_t + l_f \dot{\varphi}_t - \dot{W}_{w1}) - C_{s1} l_r (\dot{W}_t - l_r \dot{\varphi}_t - \dot{W}_{w2}) = 0$$

For the front wheel bounce motion,

$$M_w \ddot{W}_{w1} + C_{s1}(\dot{W}_{w1} - \dot{W}_t) + K_{s1}(W_{w1} - W_t) - C_{s1} l_f \dot{\varphi}_t - K_{s1} l_f \varphi_t - m_{w1} g + P_1 = 0$$

For the rear wheel bounce motion,

$$M_w \ddot{W}_{w2} + C_{s1}(\dot{W}_{w2} - \dot{W}_t) + K_{s1}(W_{w2} - W_t) + C_{s1} l_r \dot{\varphi}_t + K_{s1} l_f \varphi_t - m_{w2} g + P_2 = 0$$

3.1.2 Equations of motion of the track system

3.1.2.1 Equation of motion of the railway beam

The equations of motion of the entire track system are derived upon integrating the equation of motion for the rail as an Euler beam with the differential equations of motions for the discrete sleeper and ballast supports. The deflection of the continuous rail can be derived from the partial differential equation for the Euler beam as:

$$EI \frac{\partial^4 w_r(x,t)}{\partial x^4} + m_r \frac{\partial^2 w_r(x,t)}{\partial t^2} = -\sum_{i=1}^{N} F_{rsi}(t)\delta(x - x_i) + \sum_{j=1}^{2} P_t'(t)\delta(x - x_j)$$

Where *N* is total number of sleepers considered in the model, *k* is the number of deflection modes considered for the rail beam and *j* is the number of wheel sets incorporated in the vehicle model, which represent the number of moving point loads acting on the beam. *E* is the elastic modulus of rail beam materials and *I* is the second moment of area. The coordinate *x* represents the longitudinal position of the beam with respect to the left end support of the rail beam. X_i defines the position of the i th sleeper and $\delta(x)$ is the Dirac delta function

$F_{rsi}(t)$ is force developed at the i th rail/sleeper interface, which follows

$$F_{rsi}(t) = K_{pi}\left[w_r(x_i,t) - w_{si}(t)\right] + C_{pi}\left[\dot{w}_r(x_i,t) - \dot{w}_{si}(t)\right]$$

Since gravity is distributed on each part of the car system, the vertical force acting on the wheels consists of only the dynamic part, namely the contact force. Using the Hertzian contact model we have

$$P_j(t) = Ch\left[w_{wj}(t) - w_r(x_j,t) - r_j(t)\right]^{\frac{3}{2}};\ j = 1,2$$

Where Ch is Hertzian wheel-rail contact coefficient and $r_j(t)$ is the wheel flat function for the specified wheel. From the equation we find the contact force grows as the relative displacement increases. In case there is a loss of wheel-rail contact, $P_j(t)$ equals zero.

3.1.2.2 Equations of motion for the sleepers and ballasts

The equation of motion for the discrete sleeper and ballast masses are derived as follows:

$$M_{si}\ddot{w}_{si}(t) + (C_p + C_b)\dot{w}_{si}(t) + (K_p + K_b)w_{si}(t) - C_b\dot{w}_{bi}(t) - K_b w_{bi}(t) - C_p\sum_{k=1}^{K} Y_k(x_i)\dot{q}_k(t) - K_p\sum_{k=1}^{K} Y_k(x_i)q_k(t) = 0;\ i = 1,2,\ldots\ldots N$$

$$M_{bi}\ddot{w}_{bi}(t) + (C_f + C_b + 2C_w)\dot{w}_{bi}(t) + (K_f + K_b + 2K_w)w_{bi}(t) - C_b\dot{w}_{si}(t) - K_b w_{si}(t) - C_w\dot{w}_{b(i+1)}(t) - K_w w_{b(i+1)}(t) - C_w\dot{w}_{b(i-1)}(t) - K_w w_{b(i-1)}(t) = 0;\ i = 1,2,\ldots\ldots N$$

Note that the shear coupling only exists between ballast masses. Thus

$$W_{b0}(t) = \dot{W}_{b0} = 0;\ \text{and}\ W_{b(N+1)}(t) = \dot{W}_{b(N+1)} = 0$$

3.2 Choice of Input

The result of this numerical solution is heavily dependent on the input parameters. To guarantee convergence of the system, input parameters that are verified by previous researcher are selected and used. The input parameters comes from a typical wagon-track system in North America. Detailed data are listed below

Notation	Description	Value
M_c	Car body mass(quarter car)	19400kg
M_t	Bogie mass(half)	500kg
M_w	Wheel mass	500kg
J_t	Bogie mass moment inertia	176kg-m^2
K_{s1}	Primary suspension stiffness	788MN/m
K_{s2}	Secondary suspension stiffness	6.11MN/m
C_{s1}	Primary suspension damping	3.5kN-s/m
C_{s2}	Secondary suspension damping	158kN-s/m
D_f	Wheel flat depth	0.4mm
L_f	Wheel flat length	52mm

Table 3- 1 Input parameters

3.3 Simplified models and results

3.3.1 Models

The abovementioned system is too complicated. Thus a few simplified cases are studied. Since the input and result provided by previous researchers are not complete, some of the calculations are performed with MATLAB ode45 solver and then verified by Simulink.

3.3.1.1 3-DOF model

In the first model, the influence of railway, sleepers and ballasts are ignored, and it is assumed the wheels will not separate from the railway. In this model, the railway is considered as rigid support without imperfection lying at z=0. The wheel displacement will be zero. The whole system consists of only the car body and the bogie and respective connections. Only three degrees of freedom, namely the bounce of the car body and the bounce and pitch of the bogie are taken into consideration.

3.3.1.2 5-DOF model

In the second model, the wheels are included and modelled as masses connected to the bogie by primary suspensions. The railway is considered as rigid support without deflection lying at z=0. Since the wheel cannot 'run into' the railway, the boundary condition becomes:

$$\text{for } W_{wi}(t) \geq 0, P_1 = ((\frac{M_c + M_t}{2}) + M_{wi})g; W_{wi} = 0; i = 1,2$$

$$\text{for } W_{wi}(t) < 0, P_1 = 0; i = 1,2$$

Note that when $W_{wi} < 0$, it means the ith wheel is separated from the wheel.

3.3.2 Calculations

3.3.2.1 Gravity influence

Firstly, for the first model, initial conditions are taken as 0 for all degrees of freedom. Results are shown below.

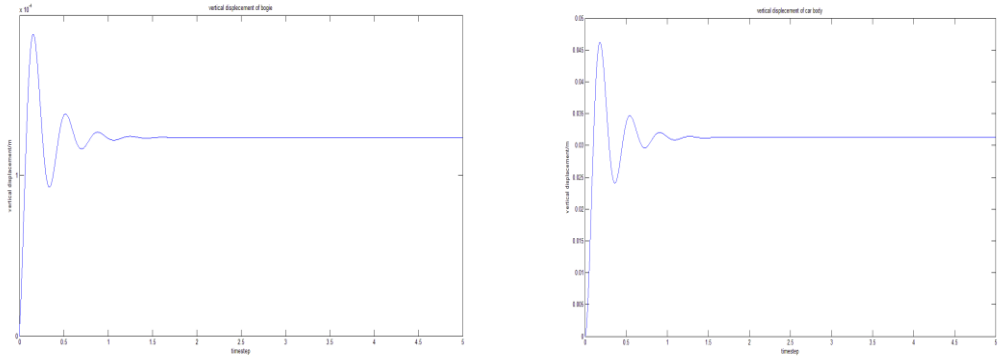

Figure 3- 3 Vertical displacement of the bogie (left) and car body (right)

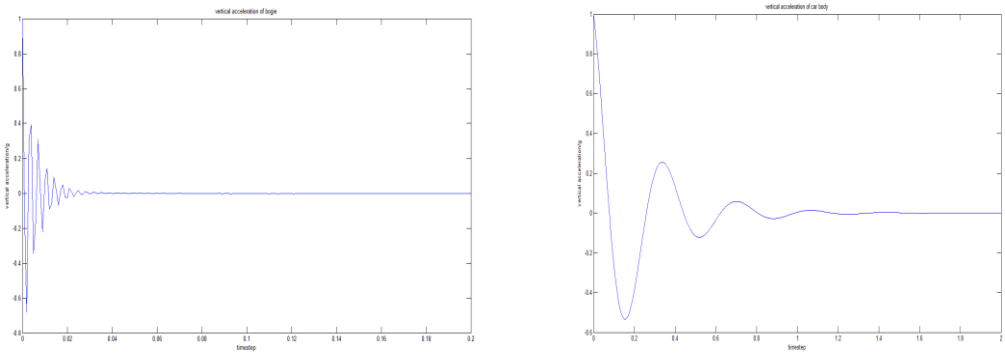

Figure 3- 4 Vertical acceleration of the bogie (left) and car body (right)

From figure 3-3 and 3-4 we find this case describes the oscillation of a system under gravity and a certain initial condition. Eventually the vibration dies down due to damping effect. In the end it reaches static equilibrium. Since the primary spring has a higher stiffness, the displacement of car body is much larger than that of the bogie. The highest acceleration is 1g, which corresponds to the initial condition. The result validates the method.

The same calculation is also performed on the second model. The initial conditions for all degrees of freedoms are 0. The results are shown below.

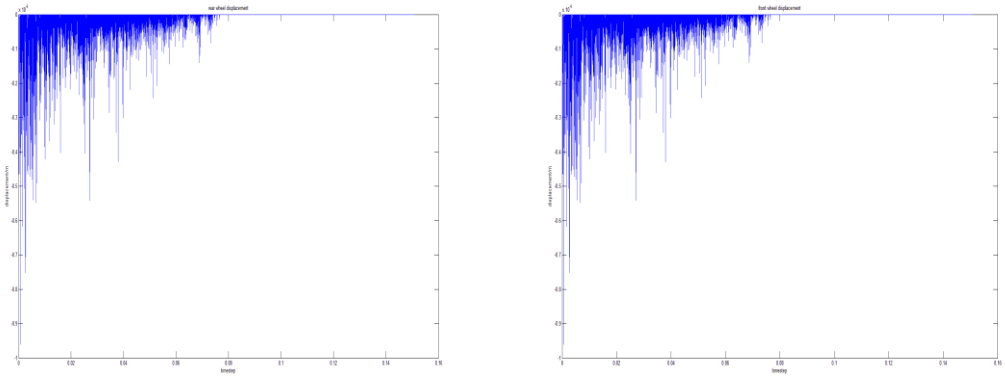

Figure 3- 5 Wheel displacement of rear wheel (left) and front wheel (right)

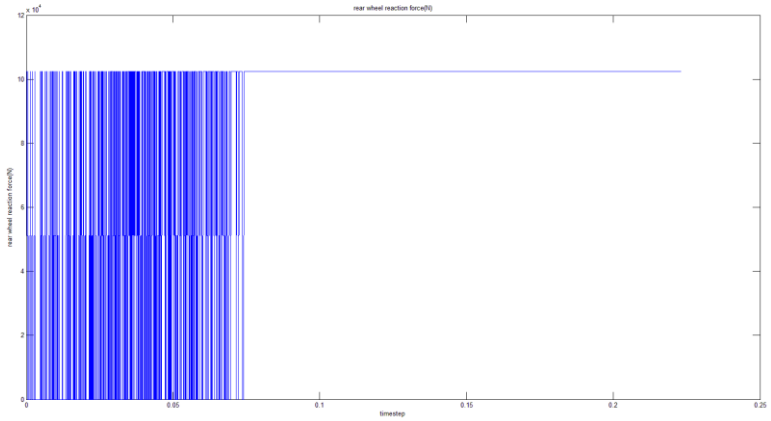

Figure 3- 6 Rear wheel reaction force

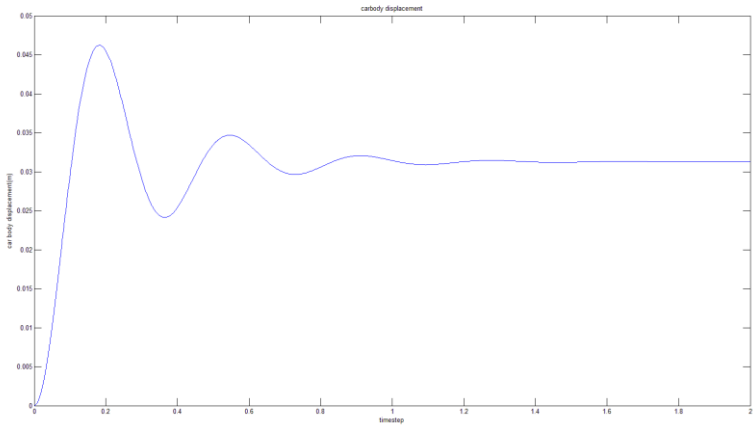

Figure 3- 7 Displacement of car body

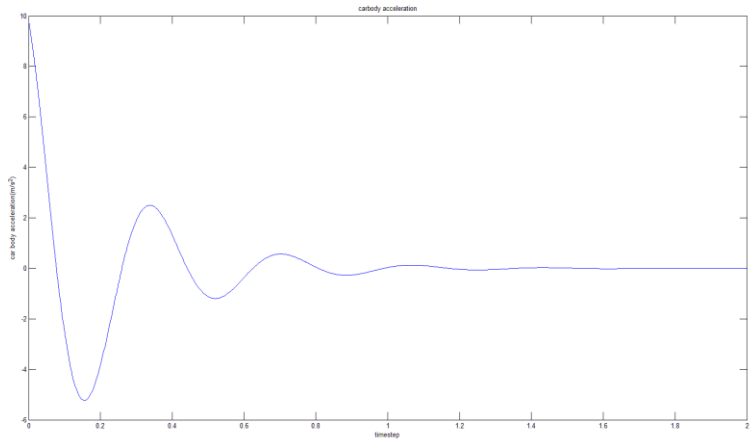

Figure 3- 8 Acceleration of car body

From figure 3-5 we find that there are some moments where the wheels are slightly separated from the railway. This is because when the wheels contact the railway, the contact forces acted on the wheels are too large. When the wheels separates from the railway, the contact force diminishes and gravity pulls it back to the railway. This can also be found in figure 3-6, which illustrates that the contact force swings between 0 and half of total weight. After a short period of time, the system reaches its equilibrium. In the end the vertical displacement and the acceleration history of the car body are same as in previous model (figure 3-7 and 3-8).

3.3.2.2 Elevated car system

The second group of calculation is done on both models. Firstly, for the first model, the car body and bogie are given a specified initial displacement to simulate the situation where after a special stimulation, the whole car system is elevated. Then the wheels have contacted the railway (equilibrium position) while the car body and the bogie are still ‘floating’ in the air. The initial displacement given by the stimulation is 2mm. The result is shown below.

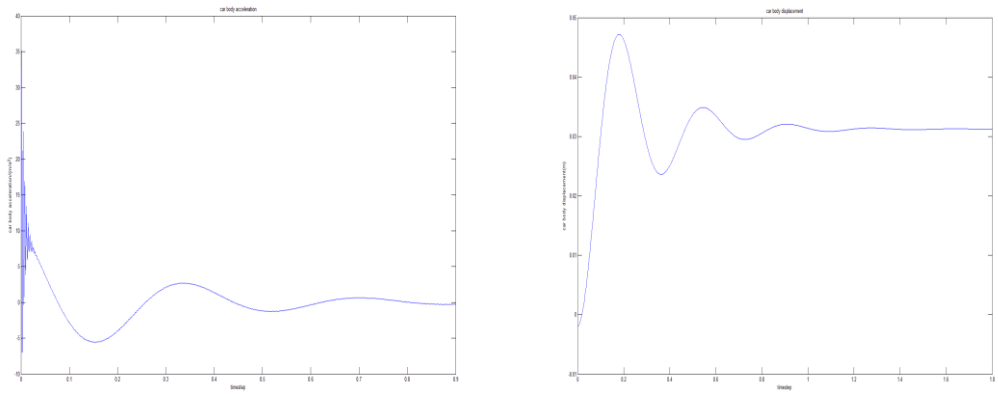

Figure 3- 9 Car body acceleration (left) and displacement (right)

From figure 3-9 we find that total force acted on the car body is much larger than in the first calculation because under this initial condition, the springs are further prolonged, thus yielding a larger car body acceleration. The peak acceleration has increased to 3.5 times. Apart from that, the tendency of vibration is same. In the end, the car reaches the same equilibrium position.

The same calculation is carried out on the second model. Different from abovementioned calculation, the same initial conditions are also specified on both wheels. Hence it simulates the situation where the whole car system is elevated due to some external loading. The results are shown below.

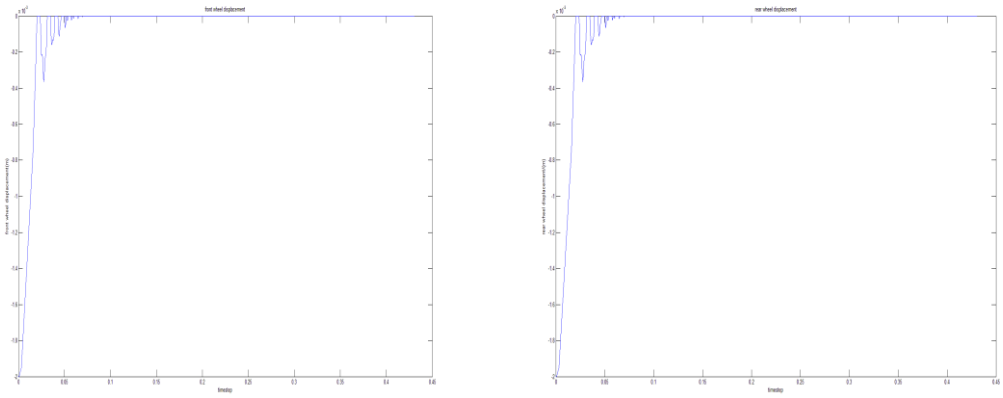

Figure 3- 10 Wheels displacement after 2mm elevation

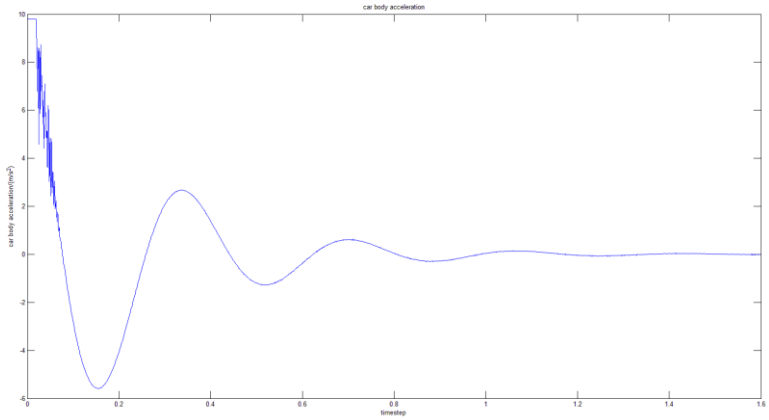

-

Figure 3- 11 Car body acceleration

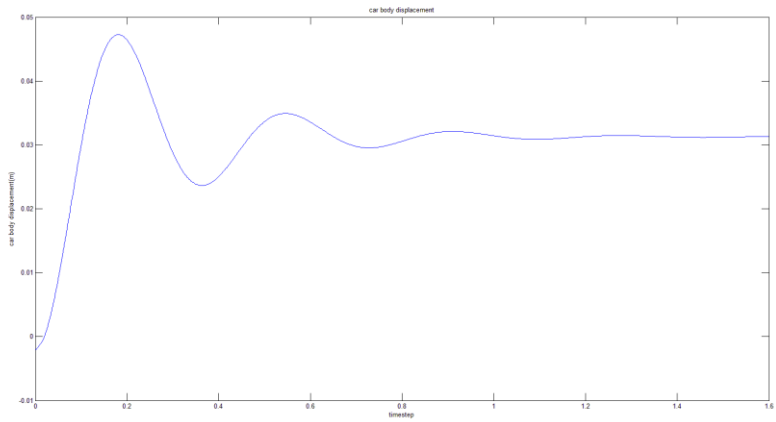

Figure 3- 12 Car body acceleration

At the initial moment, the whole system will move vertically downward due to gravity. When the wheel contacts the railway, the large contact force makes it bounce back. Due to the primary suspension, the vertical movement will die down gradually. In the end the wheels will stay on the railway, and the car body vibration will decrease to zero eventually. Each time the wheel contacts the railway, it generates some 'noise' in the car body acceleration because an external load is introduced to the system. Eventually the car body reaches the same equilibrium as described before.

3.3.2.3 Wheel flat influence

Since only the second model contains the wheels, this calculation is performed only on this model. A haversine flat is introduced to the rear wheel. The wheel flat is expressed as

$$W_d(t) = \frac{D_f\left(1 - \cos\left(\frac{2\pi v t}{l_f}\right)\right)}{2}$$

Where D_f is flat depth, L_f is the length of the flat, v is the speed of the train. The wheel flat is illustrated in figure 3-13

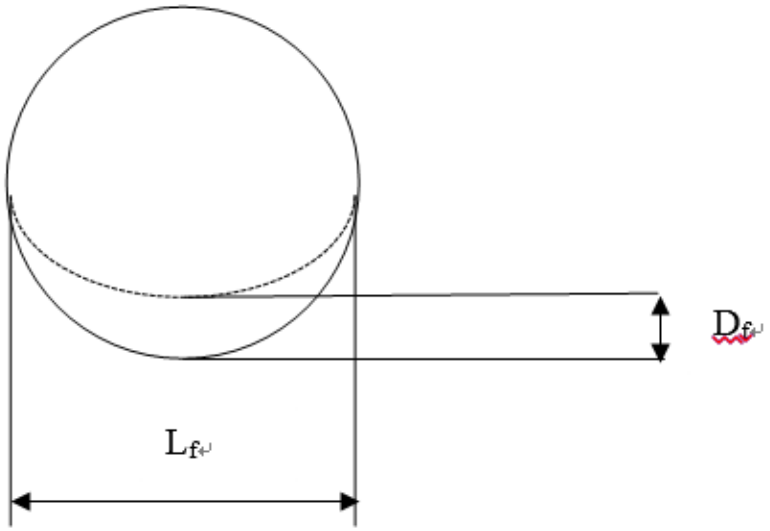

Figure 3- 13 Illustration of wheel flat

In the calculation, the train speed is set as 3.6km/h so that at the first small steps, details of the system movement can be tracked. In this situation, the period of wheel flat is 0.052s. Figure 3-14 pictures the wheel flat history.

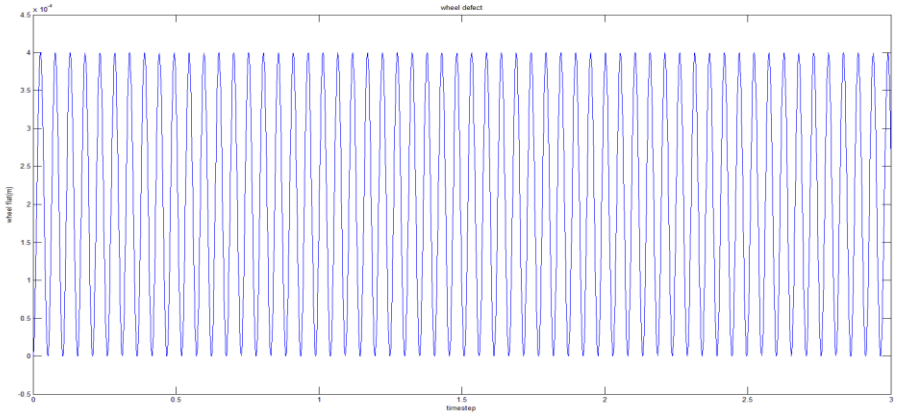

Figure 3- 14 Wheel flat history

The boundary condition thus becomes:

for $W_{w1}(t) - W_d(t) \geq 0, P_1 = ((\frac{M_c + M_t}{2}) + M_w)g; W_{w1}(t) = W_d(t)$;

for $W_{w1}(t) - W_d(t) < 0, P_1 = 0;$

The results are shown below

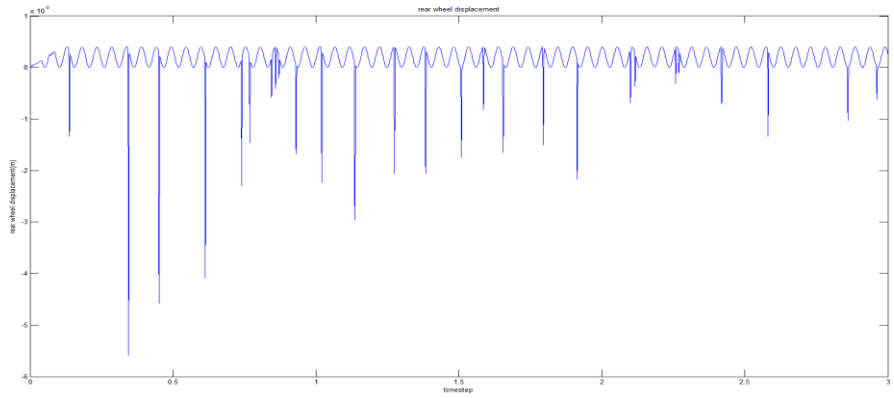

Figure 3- 15 Rear wheel displacement with wheel flat

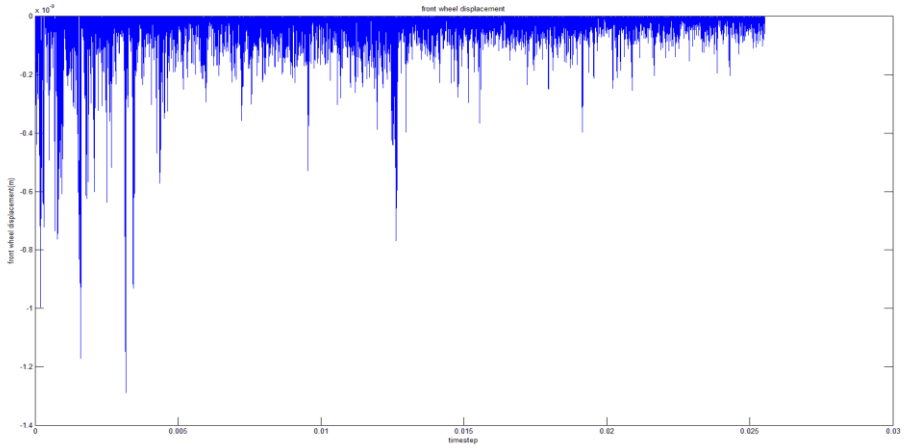

Figure 3- 16 Front wheel displacement without wheel flat

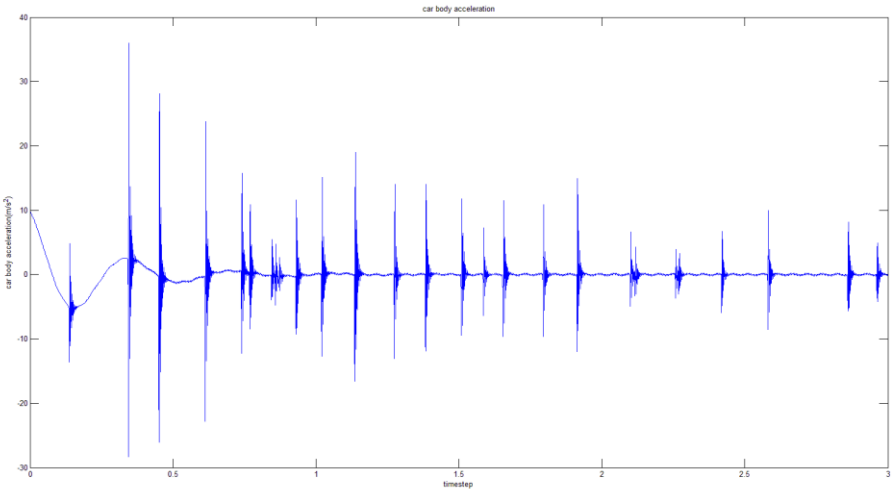

Figure 3- 17 Car body acceleration under wheel flat

Comparing figure 3-5 with figure 3-16, we find that the movement of the front wheel is not much affected. However, the wheel flat introduces a lot of influence to the rear wheel. After the initial moment, the wheel is allowed to move downward due to the wheel flat. Then after each 0.052s, the wheel flat disappears and the wheel moves back to 0. Due to the large contact force, at some time-steps. It bounces up and separates from the railway slightly then goes back to the railway. Whenever the wheel is bounced up, the springs are suppressed, causing a larger acceleration in the car body. This can be seen in figure 3-17. Variable time steps are taken in this calculation, when constant time step is applied, the same pattern of motion should be see in figure 3-15 and figure 3-17

3.4 Conclusion

The acceleration of the car body depends on both the input parameters and road conditions. Based on the abovementioned calculations, the acceleration range can be from -3g to 3g. Thus the measured vertical accelerations are reasonable.

Chapter 4 Static Test Analysis

Before the calculation of fatigue, a few tests are conducted to validate the all-shell model. The most important are the stacking test, the restraint test, the racking test and the lifting test. The performance of the tests are based on the ISO standard. The location and the value of the external forces are based on the ISO standard. The experimental data of static tests are provided by the Lloyd's register (Lloyd's Register SHI0816414 , 2008). A comparison of the simulation result and experimental data is listed at the end of each test.

Item	Value
External length	6058mm
External width	2438mm
External height	2591mm
Capacity	26000L
Maximum gross weight	36000kg
Tare weight	3820kg
Maximum cargo weight	32180kg

Table 4- 1 Dimensions and details of the tank container

Structure	Element type	Material property in ANSYS		
		Young's modulus	Poisson ration	Yield strength
Frame	Shell181	2.06e5MPa	0.28	345MPa
Vessel	Shell191	2e5MPa	0.3	170MPa
Corner castings	Shell191	1.95e5MPa	0.3	415MPa
Skirt	Shell191	1.95e5MPa	0.3	304MPa
Side reinforcement	Shell191	2e5MPa	0.3	410MPa

Table 4- 2 Material properties of the tank container

Details of this tank container and global model is listed in table 4-1 and table 4-2. After checking with report provided by the Lloyd's register, the dimensions of the model matches with requirements. Descriptions of the static tests mentioned in this chapter come from ISO 1496-3:1995(E).

4.1 Stacking test

Experiment description

Before a container is put into use, a few static tests should be performed. The stacking test is one of them. This test aims at proving the ability of the container to support a superimposed mass of containers, taking into account conditions aboard ships at sea and the relative support eccentricities between superimposed containers.

As requested by IMO regulations, a nine-high stacking, i.e. eight containers stacked on top of one container, is applied in the experiment. According to the experimental data provided by Lloyd's Register, each stacked container is filled with water up to the gross weight of 27000kg and the vertical acceleration for the stacked containers is considered as 1.8g. These data are used to calculate stacking force according to the standard. As a result, vertical stacking force on the bottom container is 1.8*9.8*27000*8=3.81MN.

Containers are stacked on the upper corner fittings of the bottom container with an offset of 25.4mm laterally and 38mm longitudinally. Thus the bottom container is subjected to a combination of vertical force, lateral moment and longitudinal moment. In the computational model, the influence of water can be included by modifying the density of the structure.

The container is simplified as a cuboid, as illustrated in figure 4-1. The upper corners are depicted as A,B,C,D and the bottom corners are represented as A1,B1,C1,D1. In later chapters, the descriptions of the boundary conditions are based on these letters. In the all-shell model, each corner fitting is modelled as a cube with six faces. Thus the surface on which the force is loaded will be mentioned.

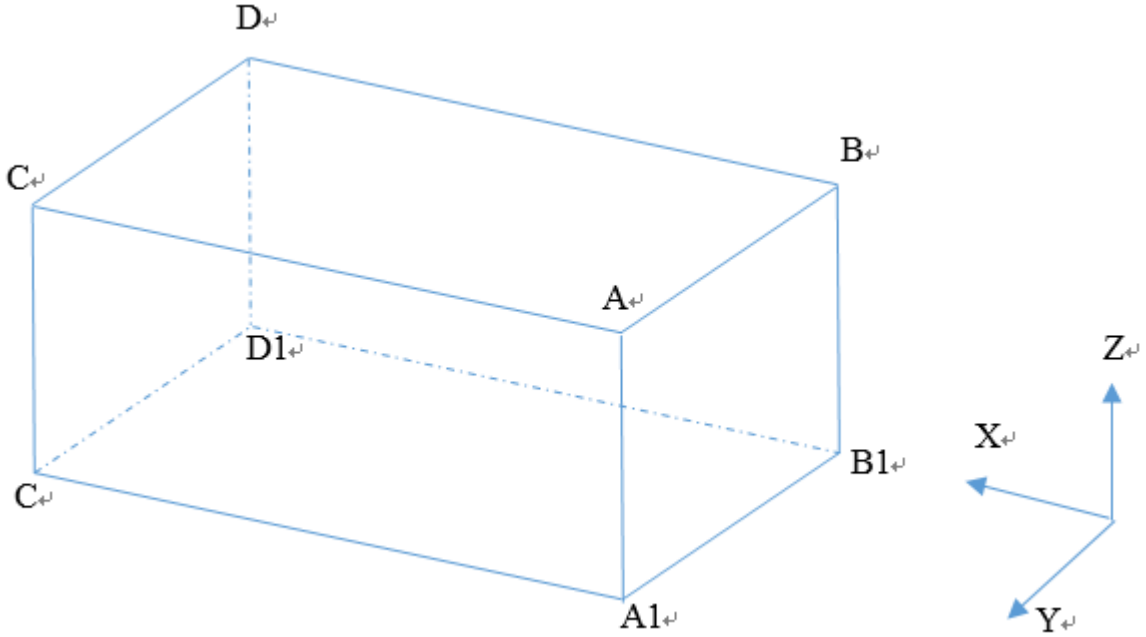

Figure 4- 1 Simplified container model

Eight parameters, namely the lateral and longitudinal displacement of A,B,C,D are measured during and after the test. In the simulation, measurements are done at the center node of the upper face of A,B,C,D. The measurement is illustrated in figure 4-2 in detail.

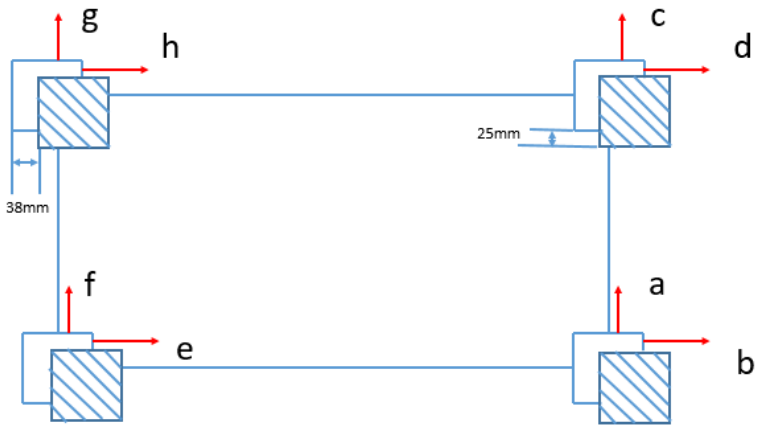

Figure 4- 2 Illustration of measurement

Boundary conditions

The bottom corner fittings of the bottom container are fixed so the translational motion along three directions as well as the rotational movement along the z axis are zero. In other words, at point A1,B1,C1,D1, Ux, Uy, Uz and Rotz are zero. External loadings are located on the upper surface of A,B,C,D. The stacking forces are loaded on the center node of the upper surface of A,B,C,D. Due to the complexity of the distribution of the moments, the lateral moment and longitudinal moment are considered as loaded on the center node of the upper face of A,B,C,D.

Result and analysis

Figure 4-3 and 4-4 shows the displacement vector field and Von Mises stress plot of the stacking test. The measured displacements on the upper corner fittings are shown in table 4-3.

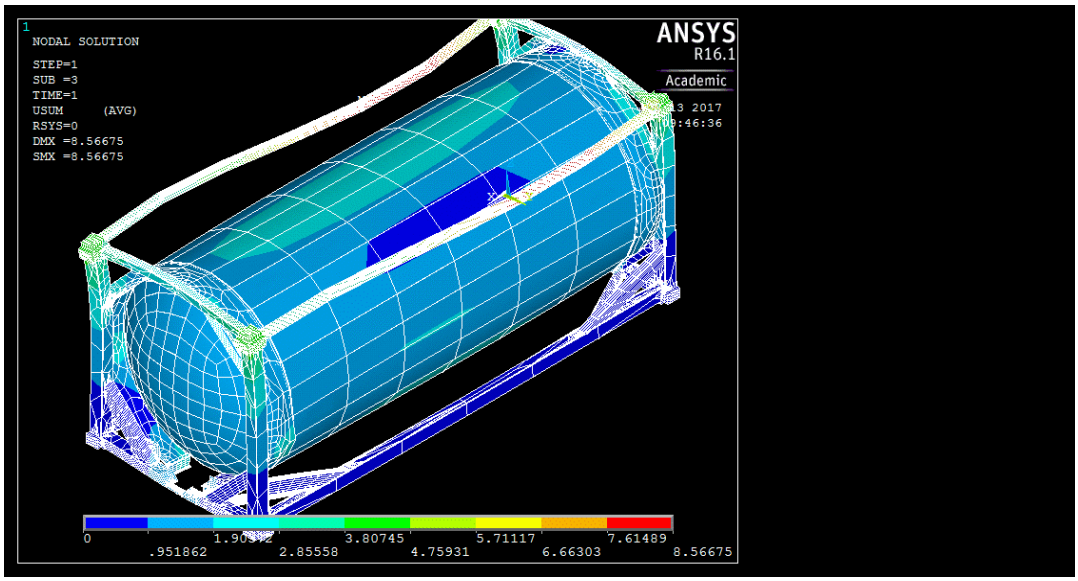

Figure 4- 3 Displacement vector field of the stacking test

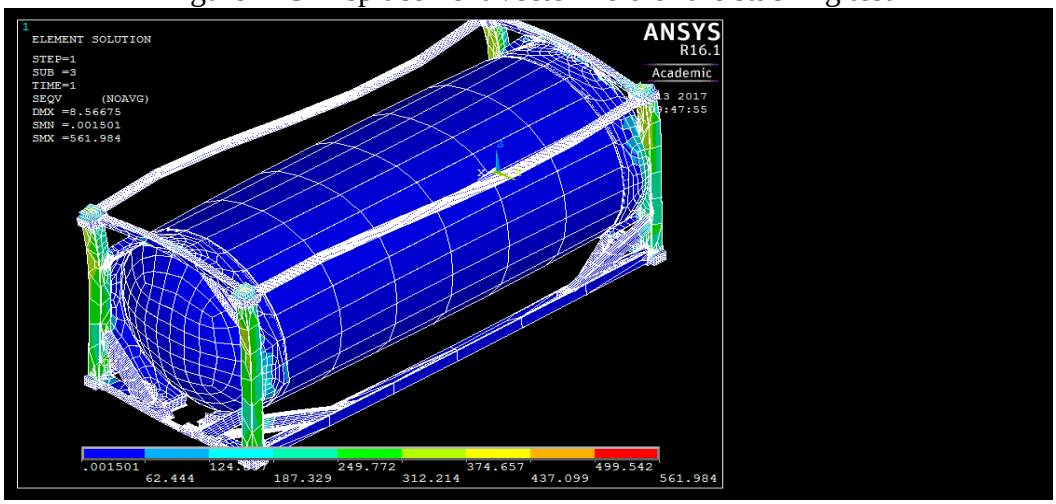

Figure 4- 4 Von Mises stress plot of stacking test

Measurement point	Experimental data/mm	Simulation result/mm
a	0.5	0.36
b	2.5	2.52
c	0.5	0.33
d	2.5	2.68
e	1.5	0.26
f	1.5	2.84
g	1	1.1
h	1	2.93

Table 4- 3 Result comparison between simulation and experiment

From the Von Mises stress plots we find that for most of the elements, the result is in elastic phase, which matches the description of the experiment provided by Lloyd's Register. For some measuring points, the result falls into an acceptable range. For other points, it doesn't. This might originate from the difference in modelling, loading and selection of result.

Firstly, as it is mentioned before, the corner castings are modelled as plates with thickness and shell element is used instead of solid element. As a consequence, the stiffness of the corner castings is different from solid corner castings. Together with the asymmetry of the structure, it could cause a different result in displacement for different nodes. Secondly, the vertical force and moments are loaded on the center node on the contact surface. However, the moment distribution could be different and there are multiple ways to apply the load. A different loading might lead to different results. Last but not least, the results are extracted from the center node of the upper face of upper corner castings, which could be different from the result measure from another location. Hence, based on the abovementioned reasons, it is believed the structure is trustworthy to reflect the reality and the structure can withstand stacking force.

4.2 Restraint test

Experiment description

The external restraint test is carried out to prove the ability of a tank container to withstand longitudinal external restraint under dynamic condition or railway operation, which implies the longitudinal acceleration is 2g. The experiment is illustrated in figure 4-5

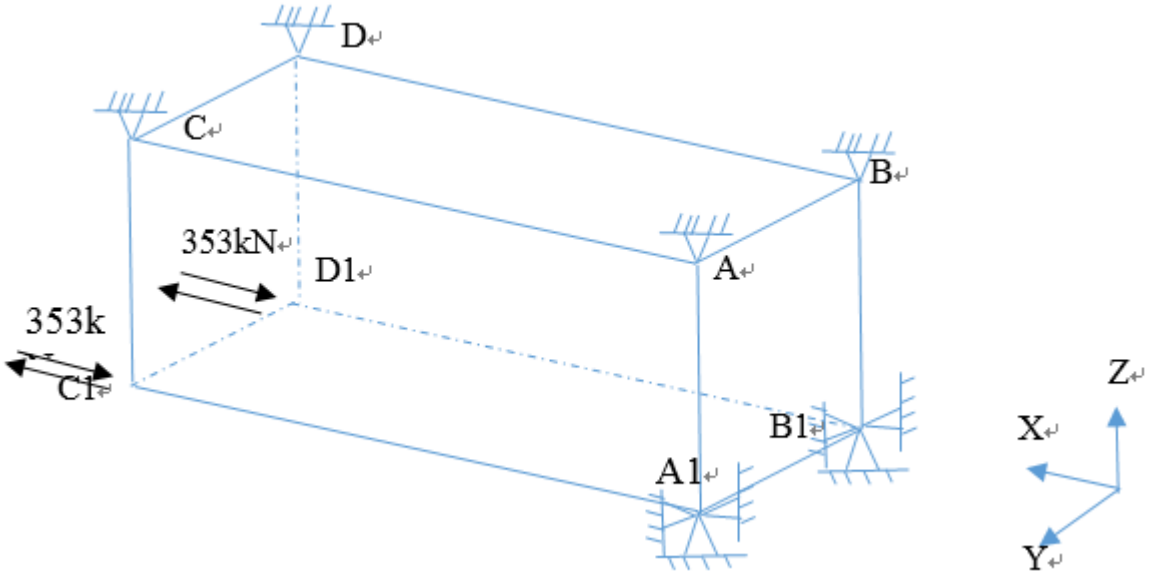

Figure 4- 5 Illustration of the restraint test

Boundary conditions

In this experiment, the container remains empty. Two bottom corner fittings at one end of the tank are secured longitudinally to rigid anchor, while for the other two corner fittings, translational movement along z axis are fixed. So in principle, Ux is set as 0 for A1 and B1 while Rotz is zero for C1 and D1. However, for numerical analysis, because of insufficient number of degree of freedom, such boundary conditions would cause fatal calculation error. Thus in the simulation, the boundary condition is set as on the bottom surface of A1 and B1, Ux, Uy, Uz and Rotz are zero while on the bottom surface of C1 and D1, Rotz is set to zero. On the upper corners, Uz is set to be zero for the upper surface of A, B, C, D. According to ISO standards, a total force of 706kN is applied horizontally through the bottom apertures of the other bottom corner fittings, first towards and then away from anchor point. Thus at each end, a horizontal force of 353kN is applied.

Result and analysis

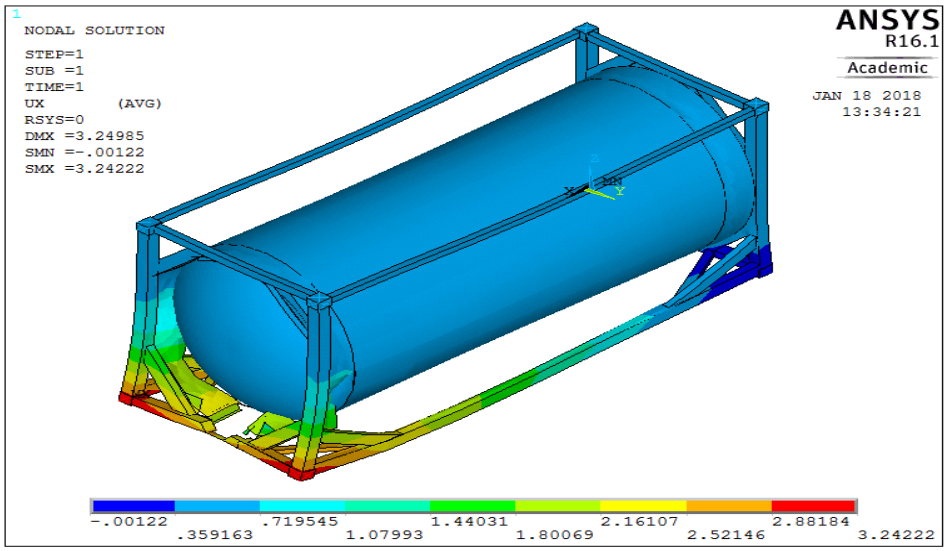

Figure 4- 6 Longitudinal displacement plot of restraint test (tension)

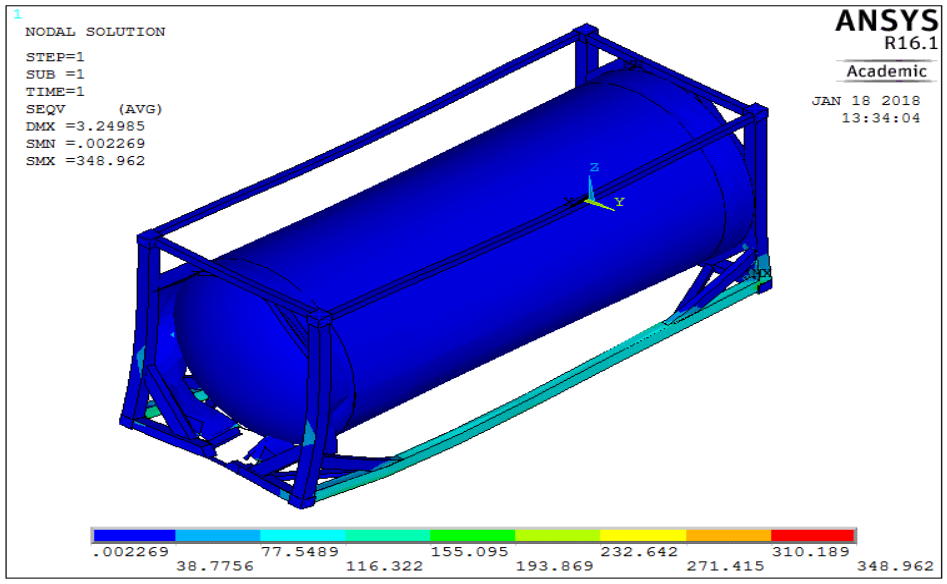

Figure 4- 7 Von Mises stress of restraint test (tension)

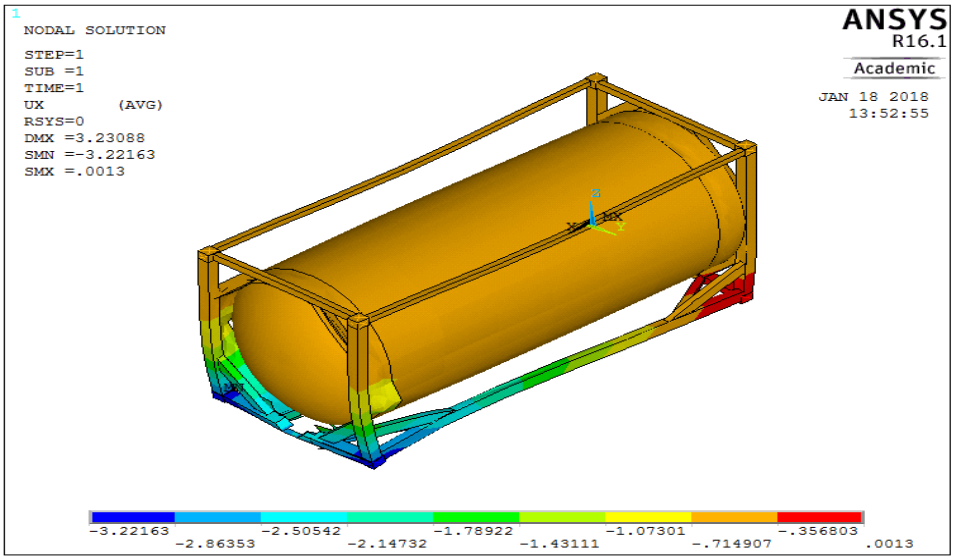

Figure 4- 8 Longitudinal displacement plot of restraint test (compression)

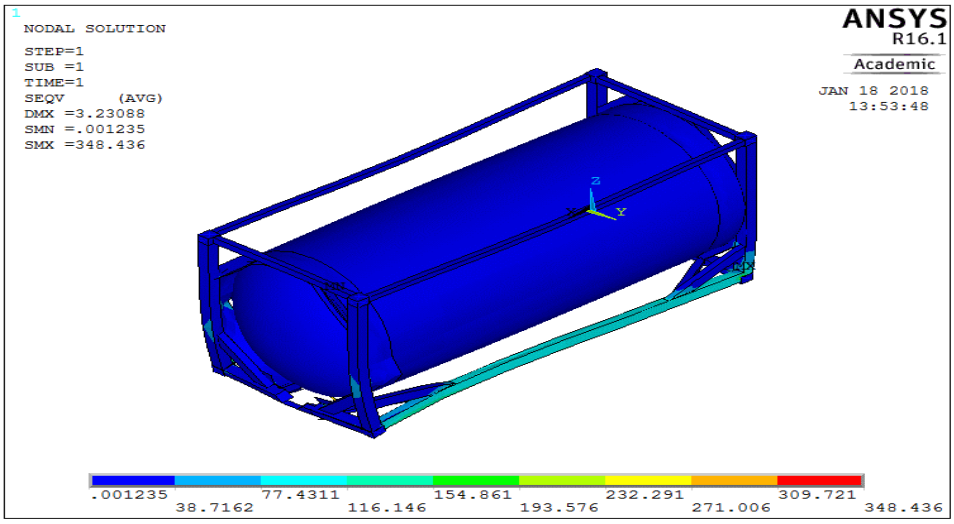

Figure 4- 9 Von Mises stress of restraint test (tension)

The comparison result is listed in table 4-4

Type of loading	Measurement	Experimental data(mm)	Simulation result(mm)
Compression	A_1-C_1	4	3.1
	B_1-D_1	4	3.1
Tension	A_1-C_1	7	3.1
	B_1-D_1	8	3.1

Table 4- 4 Result from the restraint test

From figure 4-6 and 4-8 we can find that because of the restraint, the displacement along x direction of the upper part of the structure is smaller than that of the bottom part. On the fixed end the displacement along x direction is almost zero. From figure 4-7 and 4-8 we know for most of nodes, the Von Mises stress is below 100MPa, which is far lower than the yielding stresses (170MPa for the vessel and 305MPa for the skirt). On the longitudinal frames, the Von Mises stress is also much lower than the yielding stress (345MPa). Only one node is found with Von Mises stress exceeding yielding stress and the element attached to this node is highly irregular, which indicates this error is induced by the poor quality of local mesh.

In the simulation, to guarantee the convergence of result, large-deflection effect in the static analysis is turned off. Thus in table 4-4, the deflection under tensional and compressional force should be same. The difference between measured data and simulation result shows the stiffness of the model is larger than in reality. In the experiment report, the model is over simplified and it is not clear how the data is measured. Thus the difference in experimental data between the two types of loading might result from errors in measurement.

In conclusion, the structure can withstand the restraint force.

4.3 Racking test

Racking test is designed to prove the rigidity of the container, i.e. the deformation of the container diagonals should not exceed a certain value when loaded with racking force. Based on the direction of loading, it can be further classified as transverse racking and longitudinal racking.

4.3.1 Transverse racking test

Experiment description

Transverse racking is performed with an empty container. The applied force is 150kN, first towards and then away from the top corner fitting. Due to the asymmetry of the front and rear ends, experiments should be carried out separately. In principle, when the container is loaded on one end, the lateral movement is restrained only on the bottom corner fitting diagonally opposite to and in the same end frame as a top corner fitting to which force is applied. The process is illustrated in figure 4-9

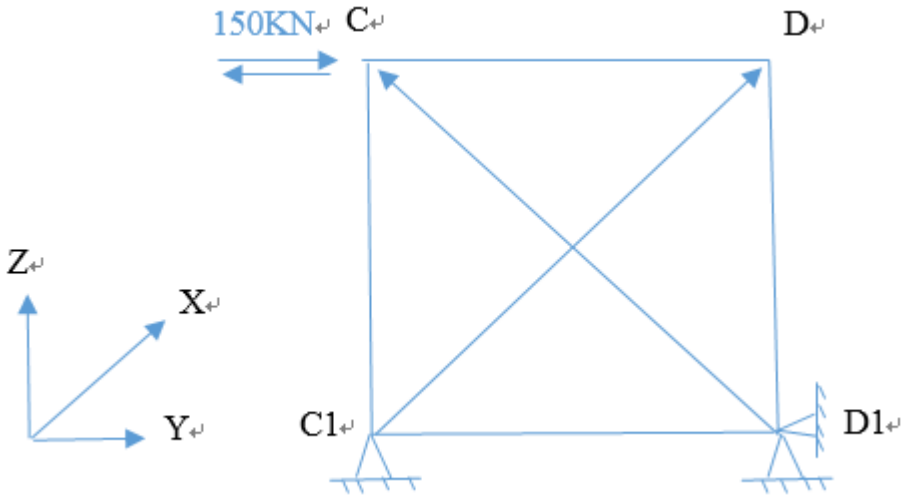

Figure 4- 10 Illustration of transverse racking test

In practice, to ensure the convergence of the result, boundary conditions are applied on all four bottom corners. The translational displacement along three directions and rotational displacement are set to be zero. That is Ux, Uy, Uz and Rotz are zero at A1,B1,C1,D1 on the bottom face and Ux, Uy, Uz and Roty are zero at D1 on the right lateral face.

4.3.1.1 Transverse racking test at rear end

Results and analysis

To begin with, the transverse racking test is done at the front end. First compression force (towards top corner fitting) is loaded then tension force (away from top corner fitting). The results are shown below.

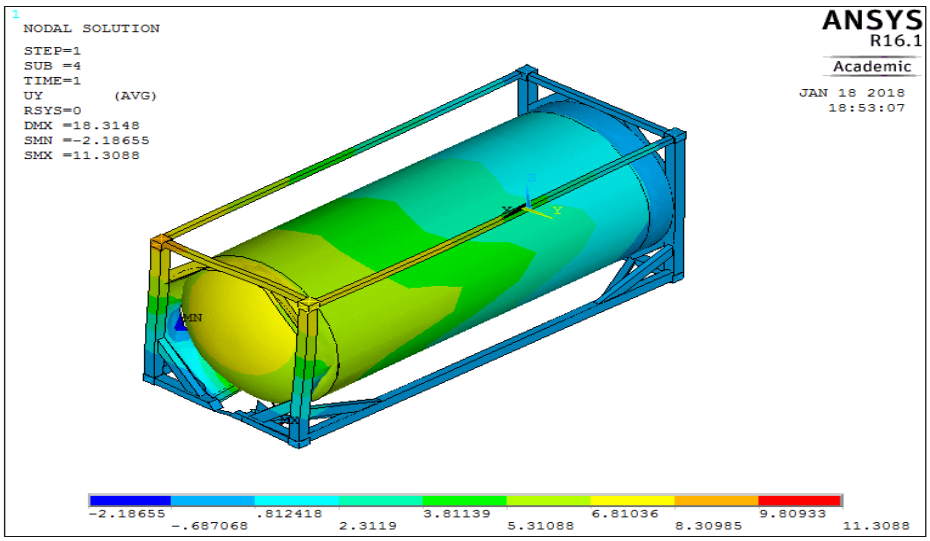

Figure 4- 11 Lateral displacement plot for transverse racking test (rear end compression)

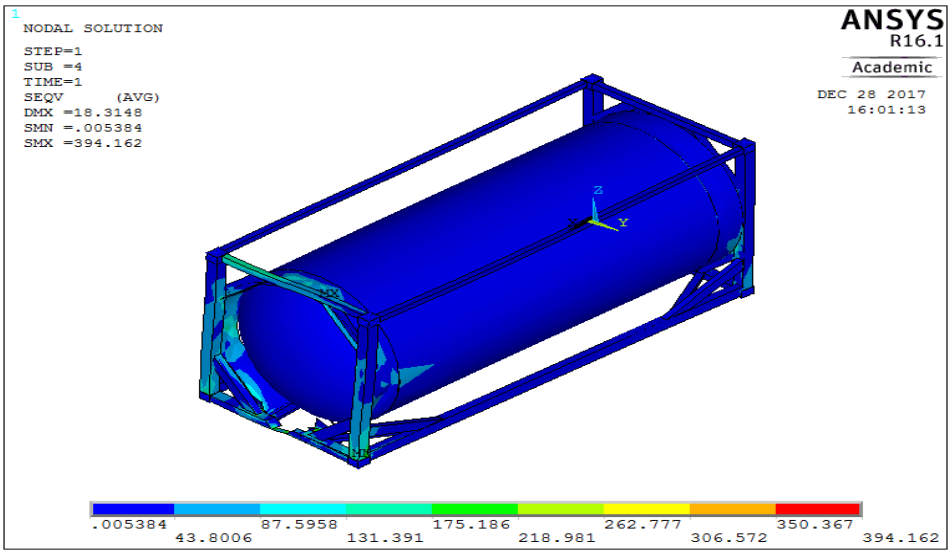

Figure 4- 12 Von Mises stress plot for transverse racking test (rear end compression)

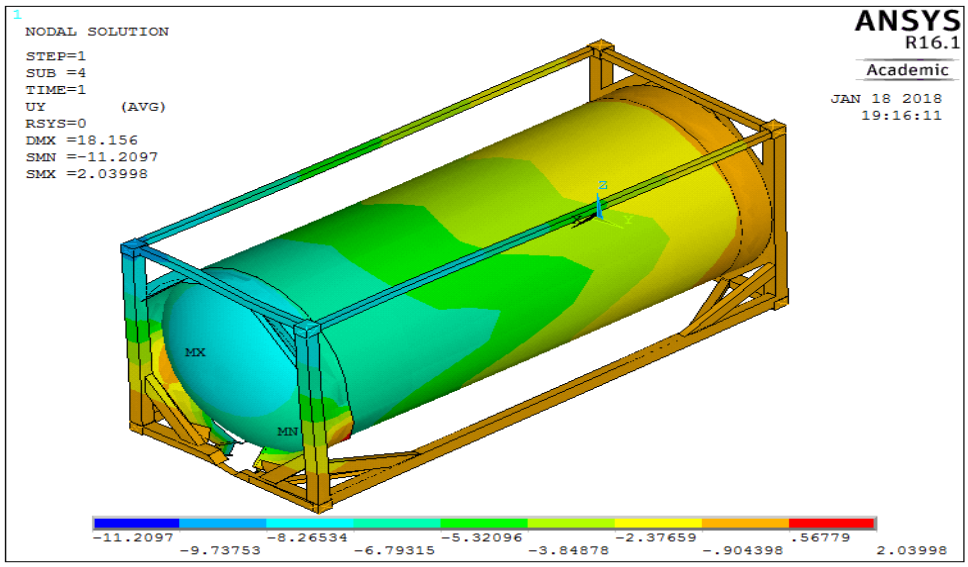

Figure 4- 13 Lateral displacement plot for transverse racking test (rear end tension)

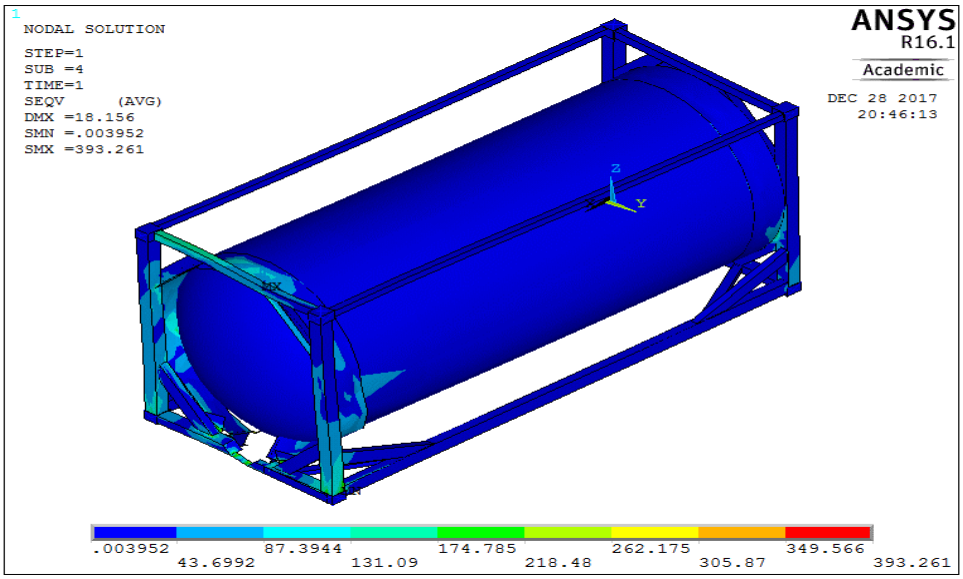

Figure 4- 14 Von Mises stress plot for transverse racking test (rear end tension)

Compression	Experimental data (before test)/mm	Simulation result(before test)/mm	Experimental data (after test)/mm	Simulation result (after test)/mm	Change (Experimental data)/mm	Change (Simulation result)/mm
C-D_1	3169	3360.94	3168	3355.09	-1	-5.85
C_1-D	3170	3360.94	3172	3366.23	+2	+5.29
Tension	Experimental data (before test)/mm	Simulation result(before test)/mm	Experimental data (after test)/mm	Simulation result (after test)/mm	Change (Experimental data)/mm	Change (Simulation result)/mm
C-D_1	3169	3360.94	3171	3366.76	+2	+5.82
C_1-D	3170	3360.94	3169	3355.67	-1	-5.27

Table 4- 5 Comparison of transverse racking test result (rear end)

	Tension/mm	Compression/mm
Upper left corner casting	-8.59	8.61
Upper right corner casting	-7.80	7.81

Table 4- 6 Lateral displacement of the upper corners

From figure 4-12 and figure 4-14 we find the Von Mises stress for most nodes are lower than the yielding stress (170MPa for the vessel, 304MPa for the skirt and 345MPa for the frames). Only a limited number of nodes where the Von Mises stress exceeds the yielding stress are found. These nodes are attached to element with irregular shapes, which indicates that the error rises from poor quality of meshing. The deformation shape in figure 4-11 and figure 4-13 match with expectation. Table 4-6 shows that for each upper corner fitting at the rear end, the lateral displacement (along y direction) under these two types of loading is more or less same, which means no plastic deformation occurred during the test.

In table 4-5, there is a huge difference between the diagonal length from experimental data and simulation result. This results from the difference in measuring points in the experiment and simulation. In the simulation, the diagonal length is calculated based on nodes in the middle of the front surface of the four corner castings at the discharge side. However, in the experiment report, the measuring points are at corners of the simplified model, which didn't specify the exact location. In fact, in the simulation model, the diagonal can vary from 3164.7mm to 3557.7mm, depending on how the diagonal is defined. Thus the difference in both the diagonal length and the length change are acceptable. Due to the slight difference of lateral displacement of the two upper corner castings, C-D_1 under compressional force should be slightly different from C_1-D under tensional force, which also matches the result. Thus the structure can withstand lateral racking force at the rear end.

4.3.1.2 Transverse racking test at front end

Results and analysis

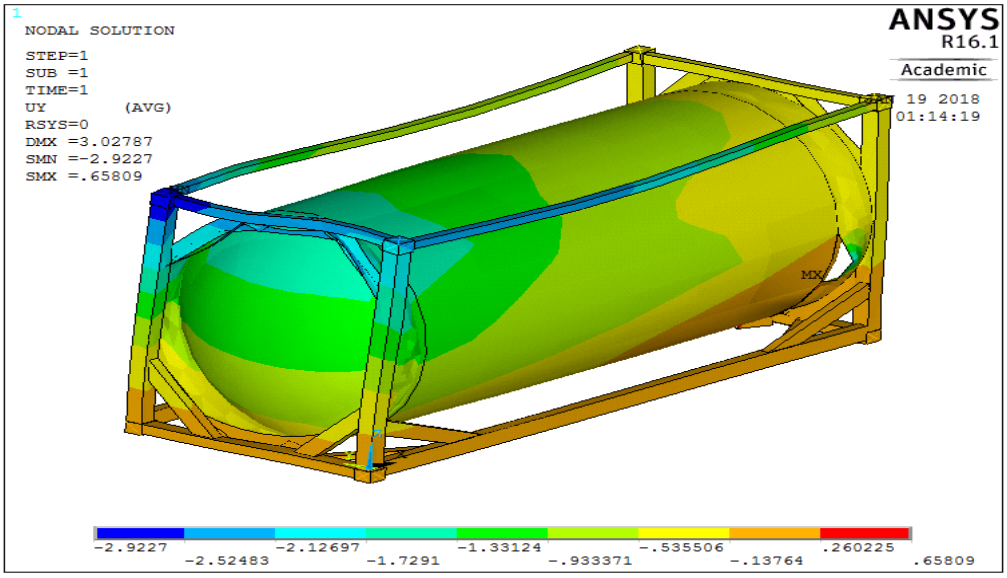

Figure 4- 15 Lateral displacement plot for transverse racking test (front end compression)

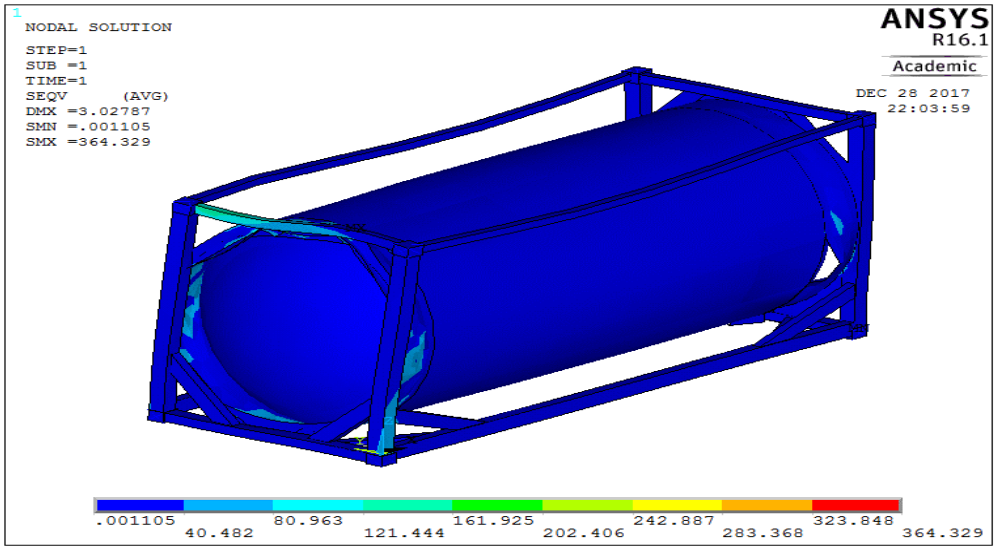

Figure 4- 16 Von Mises stress plot for transverse racking test (front end compression)

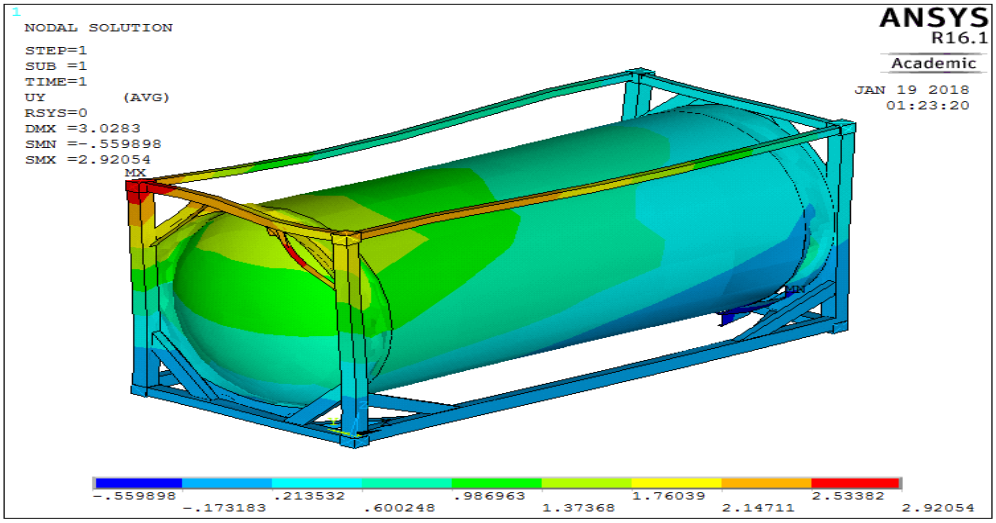

Figure 4- 17 Lateral displacement plot for transverse racking test (front end tension)

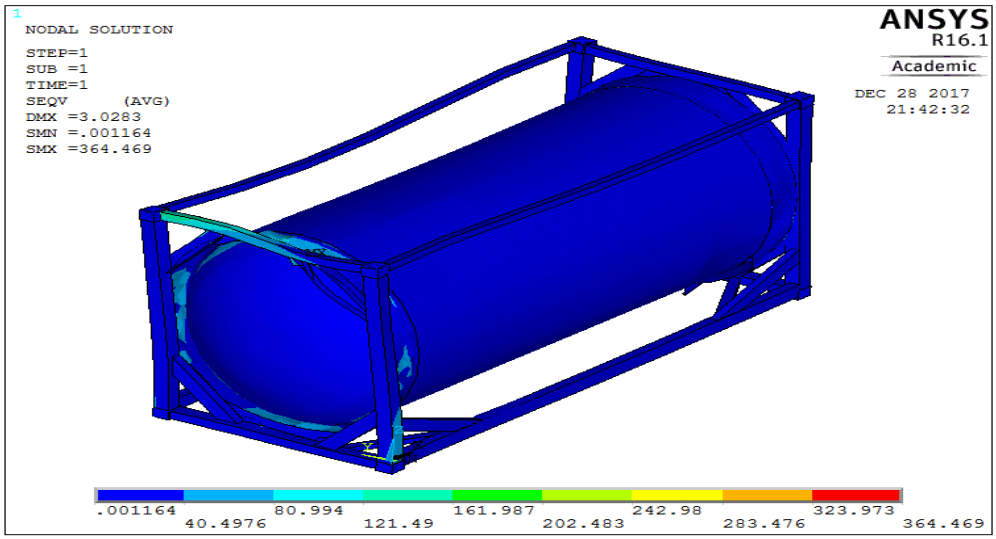

Figure 4- 18 Von Mises stress plot for transverse racking test (front end tension)

Compression	Experimental data (before test)	Simulation result(before test)	Experimental data (after test)	Simulation result (after test)	Change (Experimental data)	Change (Simulation result)
C-D_1	3170	3360.94	3168.5	3359.11	-1.5	-1.93
C_1-D	3168	3360.94	3170	3362.35	+2	+1.41
Tension	Experimental data (before test)	Simulation result(before test)	Experimental data (after test)	Simulation result (after test)	Change (Experimental data)	Change (Simulation result)
C-D_1	3170	3360.94	3171.5	3362.86	+1.5	+1.92
C_1-D	3168	3360.94	3167	3359.52	-1	-1.42

Table 4- 7 Comparison of transverse racking test result (front end)

	Tension/mm	Compression/mm
Upper left corner casting	-2.84	2.84
Upper right corner casting	-2.09	2.09

Table 4- 8 Lateral displacement of the upper corner castings (front end)

From figure 4-16 and figure 4-18 we find the Von Mises stress for most nodes are lower than the yielding stress (170MPa for the vessel, 304MPa for the skirt and 345MPa for the frames). Nodes with highest Von Mises stress are found at the connection of flange and skirt. The elements attacked to the nodes are high irregular, which indicates that the error might rise from poor quality of meshing. The deformation shape in figure 4-15 and figure 4-17 match with expectation. Table 4-8 shows that for each upper corner fitting at the rear end, the lateral displacement (along y direction) under these two types of loading is more or less same, which means no plastic deformation occurred during the test.

As it is with chapter 4.3.1.1, the differences in table 4-7 are because of similar reasons. Hence, the difference in both the diagonal length and the length change are acceptable. By comparing the result in table 4-8 and table 4-6, we find the lateral displacement at the front end is lower than that of the rear end, which means the stiffness of the rear end is lower than that of the front end due to too much openings of the structure. In conclusion, the front end of the structure can withstand lateral racking force.

4.3.2 Longitudinal racking test

The longitudinal racking test shall be carried out to prove the ability of a container to withstand the longitudinal racking forces resulting from ship movement.

In this test, longitudinal restraint shall be provided only at a bottom corner fitting diagonally opposite and in the same side frame as a top corner fitting to which the force is applied, which means Ux, Uy, Uz and Rotz are zero only on the bottom surface at C1 and D1 if A and B are loaded. However, to guarantee the convergence of the calculation, the abovementioned boundary conditions are applied on the bottom face of all four bottom corner castings.

The loading of 75kN is applied separately to each of the top corner fittings on the end of the tank container in lines parallel both to the base of the tank container. It is applied first towards (compression) then away from (tension) the top corner fittings.

Results and analysis

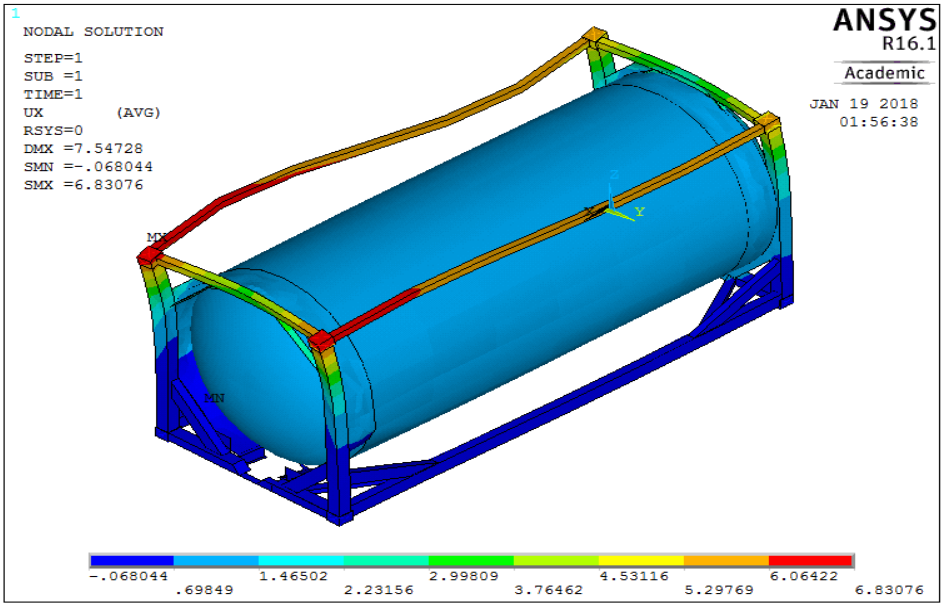

Figure 4- 19 Longitudinal displacement plot for longitudinal racking test (tension)

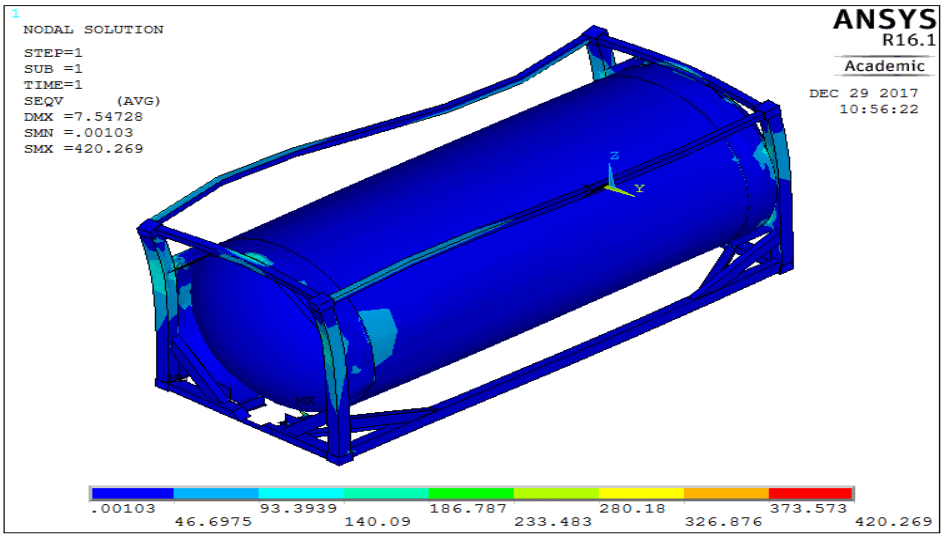

Figure 4- 20 Von Mises stress for longitudinal racking test (tension)

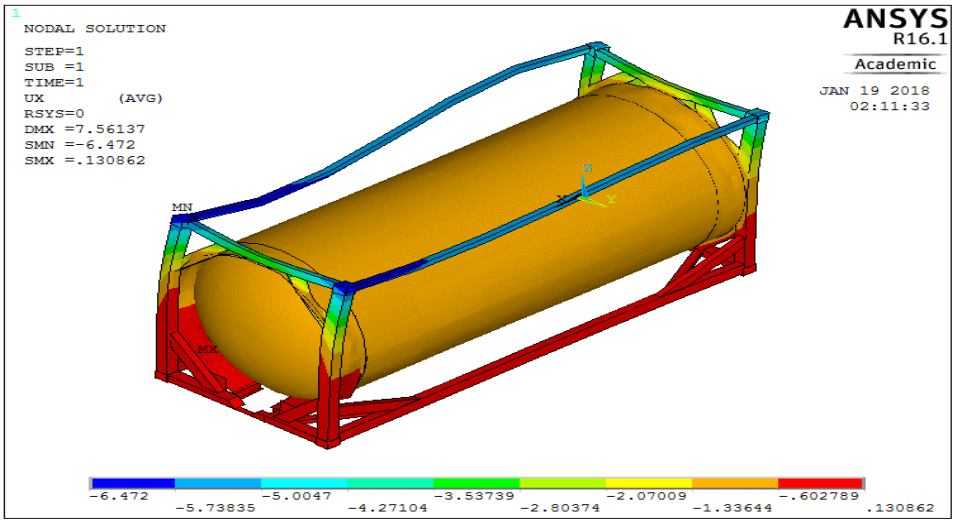

Figure 4- 21 Longitudinal displacement plot for longitudinal racking test (compression)

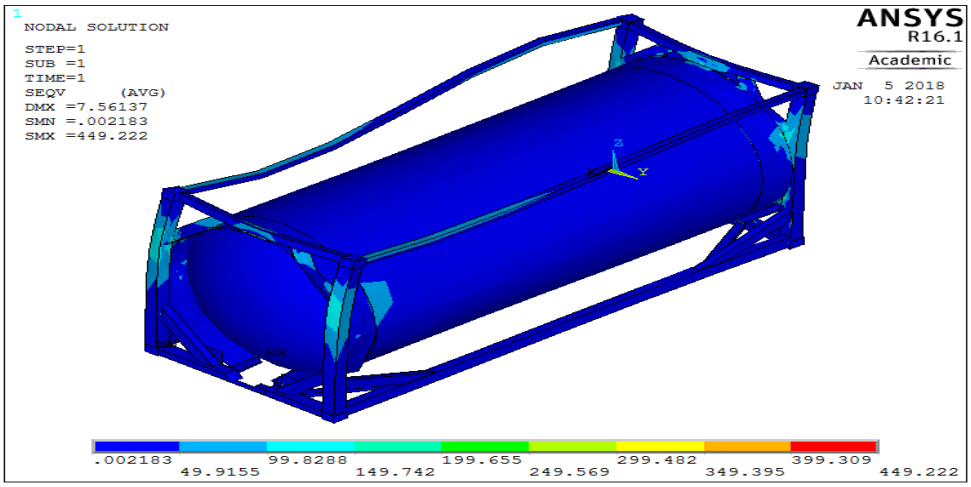

Figure 4- 22 Von Mises stress for longitudinal racking test (compression)

Longitudinal racking test	Experimental data (mm)	Simulation result (mm)
Tension	AC=5 BD=5	AC=5.1 BD=5.2
Compression	AC=11 BD=8	AC=4.8 BD=4.9

Table 4- 9 Comparison of Longitudinal racking test result

Figure 4-20 and 4-22 shows that for most of the nodes, Von Mises stress is lower than 170MPa, which is lower than the lowest yielding stress (170MPa) of all structure parts. Deformation shape in figure 4-19 and 4-21 match with expectation. Due to the resistance of the vessel, when loaded with compressional force, the displacement of the upper corner casting should be slightly smaller than when loaded with tensional force. In the experimental data, however, it shows the opposite trend, which might be caused by a different measurement.

4.4 Lifting test

Lifting tests are carried out to prove the tank container is able to withstand lifting force. In practice, there are two types of lifting tests. One is to lift from four bottom corners and the other one is to lift from four top corners.

4.4.1 Lifting from four bottom corner fittings

As it is implied by the name, in this test, the container is lifted from its four bottom corner fittings by means of lifting devices bearing on the bottom corner fittings only and attached to a single transverse central spreader beam above the container. The lifting process is illustrated in figure 4-23

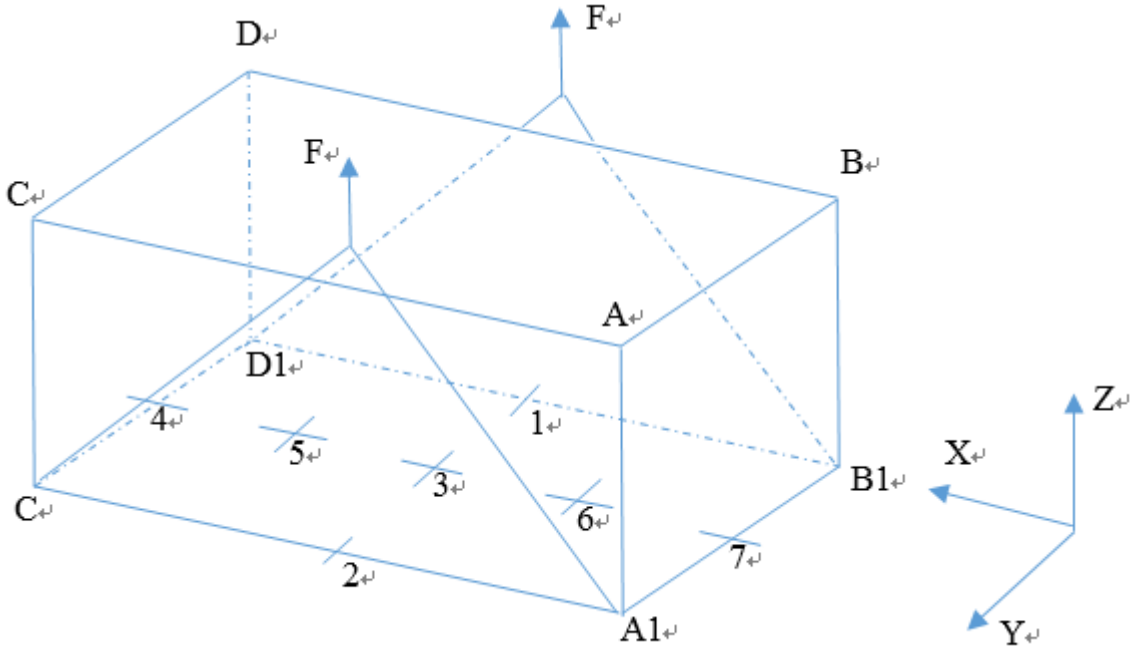

Figure 4- 23 Illustration of lifting from four bottom corner fittings

The combined mass of the tank and test load is 706kN, which brings a horizontal force and vertical force of 176kN to each bottom corner. During the test, no significant acceleration or deceleration forces are applied. For the container of interest, lifting force is applied at 45°to the horizontal tank container.

In reality, the container will reach equilibrium of force at any location. However, in ANSYS, the boundary conditions must be specified to eliminate singularity. Thus the boundary condition is at four upper corner fittings, the translational displacement along three directions and rotational displacement along z direction is zero. That is to say, on the upper face of A, B, C, and D, all six degrees of freedom are zero. Both the lifting forces and gravity are applied at the right place in this model. The results are shown below

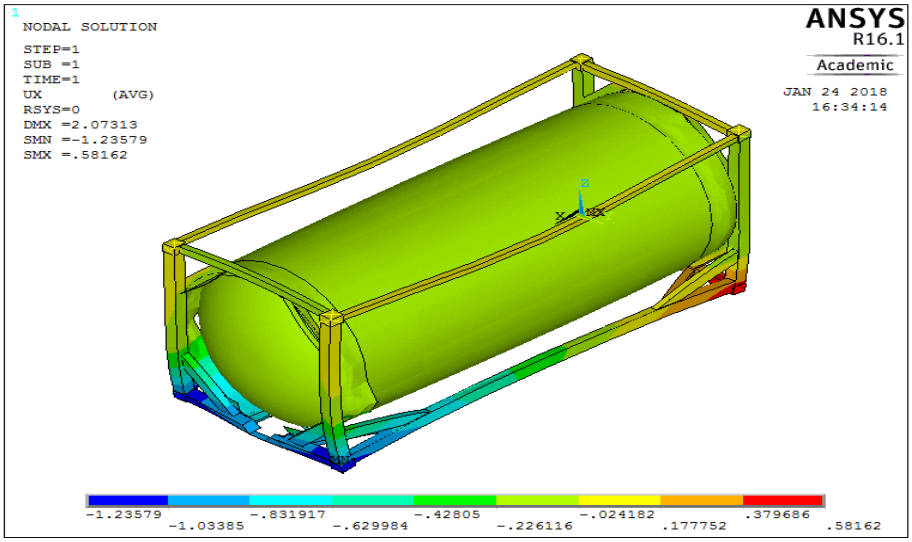

Figure 4- 24 Longitudinal displacement plot for lifting test (lifting from bottom)

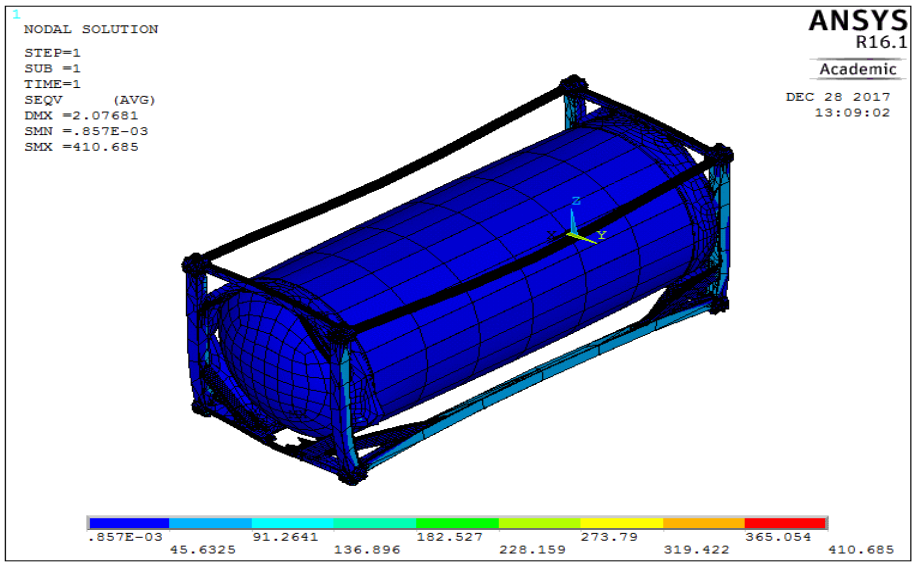

Figure 4- 25 Von Mises stress plot for lifting test (lifting from bottom)

From figure 4-25 we find that for the majority of the elements, the Von Mises stress is less than 170MPa, which is less than the yielding stress. When the upper corners are fixed, the lifting force, which has a horizontal and vertical component, acts as a bending moment, which causes the deformation shape as expected. In conclusion, the structure can withstand lifting force at the bottom and the structure is in elastic phase.

4.4.2 Lifting from four top corner castings

In this test, the container is lifted through four top corner fittings. The lifting process is demonstrated in figure 4-26

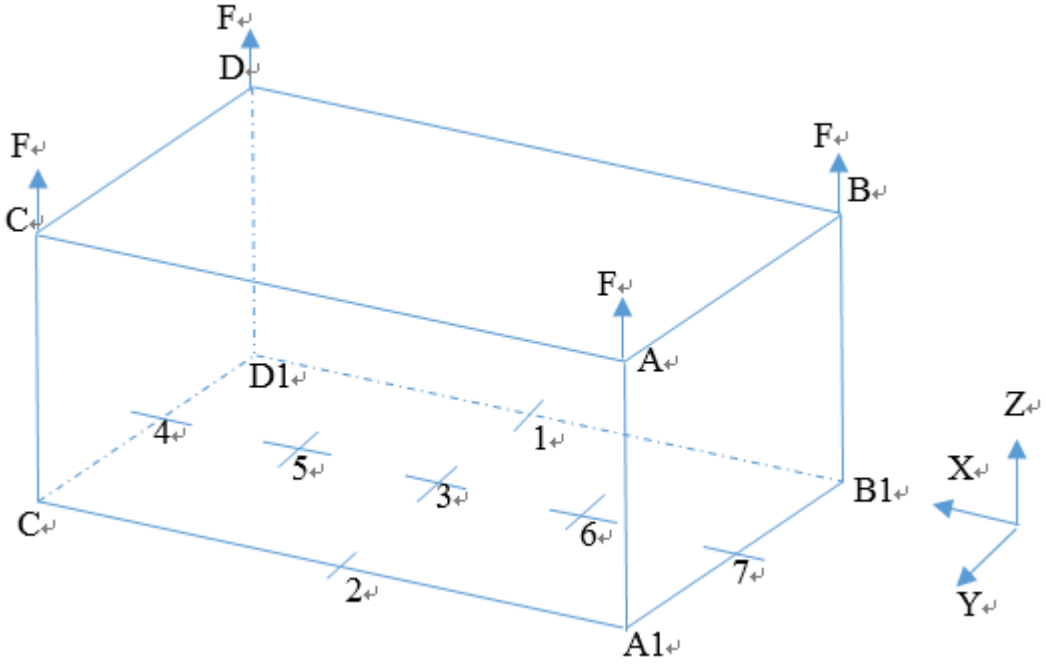

Figure 4- 26 Illustration of lifting from four upper corner fittings

The combined mass of tank and test load is 706kN, which means a vertical lifting force of 176kN on each upper corner.

Similar to the previous testing, the translational and rotational displacement of nodes on the bottom face of the four bottom corners are set to be zero to reach a converged result, i.e. Ux, Uy, Uz, Rotx, Roty, Rotz on the bottom face of A1, B1, C1, and D1 are zero. The lifting forces and gravity are applied correctly. The results are shown below

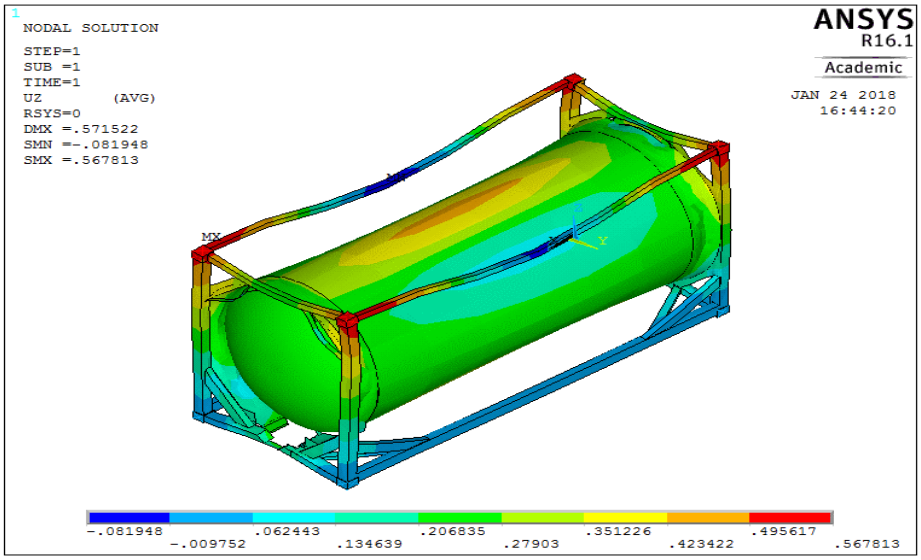

Figure 4- 27 Vertical displacement plot for lifting test (lifting from top)

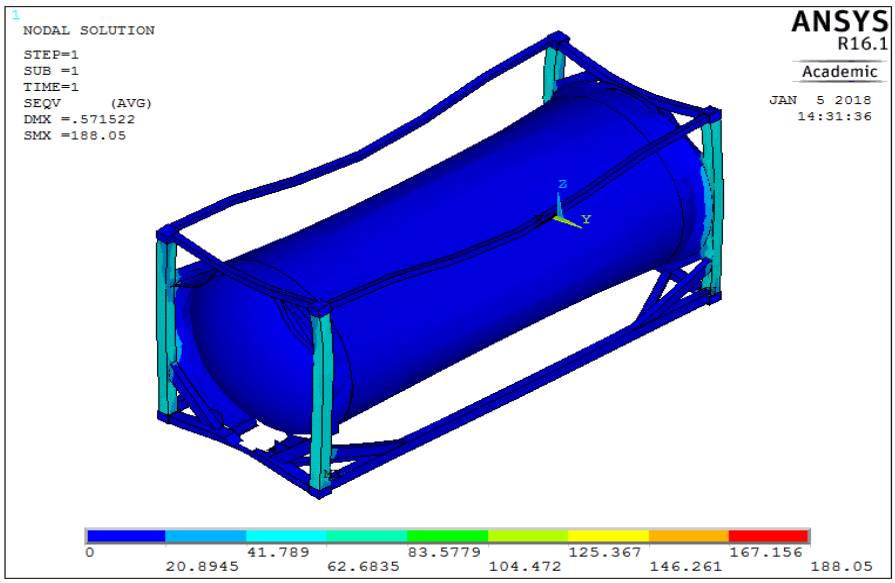

Figure 4- 28 Displacement vector for lifting test (lifting from top)

Figure 4-28 shows that the Von Mises stress is significantly lower than yielding stress. Due to the restraint on four bottom corners, when the four upper corners are lifted, it lifts the vessel through the connections. Thus the middle part of the bottom lateral frames are lifted as well, which leads to the deformation shape. The result shows that the structure can withstand lifting force from upper corners. .

Chapter 5 FEM Simulation

The fatigue analysis of the skirt weld joint requires two models, namely the global and the local model. This is because of the limit of the model and related computation time. Both are established with ANSYS APDL. The global model is verified with experimental data as explained in previous chapter. Calculation and result on the local model will be presented in this chapter.

The complete analysis procedure is divided into three parts, namely the global model calculation, the local model calculation, and the post processing. In the global model calculation period, a range of acceleration data is selected as input. After the calculation on the global model, a group of nodes that satisfies the cut-boundary condition is selected and translational displacements (along 3 directions) are extracted and used as the boundary conditions for the local model. The local model calculation is then performed with the boundary conditions and the same acceleration input. After that, in the data processing period, firstly, several paths and nodes are selected to obtain stress history, which is used to calculate variable amplitude hotspot stress. Then the rain-flow counting method is applied to obtain constant amplitude hotspot stress, followed by a calculation of the true constant amplitude stress for a longer period based on stress distribution. In the end, with the right S-N curve, the fatigue damage factor is calculated for each line of interest. The whole procedure is shown in figure 5-1

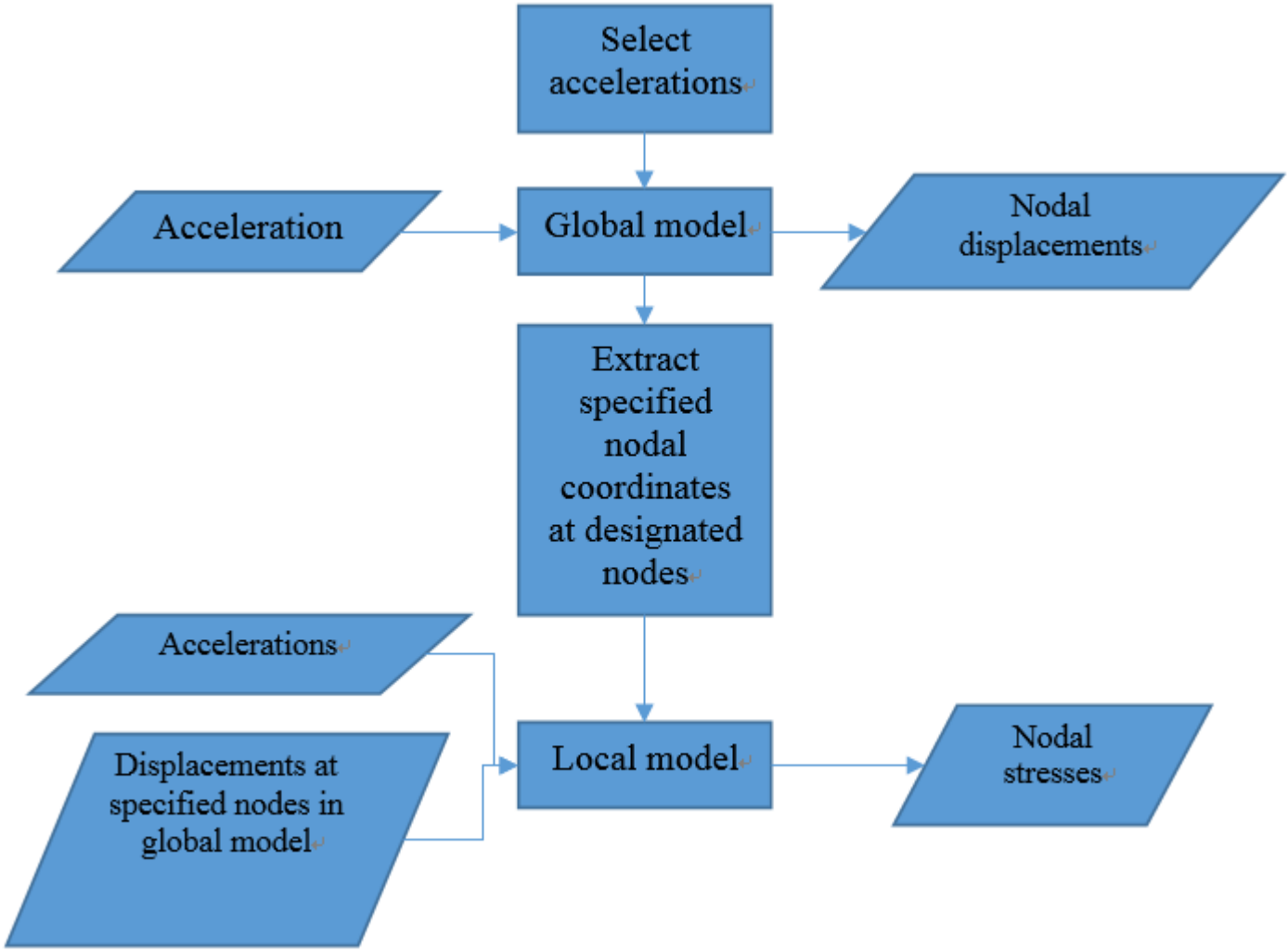

Global and local model calculation procedure

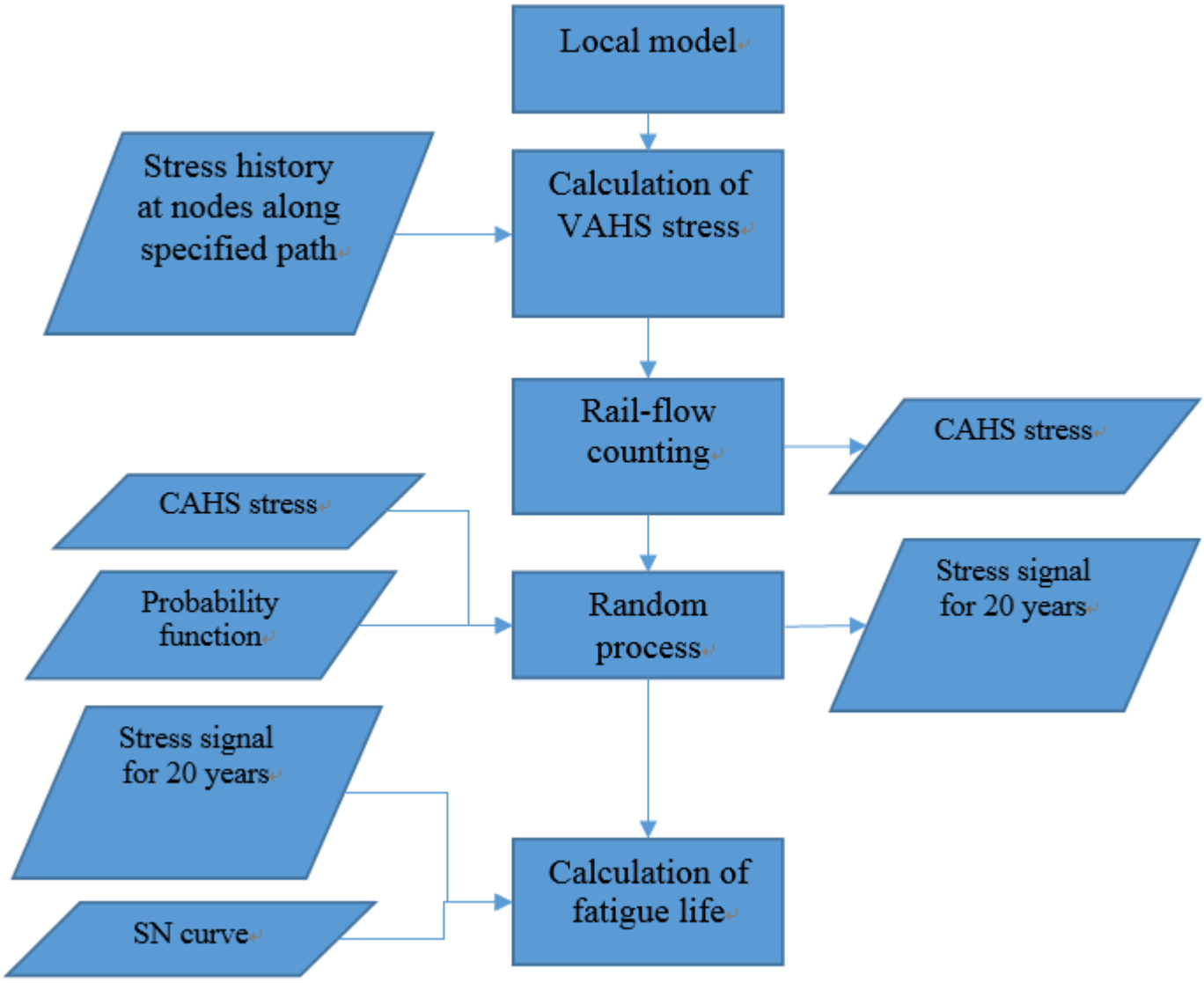

Result processing period

Figure 5- 1 Fatigue analysis flow chart

5.1 The input selection

The train acceleration data is provided by a Chinese manufacturer based on experiments. The experiments are conducted on a short distance of railway in China. A cellphone is used to record accelerations from three directions of translation. The sampling frequency is 100Hz. Total running time is 52min50s. Due to a loss of a few samples, total sampling number is 316164.The experiment condition is shown in figure 5-2

Figure 5- 2 Setup of the experiment

From figure 5-2 we can see the container is attached to the railway transportation car through anchor pads at four bottom corners. The cellphone is attached to the lower frame near the bottom corner to avoid influence from heights, thus reflecting the acceleration of the train. The sensitivity and reliability of cellphone sensor has been validated by other agencies such as Marin. The experiment is carried out on the railway between Lutai and Tianjin, China. Maximum speed on the railway is 140km/h. Since this railway is no longer used for freight transport, no further data are provided by the company.
The x,y and z acceleration in time domain is shown in figure 5-3. Speed of the train during test is plotted in figure 5-4.

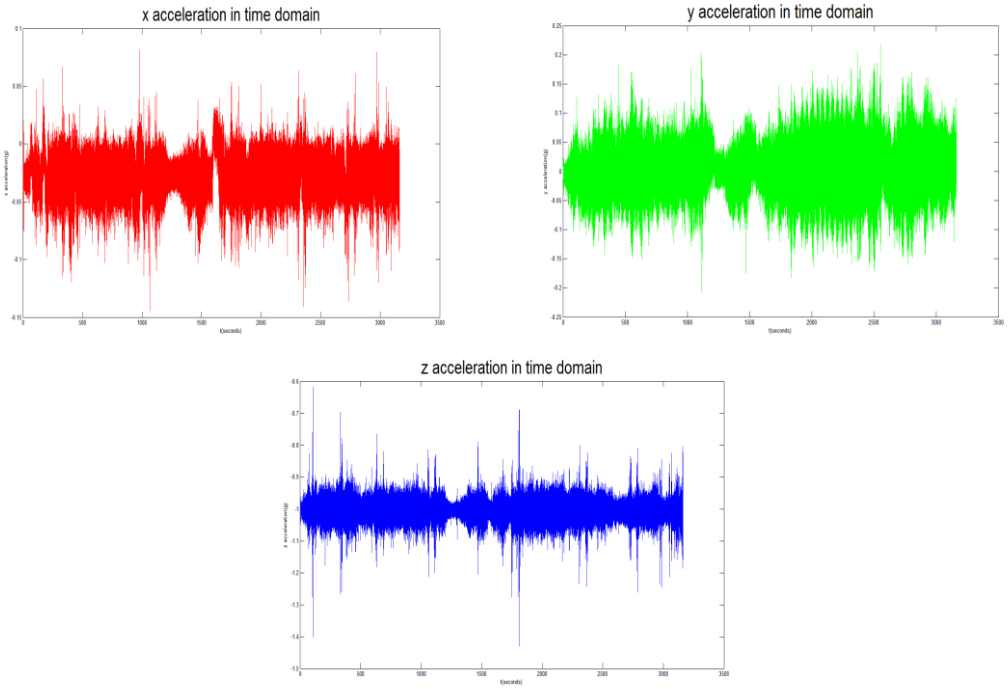

Figure 5- 3 Acceleration data from experiment

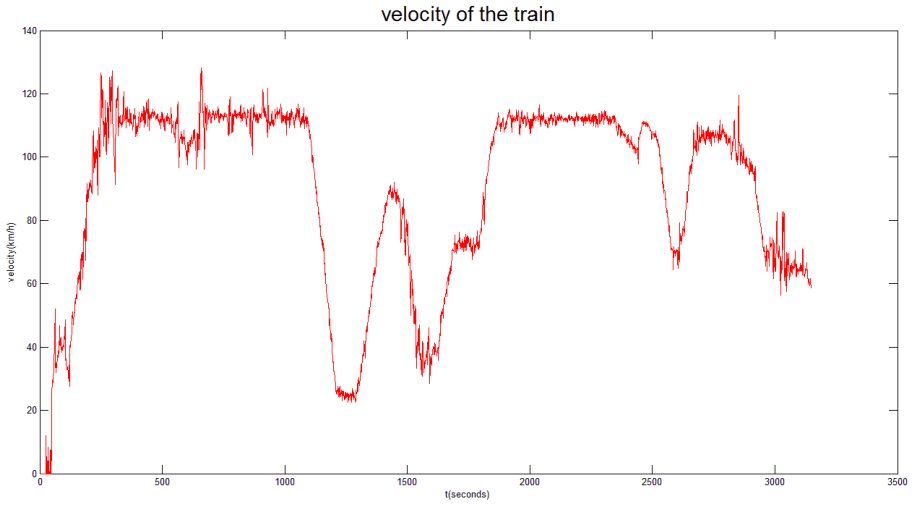

Figure 5- 4 Speed of the train during test

Note that in the measurement of z direction, acceleration of -1 corresponds to gravity. In later calculation it is reversed because the positive direction defined in the software is different from the measurement.

Figure 5-4 contains train speed from 0 to 125km/h. It covers speed for sprint period, normal transportation as well as deceleration period. Sample frequency for train speed is 1Hz. Thus the complete sample data is considered as typical for normal railway transportation. Therefore acceleration value should cover all periods.

For the sake of accuracy of the calculation, the input should include as many samples as possible. However, as the number of sample increases, the space required to store the data increases significantly, so does the calculation time. For example, to store the result for 1800 samples, 120GB of space is required and the calculation for global model would take 4 hours. The gain of accuracy doesn't compensate the loss of space and time. Thus, after a few trails, given the limitation of computer storage and calculation time, only 300 samples, which is equal to an input of 5 minutes, are selected.

After the decision of input size, the next concern is to decide which data should be included in the input file. Due to the high sampling frequency, a lot of samples in the data base are intermediate points, as illustrated in figure 5-5

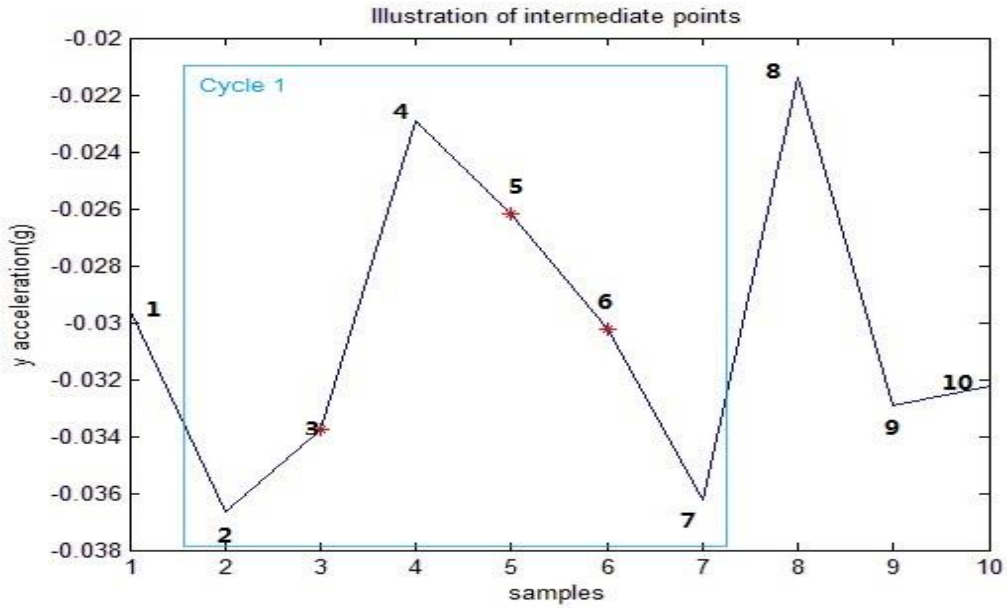

Figure 5- 5 Illustration of intermediate points (red dots)

The samples between a peak and a valley is considered as an intermediate point. The rest are peaks and valleys. For example, point 3, 5 and 6 in figure 5-5 are intermediate points while point 1, 4, 8, 10 are peaks and point 2, 7, 9 are valleys. Cycle 1 can be represented either by point 2, 4, 7 or by point 2 to 7. In the latter way, for a fixed number of input, since the intermediate points are taken into account, the number of peaks and valleys will be reduced, thus less cycles will be included in the input. To avoid that, before selecting the input, intermediate points are removed.

The output of fatigue damage calculation is heavily dependent on the input. To provide reference for design improvement, it is important to know which input will generate the maximum damage, i.e. the most severe calculation. Therefore, to calculate fatigue damage for the most severe situation, firstly, a MATLAB file is created to exclude those intermediate points, leaving behind only peaks and valleys. Secondly, 150 highest peaks and 150 minima of the whole data set are chosen and arranged in a way to create maximum acceleration range. Finally, the assembled input data is compared to data provided by a South African company. After the comparison, it is believed that in the Chinese data, the peaks in vertical acceleration are not high enough and the average vertical acceleration is much lower. In other words, the Chinese data is too conservative and will underestimate the vibration of containers. Therefore it is agreed to double the amplitude of the vertical acceleration. Since the original point of vertical acceleration is 1g, which corresponds to gravity, the formula to modify the input is listed below,

$$Az' = (Az-1)*2+1$$

Where Az is the vertical acceleration from the data set obtained from experiment and Az' is the input vertical acceleration for the FE analysis. The unit is g.
The final input is demonstrated in figure 5-6

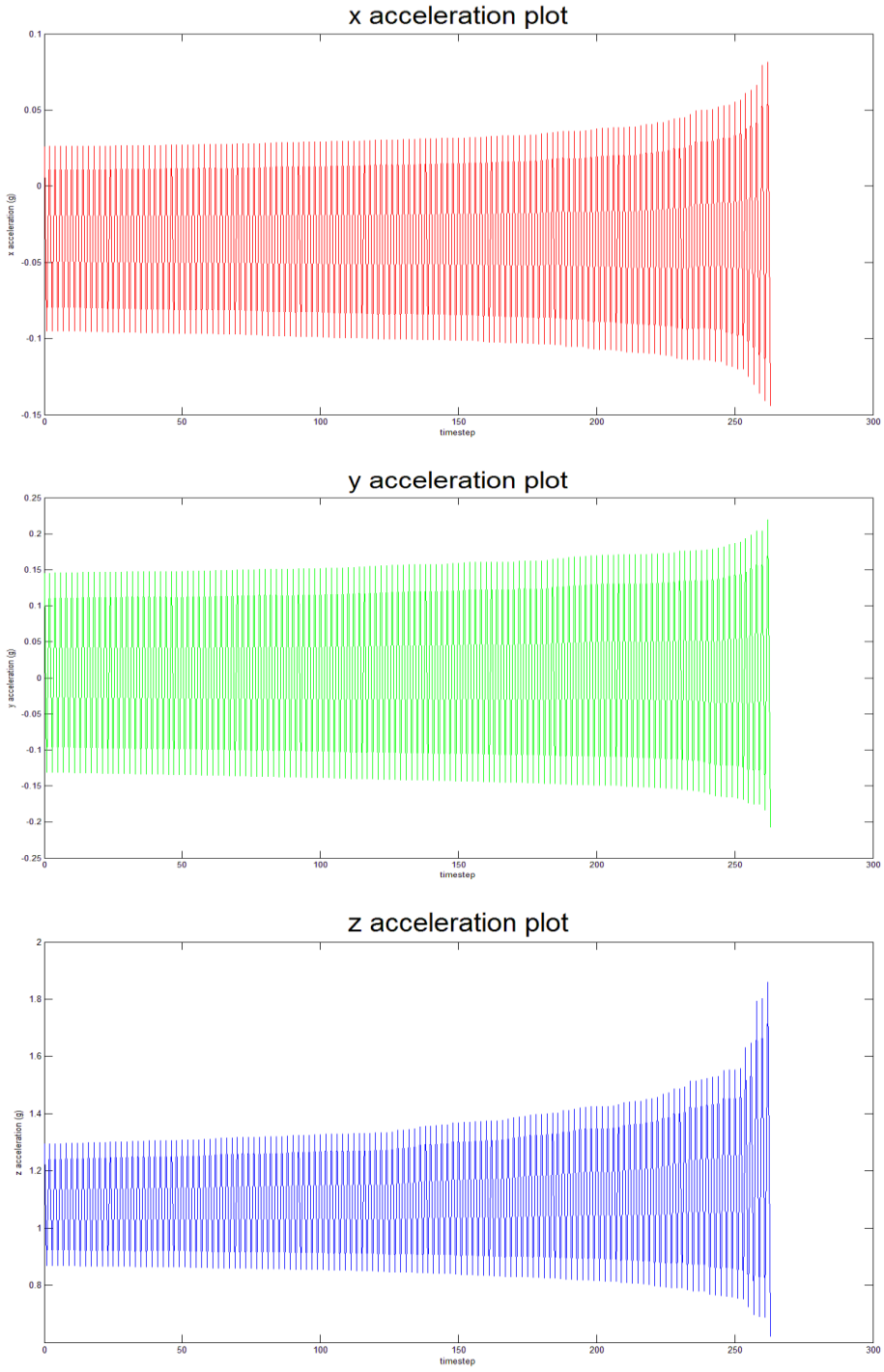

Figure 5- 6 Final input (acceleration along x, y and z direction)

5.2 FEM models

5.2.1 The global model

A tank container consists of several structural components, for example, the vessel, the skirt, the frame, the corner castings, etc. The global model should include all the necessary structural parts and ignore unimportant components such as ladders and decorations.

For the establishment of the global model, three approaches are considered. The first one is established by a previous student. In this model, the frames are modelled as hollow sections with beam 188 elements while the vessel and the skirt are modelled as plates with shell 181 element. This model is neat and easy. However, because of the numerical description of beam element, in general, the result obtained are not presented as

stress history, which means a fast qualitative calculation, which is required for fatigue life calculation, is impossible. Hence it is suggested to establish the model by another method.

The second one is modelled with solid element. The geometry is imported from Solidworks using a sketch by a manufacturer. When importing the entire geometry from Solidworks to ANSYS, sometimes volumes/solid parts are created automatically. If not, they can be generated by looping through areas which are connected to a specified area.

This method is sounds convenient, however, there are a number of significant drawbacks when it comes to practice. Firstly, some volumes created in this way are unnecessary or unwanted. This is because for one area, there could be more than one loop that starts from it and loops through surrounding areas. Due to the size of model and the amount of areas, it is difficult to identify which area is to loop from and which area should be included in the loop one by one. Secondly, for a model with large number of element surfaces, looping with each area one by one is quite time-consuming, letting alone errors that might arise from it. Thirdly, some details in the Solidworks model cause difficulty and errors in meshing. When designers developed the model in Solidworks, a lot of details are included to illustrate the model more clearly. However, those details are not desired when imported to ANSYS, for the irregularities in lines and areas make it difficult to obtain a fine-meshed result. Last but not least, combining the global model and local model is difficult. When completing the whole calculation procedure, both a global model and a local model are required. On the common boundaries, a so called cut-boundary condition should applied to combine both models, which means that on the common boundary, there should be as many ‘common nodes’ as possible. When the model is imported from Solidworks, it is difficult to obtain a well-defined cut-boundary, which causes problems in proceeding calculations. Due to those drawbacks, it is difficult to mesh and verify the global model and obtain correct result. After consulting experts in FE modelling, it is concluded that the sub-modelling technique, as well as using displacement from global model as boundary conditions for local model directly, is most likely to succeed in a path-independent calculation or static calculation. For a non-linear transient analysis which is path dependent, it is not advised to perform this boundary transition on a model built with tetrahedron element. Thus this method is abandoned after a few trials.

The abovementioned drawbacks of the second model bring us to the last model, an all-shell element model, which is used in this calculation. Shell 188 element is used to model every part as a plated structure. The biggest difficulty in creating this model is the connection between the skirt and the frame. For most of the connections, one plate is connected to several neighboring plates which are perpendicular to it and doesn’t penetrate it. In some cases, the projection of the neighboring area to one plate is a closed graph (seen in figure 5-7) while in other cases, the projection is a group of curves (figure 5-8).

In ANSYS APDL, Boolean operation is applied to glue these areas. For the convenience of calculation and meshing, as well as convergence of the result, automatic mesh is applied as each line is divided into six elements. In this mesh, mapped mesh is conducted where it is possible while free mesh is performed elsewhere. At the connection part the elements still look irregular (figure 5-9) but it doesn’t cause much problem for further calculation. A few different mesh are found feasible, but a random division of the lines might cause the failure of meshing, thus causing the whole calculation to fail. Figure 5-7 to figure 5-9 illustrates examples of abovementioned features.

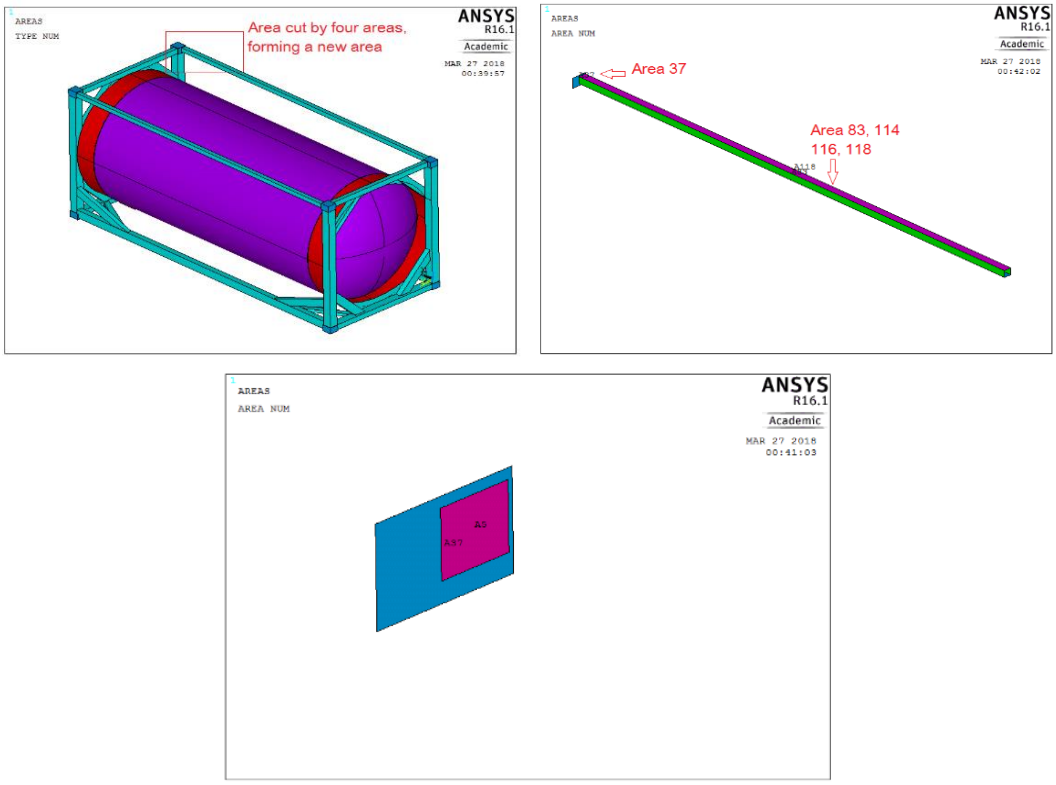

Figure 5- 7 Example of closed-graph projection

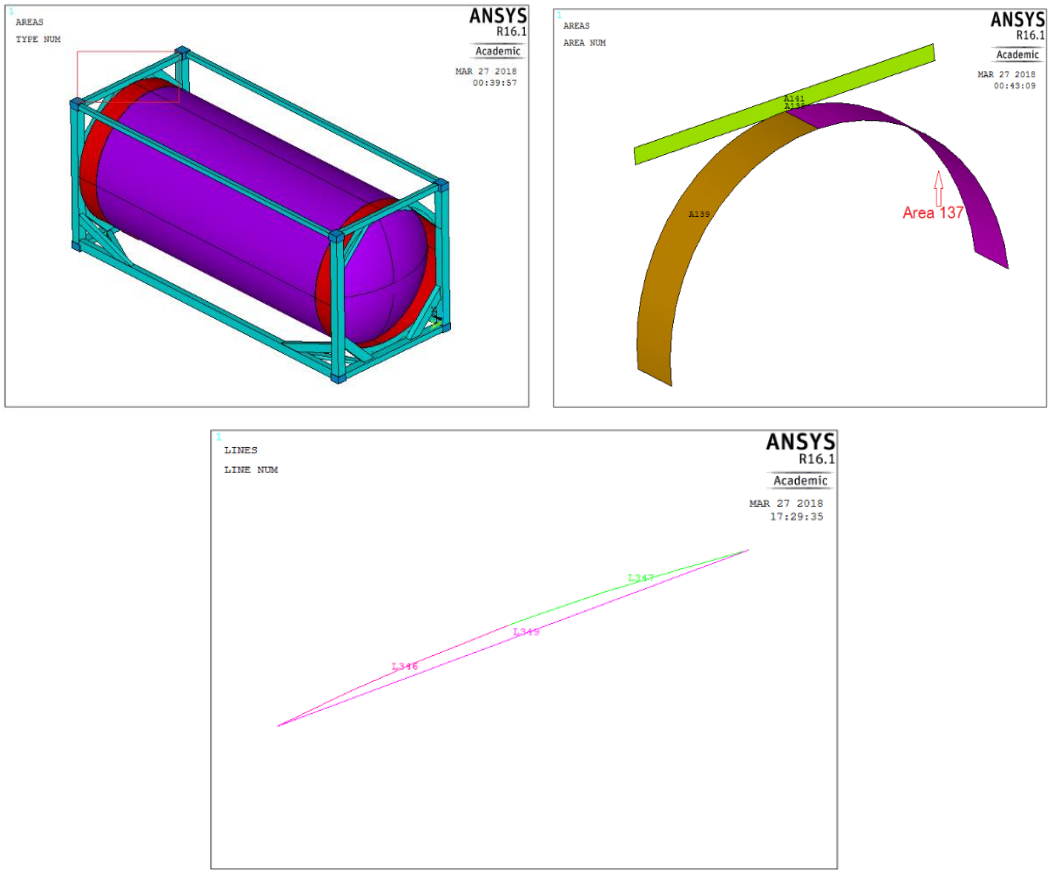

Figure 5- 8 Example of open-graph projection

Explanation of the figures

From figure 5-7 we can see, the projection of area 83, 114, 116, 118 to area 37 is a closed figure, i.e. a square. When area 37 is cut by these four areas, a new area 5 is generated.

From figure 5-8 we can see, the projection of area 137 and 139 to area 141 is not a closed figure, i.e. two lines. When area 141 is cut by these two areas, a new area 138 is formed by the two lines and original boundaries.

The two abovementioned examples have same type of connection but they should be treated differently in FE modelling.

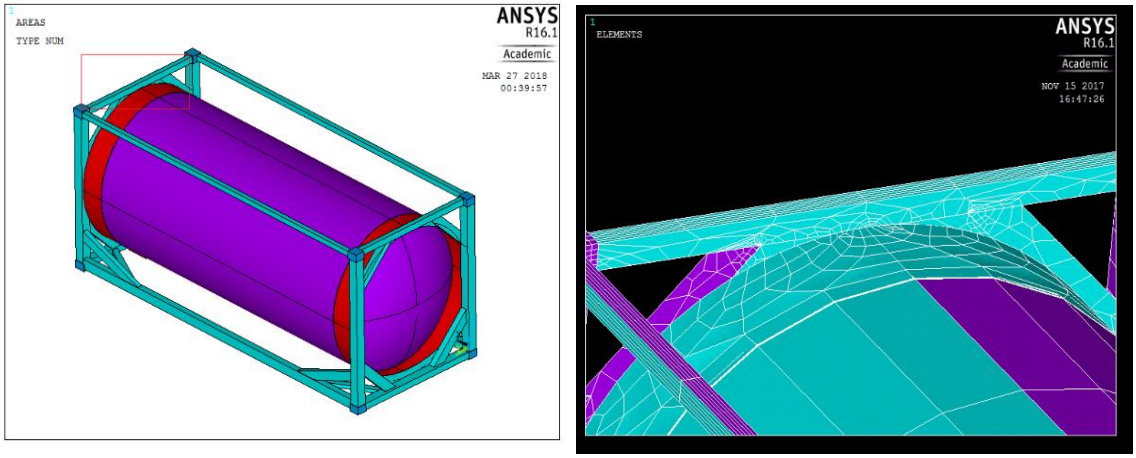

Figure 5- 9 Example of irregular elements

Figure 5-6c shows the irregular shape of the elements at the connection. When connections are established, some of the original lines will be cut by lines attached to other areas. As a result, shorter lines will be created and new areas are formed out of these short lines. After meshing, small elements will appear in the new areas while in the areas, elements will be larger. In the end, the elements look irregular.

The unmeshed global model and meshed model are shown in figure 5-10

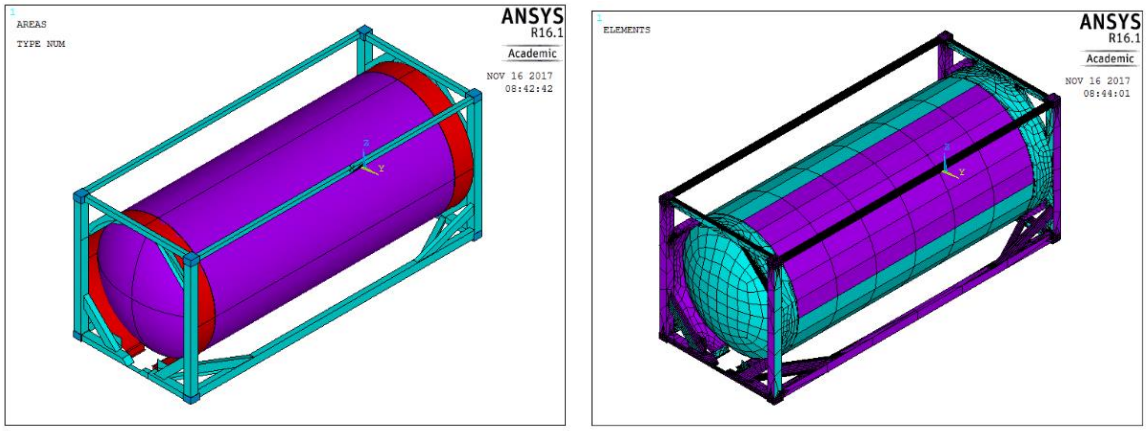

Figure 5- 10 Global model (unmeshed vs meshed)

5.2.2 The local model

5.2.2.1 Choice of elements

When modelling a local model, both shell elements and solid elements can be used. However, there are some restrictions and rules on modelling with different elements.

When shell elements are used, the elements have to be arranged in the mid-plane of the structural components, particularly in the case of steep stress gradients. Welds can be included by vertical or inclined plate elements having appropriate stiffness or by introducing constraint equations or rigid links to couple node displacements. In simplified models, welds can be ignored.

Solid elements are recommended for complex cases. A 20-node elements with mid-side nodes at the edges, can be used. With prismatic solid elements, weld can be modelling easily. By the adoption of reduced integration, the stresses can be directly extrapolated from the integration points to the element surface and subsequently to the weld toe.

Figure 5-11 shows typical modelling with both elements.

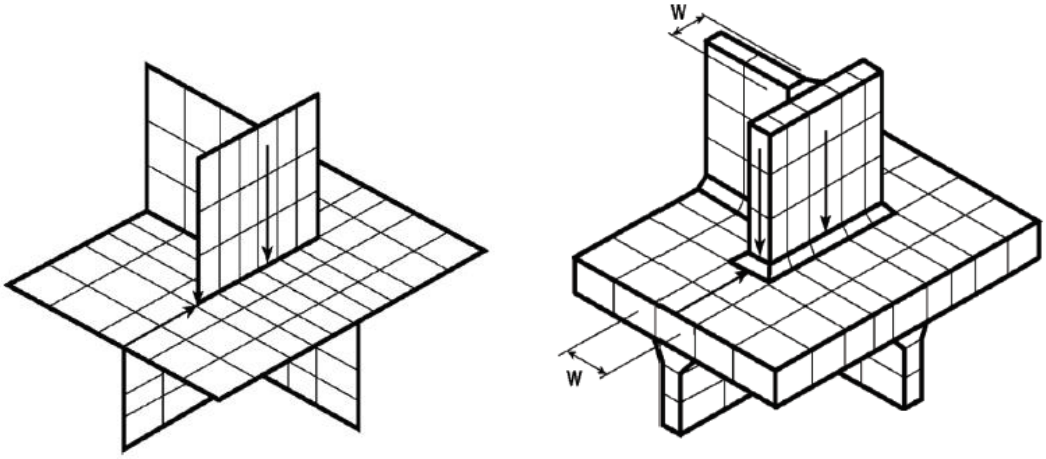

Figure 5- 11 A typical mesh and stress evaluation paths for a weld detail (shell element and solid element) (Hobbacher, 2008)

In this thesis project, the local model is based on the connection between the skirt and the frame. The curvature of the plates adds up to the complexity of the model, thus solid 185 element is applied to establish this model. In addition to the structure itself, a layer of element is added to simulate the weld joint. As it is suggested by the company, the welding element has same material property (Elastic modulus) as the frame. The local model is built under the same coordinate system as in the global model. The unmeshed and meshed local model is shown in figure 5-9.

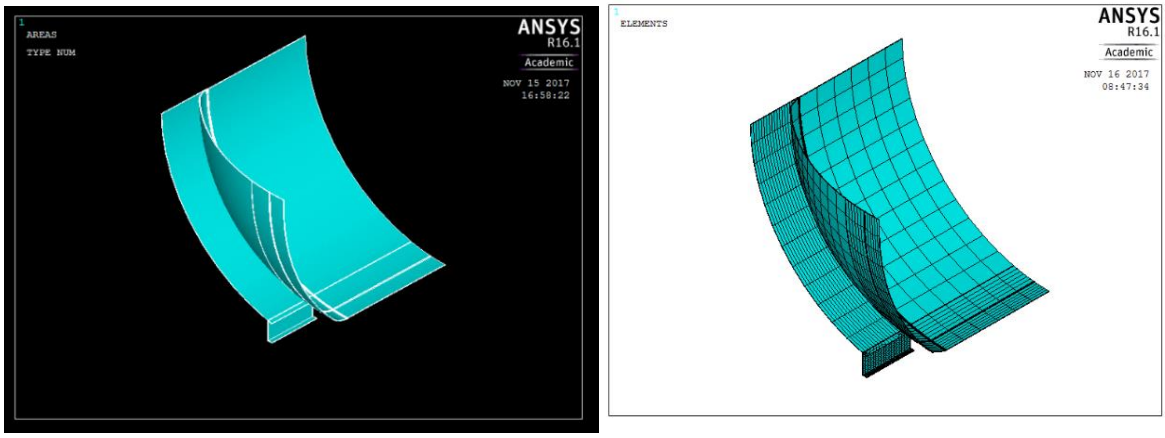

Figure 5- 12 Illustration of the local model (unmeshed and meshed)

5.2.2.2 Mesh of local model

As for the mesh of the local model, previous researchers have put forward different rules. DNV recommends that a 20-node solid element with a size of t/2 x t/2 or 8-node shell elements with a size of t x t to be used. For this mesh, linear extrapolation of the component stresses from two points (t/2 and 3t/2) are recommended and the principal stresses are suggested to be calculated at the hot spot. (Det Norske Veritas(DNV), 2008)

Fricke and Petershagan and Paetzold recommend the use of 20-node solid elements that have a side length of the plate thickness at the hot spot. They also recommend at least three elements of equal length in the area where the stress increases. (Fricke, Petershagen, & Paetzold, 1998)

ABS recommends that 20-node solid elements or 8 node shell elements be used with a size of t x t. (American Bureau of Shipping (ABS), 1992)

Based on the abovementioned suggestions, the mesh of the local model, catering for future calculation, is decided. The type of weld joint here is a lap joint. The hot spot is a fatigue mode-I type-A hot spot, thus primary stress is used as hot spot stress. To calculate the primary stress, the quadratic extrapolation formula is applied. In the quadratic extrapolation formula, three nodes along the fatigue path, each being approximately positioned at 0.4t, 1.0t and 1.4t away from the weld toe, are selected, where t is the wall thickness of the tubular component whose stress distribution is extrapolated.

For this purpose, the mesh of the local model, especially in the weld joint area, should be as precise as possible. In the area away from the weld toe, mesh can be relatively coarse to reduce computation time. Thus each line is divided into a certain number and sweep mesh is applied. In the area of hotspot stress calculation, in order to make sure the nodes are at the right location, the general idea of meshing is that firstly the model is divided along two lines. The first line is t mm away from the weld toe, while the other one is 1.4t mm away from the weld toe. The area between the weld toe and the first line is divided by 10 while the area between the two lines are divided by 2. In this way we can guarantee the nodes are at the desired locations. Considering how the model is established, in reality the meshing is slightly different, but still can ensure that the nodes are at the right location. Figure 5-10 shows the meshed weld area in the local model.

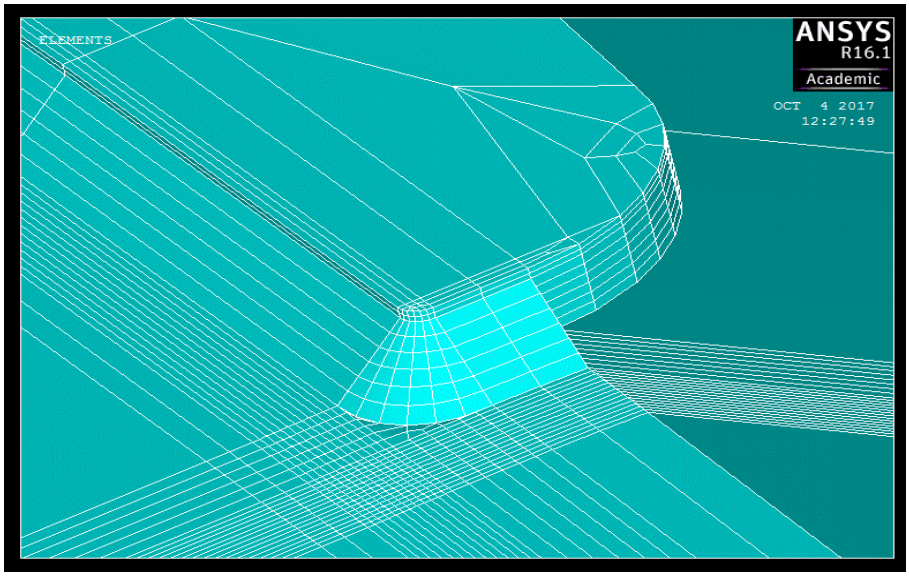

Figure 5- 13 Mesh of the local model (Hotspot stress calculation area)

5.2.3 Transition from the global model to local model

In ANSYS, normally the transition from a global model to a local model is done by the sub-modeling technique. When it is applied on the user defined cut boundary, displacements of nodes from global model are interpolated automatically to calculate displacements for nodes on the local model, which will be used as boundary conditions in the local model. This technique is based on Saint Venant's Principle. The requirements of this technique are as follow, firstly, since this technique is based on Saint Venant's principle, the cut boundary should be away from stress concentration area. Secondly, both global model and local model should be established under the same coordinate system. Thirdly, only shell element and solid element should be used in both models.

An initial attempt of the transition is done by this sub-modeling technique. However, due to a lack of knowledge and the complexity in transient analysis, it failed as the number of boundary conditions for the local model is not sufficient. After consulting with the experts, a new method to combine the two models is proposed.

In this new method, firstly, establish both models under the same coordinate system. Secondly, extract coordinates for each node in global model and local model with its node number, and save the information in two txt files defined as 'global node' and 'local node'. Thirdly, a MATLAB file is used to select the nodes that have same coordinates in both models and save the node numbers in a matrix. This MATLAB file also writes macros for ANSYS. The macros written by this MATLAB file will extract displacements for the selected nodes in the global model and apply them to the respective nodes in the local model. In the end, together with the acceleration input, the calculation could be performed on the local model.

An example is shown in Table 5-1. In this case, node 10438 in the global model is paired up with node 1 in the local model. The x,y,z displacement of node 10438 in the global model are extracted and used as boundary conditions for each time step on node number 1 in the local model.

	Node number	x	y	z
Global node	10438	5442.5	1039.5	-3.0699
Local node	1	5441.1	1038.5	-3.5951

Table 5- 1 Example of the node pairs

Although this method can solve the problem, it has a few drawbacks. To begin with, the calculation on the local model is highly dependent on the boundary conditions, which means whether the calculation would succeed depends on the meshing of both models. If the number of 'node pair' is insufficient, the calculation will fail as it doesn't converge. Secondly, this method is most likely to fail in a shell to shell transition, because the number of boundary conditions required for each node is higher than that is required for shell element. Thirdly, in transient dynamic analysis, the reliability of the method is yet to prove due to the non-linear nature of this analysis type. In different calculations, the method should be modified to reach a converged result.

5.2.4 Comparison between the global model and local model

To verify that the local model can represent the part in global model correctly, a comparison study is carried out.

One node from global model and another from local model is extracted. These two nodes have similar coordinates but are not included in the abovementioned 'node pairs', since the nodes from the 'node pairs' will surely have same displacements. The aim of this comparison study is to compare the displacements of nodes outside the node pairs, thus proving the feasibility of this method.

Three groups of nodes are chosen. The node number and coordinates are shown in table 5-2. The comparison result is shown in figure 5-14, figure 5-15 and figure 5-16

Group1	Node number	X coordinates	Y coordinates	Z coordinates
Global node	10438	5442.5	1039.5	-3.0699
Local node	7	5440.7	1038.5	-3.7679
Group2	Node number	X coordinates	Y coordinates	Z coordinates
Global node	10464	5437.4	1146.4	-9.431
Local node	3002	5439.1	1144.9	-9.4396
Group3	Node number	X coordinates	Y coordinates	Z coordinates
Global node	11338	5442.5	879.55	24.894
Local node	5306	5441.3	877.55	24.894

Table 5- 2 Detail information of the node pairs

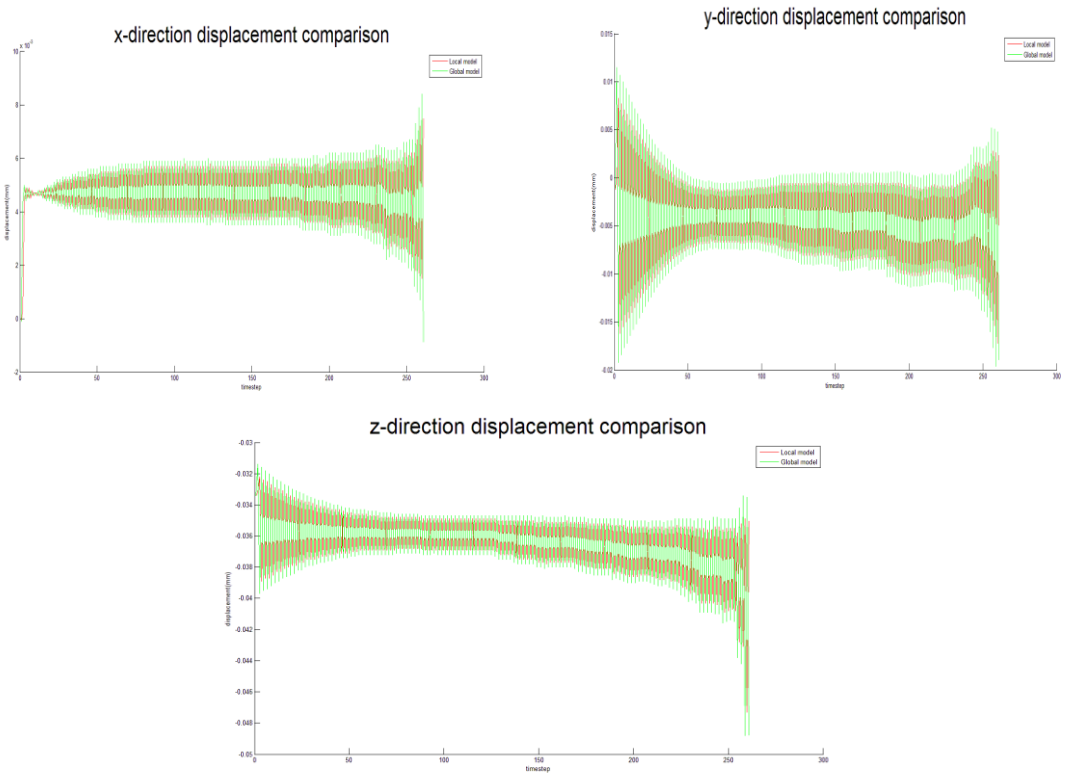

Figure 5- 14 Comparison of nodal displacement from both model (group1, x, y, z translational displacements)

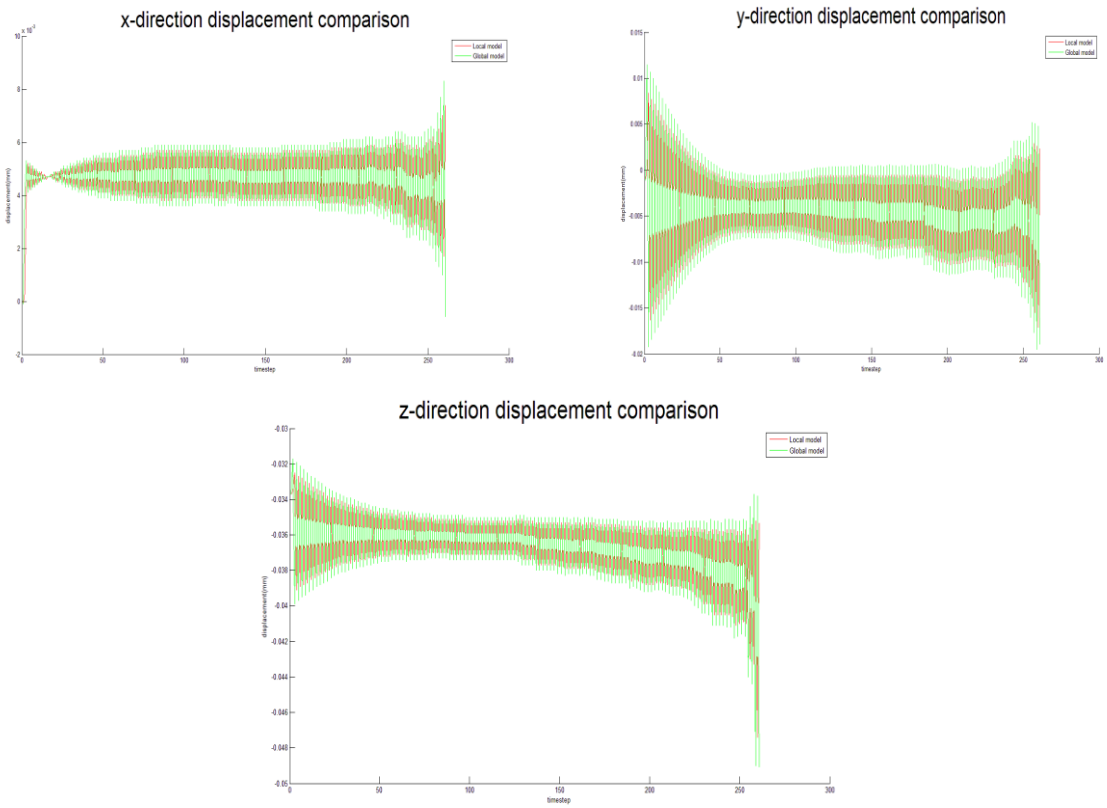

Figure 5- 15 Comparison of nodal displacement from both model (group2, x, y, z translational displacements)

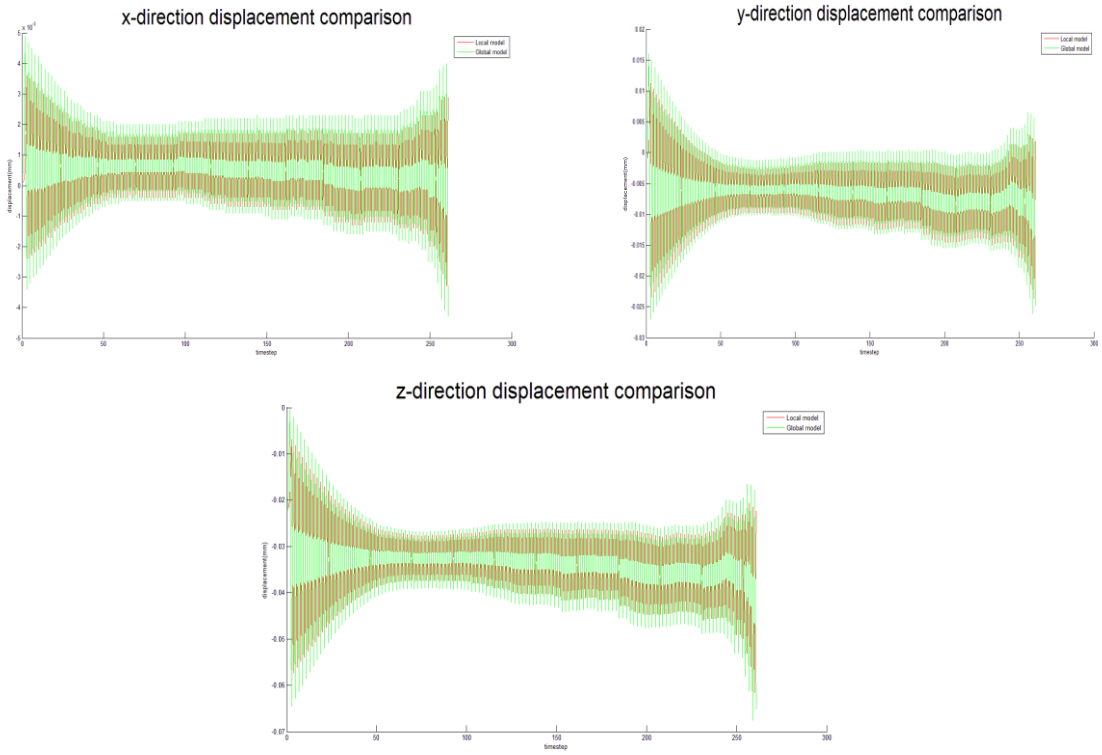

Figure 5- 16 Comparison of nodal displacement from both model (group3, x, y, z translational displacements)

Note the global model is built with shell elements only and the local model is built with solid elements only. In ANSYS, there is no rotational displacement for solid element. However, when the translational displacement of the node is same, the force and moment around it should both achieve the equilibrium. Thus a comparison between the translational displacements is sufficient. From the comparison we find that for most of the time steps, the difference between these two nodes is not too much. Although for some time steps the difference is quite large, however, given the slight difference between the nodes in each group and the curvature of the model, the result is acceptable. Thus the local model can truthfully reflect the global result and is used to carry out fatigue calculation.

5.3 Data processing

5.3.1 Variable amplitude hot spot stress

The hot spot stress is the geometric stress on the surface at the critical point (hot spot), such as discontinuity and weld toe, where fatigue crack is expected to grow along the weld toe in the local model. Hot spots are chosen at places where geometry change causes peak stresses. The hot spot positions and paths of stress extrapolation is illustrated in figure 5-17

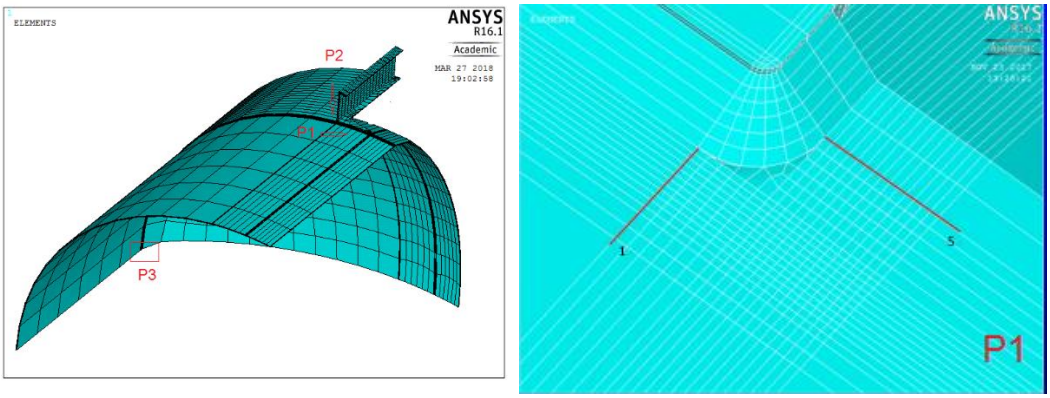

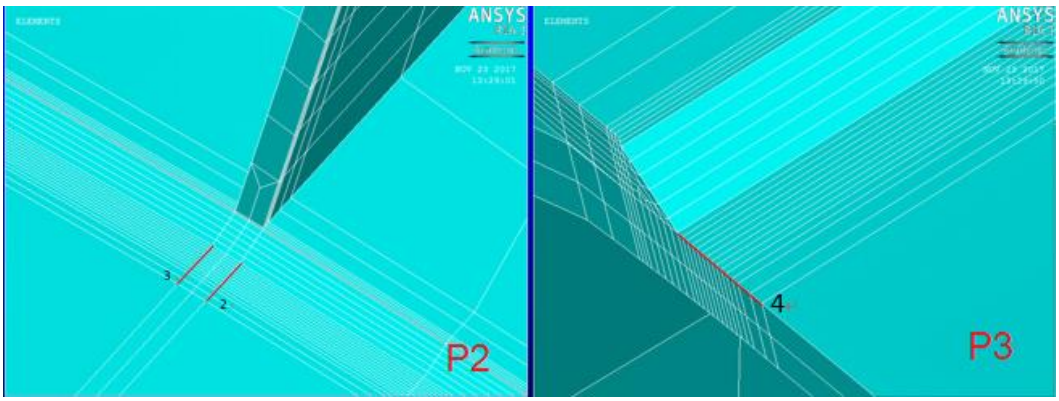

Figure 5- 17 Illustration of hot spots and paths

Hot spot stress cannot be read from FE model at weld toe node, but should be calculated by the extrapolation method. The IIW recommends that for calculation of hot spot stress, the quadruple extrapolation method is preferred. In this method, three nodes at specified locations are selected. They are at 0.4t, 1.0t and 1.4t away from weld toe, where t is the plate thickness. The calculation is illustrated in figure 5-18

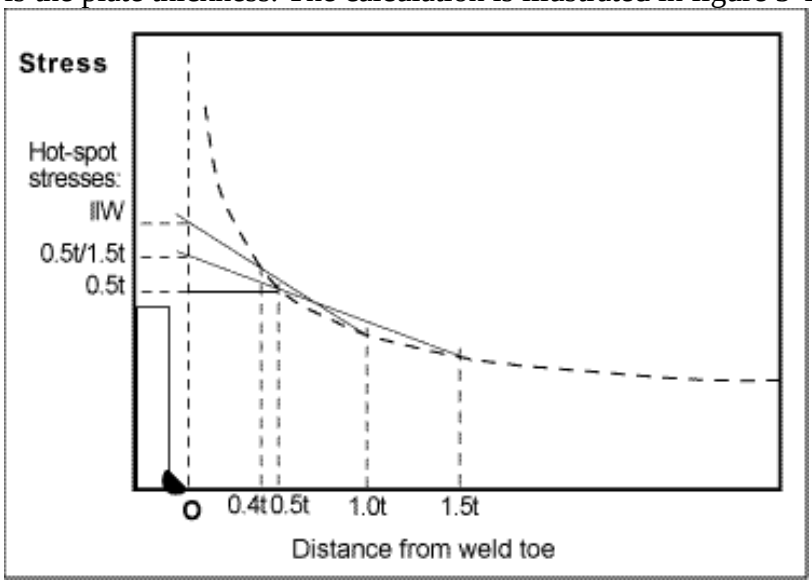

Figure 5- 18 Illustration of quadruple extrapolation (Hobbacher, 2008)

A polynomial curve is applied to fit those stress. Thus we have

$$\sigma_{0.4t} = a \cdot (0.4t)^2 + b \cdot (0.4t) + c$$
$$\sigma_{1.0t} = a \cdot (1.0t)^2 + b \cdot (1.0t) + c$$
$$\sigma_{1.4t} = a \cdot (1.4t)^2 + b \cdot (1.4t) + c$$

By extrapolating the stress at these three nodes, we can obtain that.

$$\sigma_{Hs} = \sigma_{0t} = \frac{7}{3}(\sigma_{0.4t} - \sigma_{1.0t}) + \sigma_{1.4t}$$

5.3.2 Choice of solution

A node is connected to a number of elements. Thus there are two ways to extract stress on each node. The first one is to extract stress on each element attached to one node and take the mean value as the nodal stress. The second one is to extract the nodal averaged stress calculated automatically by the software. An example is shown is figure 5-19 to display the difference between these two components. In this example, the location of the nodes are at 0.4t, 1.0t and 1.4t away from weld toe on fatigue line 1.

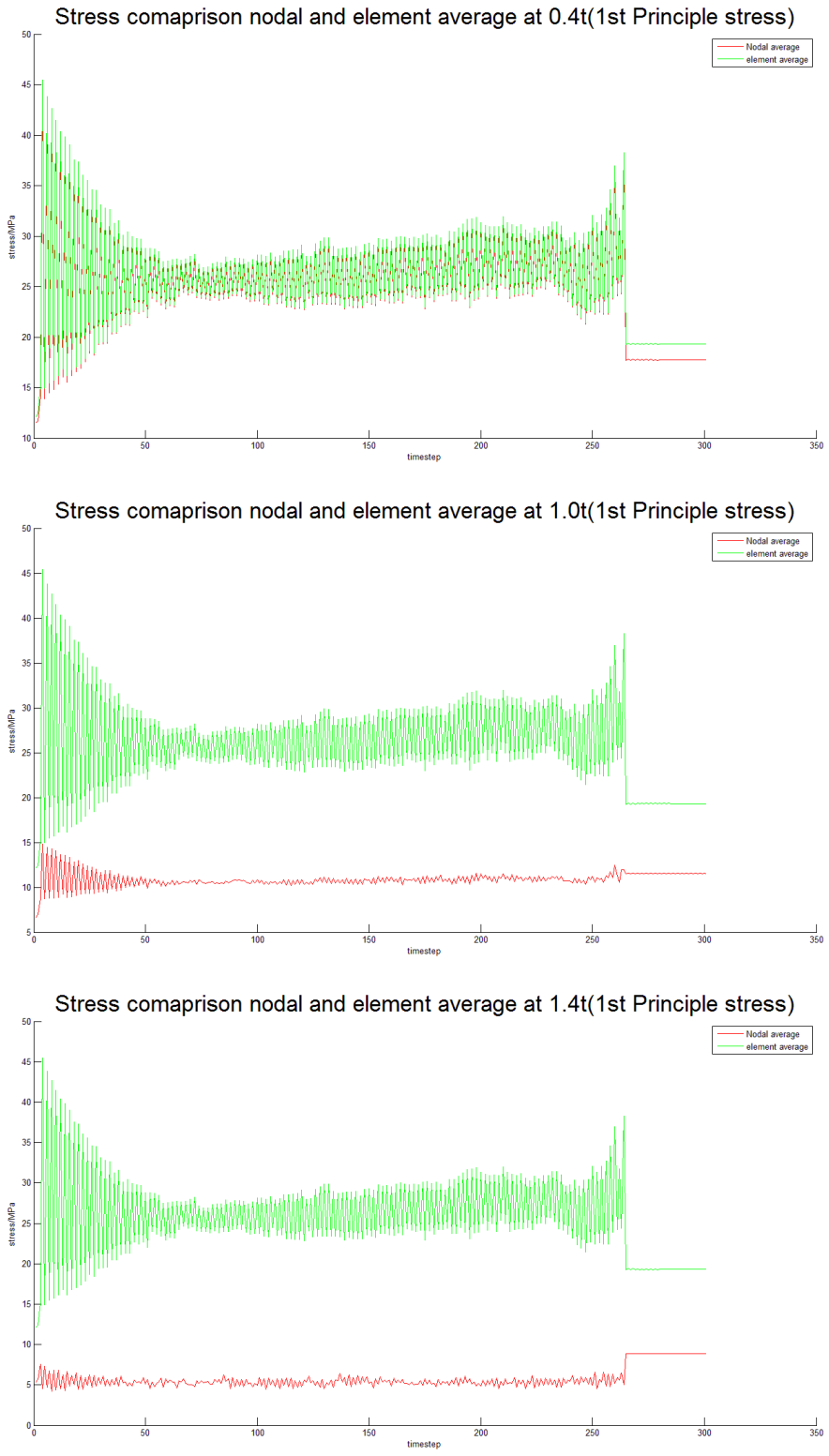

Figure 5- 19 Comparison of Nodal averaged result and Element averaged result on three nodes (1st Principle stress)

From the figures we find that for hot spot 1, at 0.4t, the difference is not much. However, for other nodes, the difference can be quite large. Because of the numerical description of element formulation, it is advised to use the nodal average instead of the element average.

5.3.3 Choice of stress

Once the choice of element solution is determined, the choice of stress component as the hot spot stress becomes another issue. There has been some arguments on which stress component should be used as the hot spot stress. From engineering point of view, the maximum principle stress is suggested because it's easy to obtain. However, some researchers suggest using the primary stress because from experimental observations, the developed crack is normal to the primary stress whereas the direction of the maximum principal stress may be different (Karamanosa, Romeijn, & Wardenier, 2002). For this sake, primary stress at the specified locations are used as the hot spot stress.

To extract the primary stress, firstly, a local coordinate system is established at the weld toe. Then a nodal coordinate systems is built by rotating it to the direction of specified node. In the end, primary stress can be read as the stress along the axis that follows the specified direction. An example of the primary stress is shown in figure 5-20

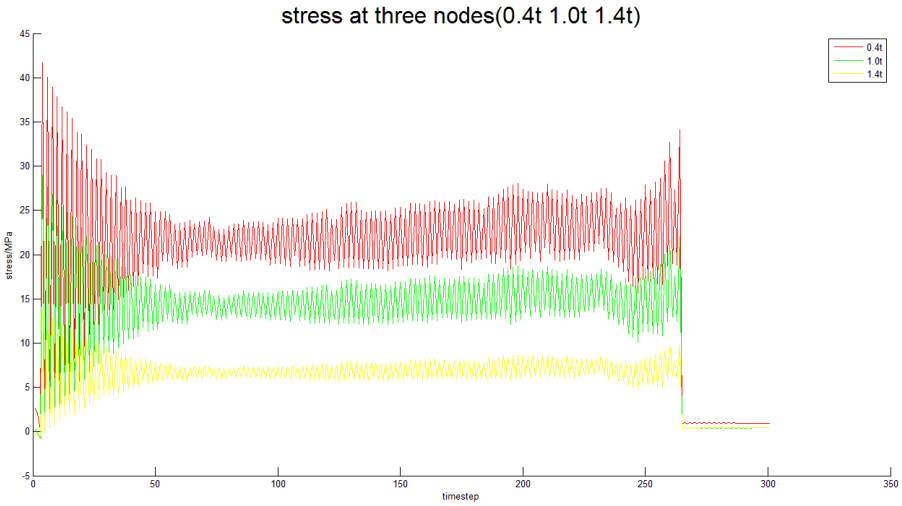

Figure 5- 20 Illustration of primary stress at three nodes (line 1)

A comparison of principle stress and primary stress is displayed in figure 5-21

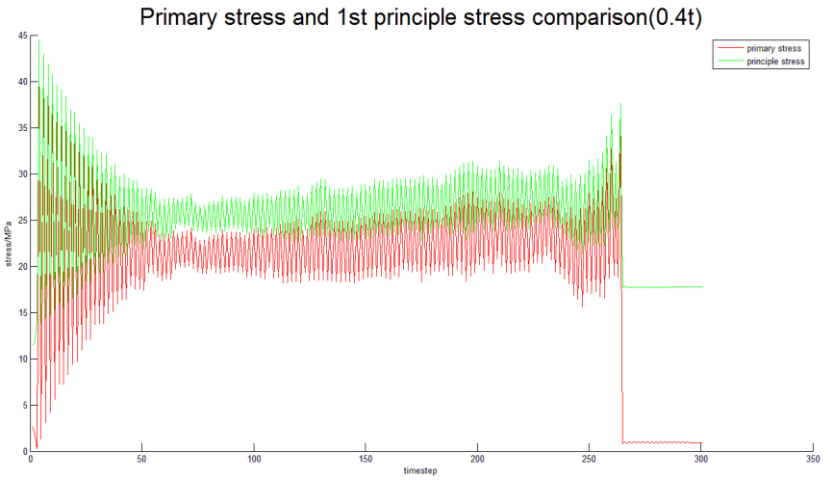

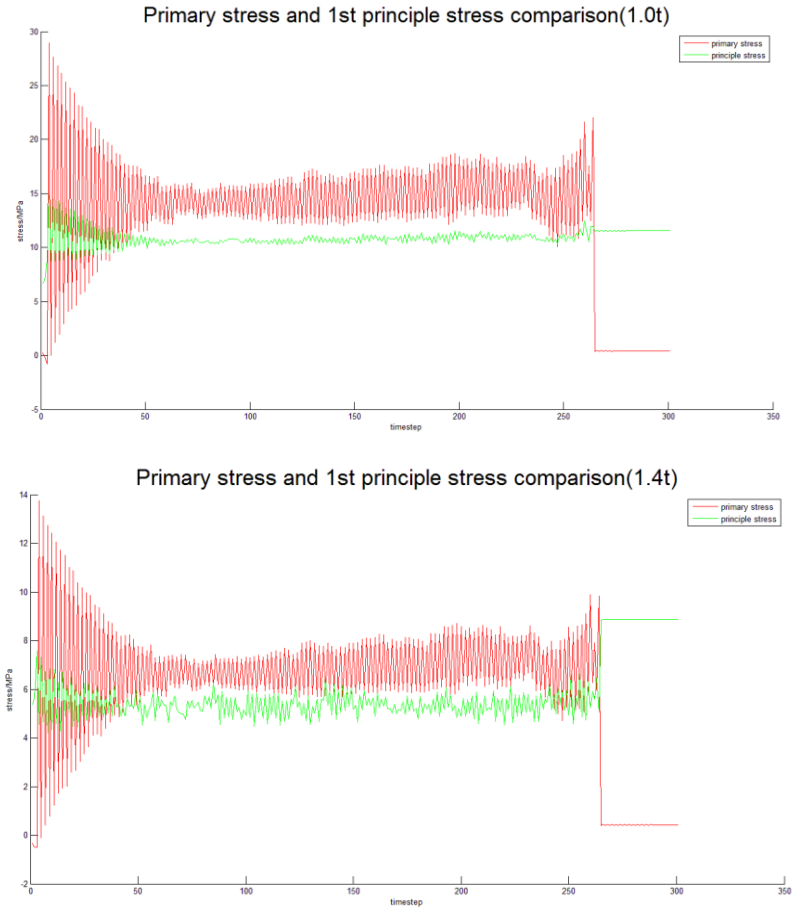

Figure 5- 21 Comparison of primary stress and principle stress (0.4t, 1.0t, 1.4t along line 1)

From the comparison we find that firstly, there is a huge difference between these two stresses. This is because principle stresses are the components of stress tensor when the shear stress becomes zero, while the primary stress is the stress along the specified direction. Their directions may not coincide and in primary stress direction, there is shear stress components. Secondly, on nodes that are farther from the weld toe, the difference is larger due to stronger influence from shear stress. In the end, the primary stress is used as the hot spot stress.

With the primary stress at three nodes based on nodal averages, the variable amplitude hotspot stress is obtained. After rain-flow counting, the constant amplitude hotspot stress is calculated from the VA hotspot stress. These two stresses are shown in figure 5-22

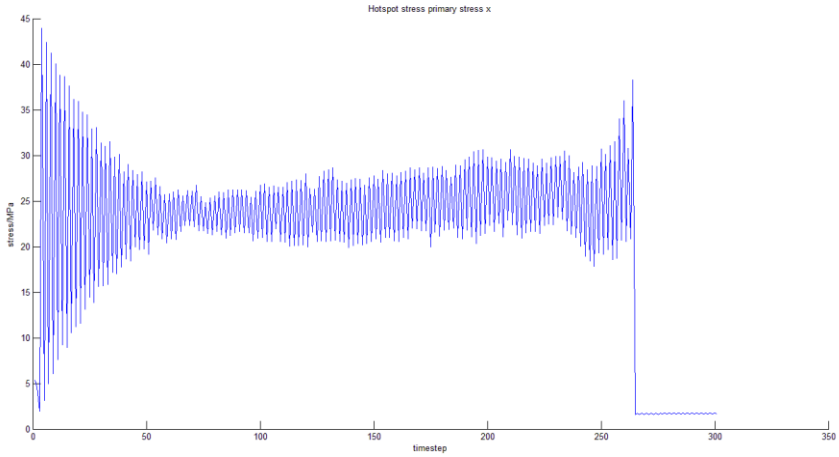

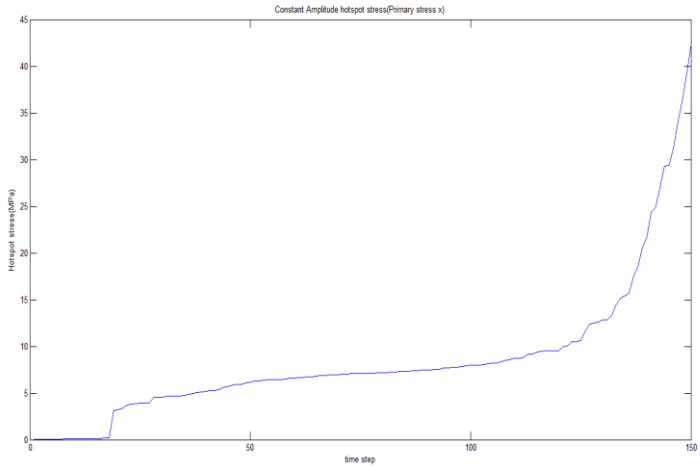

Figure 5- 22 VA hotspot stress vs CA hotspot stress (line 1)

5.3.4 Transition from 5 minutes to a longer period

The abovementioned stress is calculated for the 5-min input. To calculate for a much longer time period, for example, 20 years, a transition from 5 minutes to 20 years is required. Due to the randomness of the input, a simple multiplication of the result would be incorrect. For example, in a longer period, the peak acceleration might be higher and the input will include more value, which might lead to a higher hot spot stress level. However, the distribution of the output for 20 years should have a high similarity with that for 5 minutes. Hence through the distribution of hot spot stress, we can obtain the probability of occurrence for a high or lower stress range, thus including all possible stress levels that would occur during the 20 years.

To estimate the distribution of hot spot stress, three distribution types, namely the Weibull distribution, Rayleigh distribution and Generalized Extreme Value (GEV) distribution, are selected to find out the best fit.

Firstly, the stress range is divided into a few blocks and the probability histogram is plotted. Then the data is fitted to different distribution types and the probability distribution functions (PDF) are plotted. Alternatively, to help to reach a conclusion, the cumulative distribution functions (CDF) of the three distributions are also plotted together with an empirical CDF derived from the data. The result is shown below.

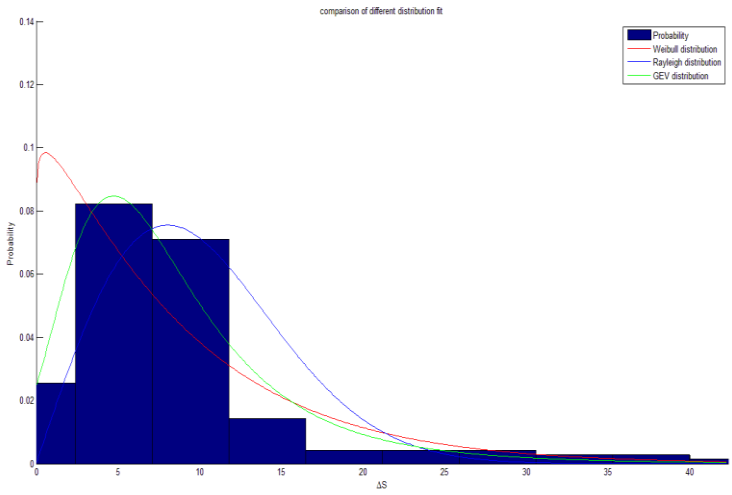

Figure 5- 23 Probability histogram and three PDFs

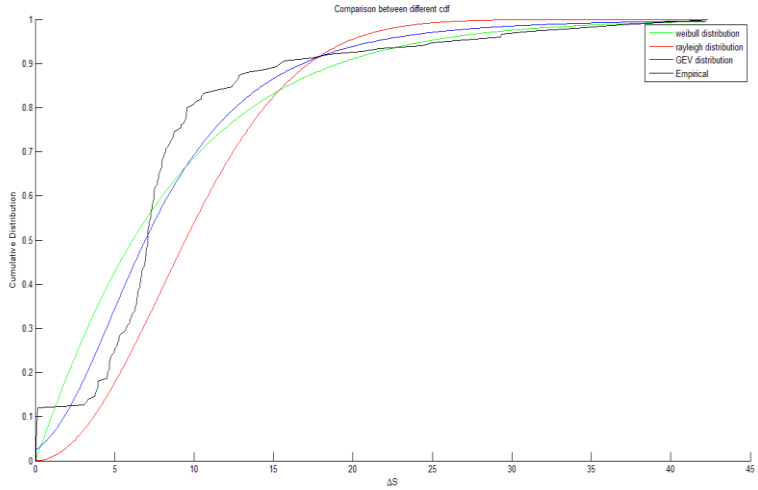

Figure 5- 24 Empirical CDF and three CDFs

The Generalized Extreme Value distribution combines Gumbel, Frechet and Weibull family of Distributions. In fatigue line 1, the shape parameter for the fitted GEV distribution is positive, which is reduced to a Frechet distribution.

From figure 5-23 we find that GEV distribution and Rayleigh distribution are better fits than the Weibull distribution because the values on the curves are closer to that of the histogram data and they show a similar tendency. Weibull distribution gives a higher estimation on low and higher range stress, which might exaggerate the situation. In low and middle stress range, the GEV distribution gives a better fit than the Rayleigh distribution. In high stress range, the probability calculated with Rayleigh distribution is lower than that of GEV distribution. Hence Rayleigh distribution gives that the high stress range is less likely to occur, and the damage induced by this part is lower. As a result, fatigue damage calculated with it will be more conservative.

From figure 5-24 we find that the CDF given by the GEV distribution is closer to the empirical CDF. Thus the GEV distribution is recommended. Results calculated with other two distribution types will be presented and compared.

5.3.5 Random process of the output

In order to remove the randomness of the 5-minute output, a random stress signal, which corresponds to an output of 50 minutes, is constructed out of the 5-minute out. This signal is created by randomly select stress levels from the 5-minute output with respective probability of occurrence. Then the new signal is fitted to a new distribution with abovementioned method and calculated for a period of 20 years.

Alternatively, the 20-year output can be formed by selecting result from the 5-minute output directly. Since the distribution of hotspot stress only includes values within the 5-minute hotspot stress range (lower than 50MPa), compared with this realization of the output, the stress level given by the first realization will be centralized in lower levels, and the probability of high stress level will be lower. The result is shown in figure 5-25

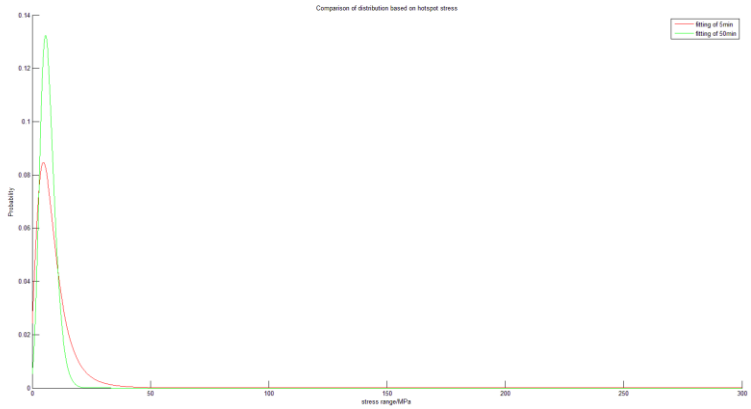

Figure 5- 25 Comparison of the random process

5.3.6 Choice of the S-N curve

When hotspot stress concept is applied and the weld root is non load carrying, the S-N curve is FAT 100. The figure is shown below

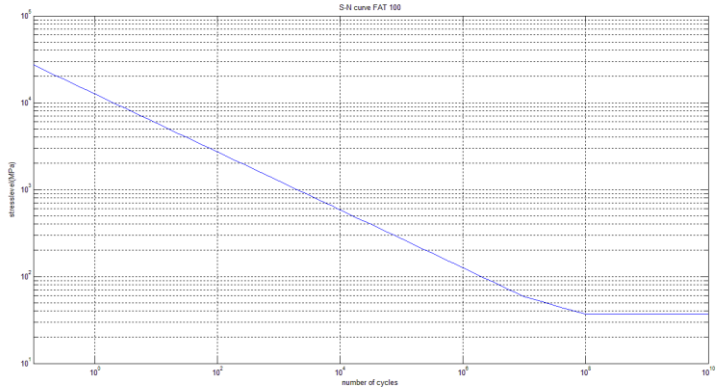

Figure 5- 26 S-N curve FAT 100

This S-N curve shows that when stress is below 36.91MPa (cut-off limit), there won't be any fatigue damage. From 5-26 we know, there is a small number of cycles with stress level above the cut-off limit, thus we expect there would be limited fatigue damage.

5.4 Analysis result

For fatigue line 1, damage factor is calculated under two distribution types. For each type, it is calculated under both direct fitting and random process. Direct fitting is to calculate damage factor with these distribution types directly. Random process is to assemble a stress history of longer period (30min), then damage factor is calculated with the 30min signal with the same distribution type. The comparison result is listed in table 5-3

	Rayleigh distribution	GEV distribution
Direct fitting	1.4309e-5	0.0145
Random process fitting	0	0

Table 5- 3 list of result

The same procedure is applied on the other 4 fatigue paths. Detailed result will be listed in later chapters. From table 5-3, since the maximum damage factor is lower than 1, we can draw the conclusion that there is no fatigue damage at hot spot 1 within 20 years.

Chapter 6 Other FEM analysis Other Than Fatigue Calculation

In this chapter, works apart from fatigue calculation for specified welding are listed. These works are requested by Trifleet Leasing during the period of my thesis. In these works, both the 26kl model global model established by the previous student and the all shell model are applied. Recommendations for improvement of my work will be listed at the end of this chapter.

6.1 Fatigue life estimation under combined utility

In the previous project, the previous student performed fatigue life calculation of the 26kl tank container under highway transportation. Fatigue life is calculated for a few hotspots along designated paths. In this graduation thesis, fatigue life is calculated for a few other hotspots under railway transportation. However, a few questions still remain unanswered. What would be the fatigue life of this tank container under a combination of both transportation methods? How would fatigue life changes if the utility (transportation type, transportation time) of the container changes?

From chapter 5 and graduation thesis of previous student we know, the finished calculation only contains results for a limited number of hotspots and the input for both transportations only represent a small portion of all scenarios. Considering the unlimited input combinations and large amount of hotspots, it is advised to narrow the scope and propose a formula instead of calculating the exact fatigue life for every possible hot spots. The verification and modification of the formula should be done in future when more data are obtained.

The decision of fatigue life of the tank container consists of three steps. Firstly, define related parameters. Secondly, propose formula of fatigue life. Thirdly, clarify damage criteria and assumptions of the formula. From previous chapter we know, for a specified hotspot, fatigue damage is related to both working condition (accelerations) and working time. On the one hand, as the working condition gets severer, which is represented by a higher acceleration amplitude or acceleration range, the fatigue damage gets higher and fatigue life decreases. On the other hand, the longer the tank container is in use, the greater damage it will suffer from, consequently the shorter fatigue life. Let's assume that the route of transportation is fixed, therefore the fluctuation of acceleration range and amplitude shouldn't be significant. Such minute changes are already accounted for in the random process part of the calculation. Therefore the deviation of fatigue life of each hotspot induced by input variation can be ignored and fatigue damage is only related to working time.

Let's define standard work plan as 8 hours per day, 250 days per year and 20 years. Let h1, d1, y1 be the working parameters for tank container under highway transportation and h2, d2, y2 be their counterparts under railway transportation. Fh_1, Fh_2, …,Fh_n denote the calculated fatigue life for hot spot 1, 2, …,n under highway transportation according to standard work plan while Fr_1,Fr_2, …Fr_n be the same thing under railway transportation. Then the fatigue life of this tank container under random combined working conditions is

$$T = \frac{20}{Max\left\{\frac{y_1 d_1 h_1 Fh_1}{40000} + \frac{y_2 d_2 h_2 Fr_1}{40000}, \frac{y_1 d_1 h_1 Fh_2}{40000} + \frac{y_2 d_2 h_2 Fr_2}{40000}, \dots, \frac{y_1 d_1 h_1 Fh_n}{40000} + \frac{y_2 d_2 h_2 Fr_n}{40000}\right\}};$$

The unit of fatigue life is years.

The equation above is based on several assumptions. To begin with, all cracks are equally dangerous to the structure regardless of their locations. That is to say, if any crack is found, the tank container is considered as out of use. Thus when fatigue damage for whichever hotspot reaches one, the tank container reaches the end of its life. In reality, the container might still be able to perform even if cracks are found at some less critical locations. To account for this, weight factors can be implemented for each term. Secondly, the equation assumes that fatigue damage accumulates linearly over time. For each hotspot, total fatigue damage is a summation of fatigue damage induced by both transportation. For each transportation, fatigue damage is the

ratio between actual working time and standard working plan multiplied by fatigue damage of standard work plan. In other words, fatigue life for each transportation is linearly related to its actual working plan. However, from chapter 2 we know, fatigue development is not linear over time. Fatigue behavior at various hotspots are different due to pre-process of the structure and local material properties. Therefore, this equation can be considered as a reference of the fatigue life of the tank container, rather than a precise calculation of it.

6.2 A simple static calculation.

At the beginning of this thesis project, Trifleet Leasing is interested in a calculation concerning the falling of the container.

In this case, a container is considered to be falling from 2 meters. To simplify calculation, the loading is considered to be static and dynamic behavior of falling is ignored. Assuming the time of contact is 1s, total loaded force on the bottom is 578.2KN. On each bottom the force is 144.5KN. The result is shown in figure 6-1

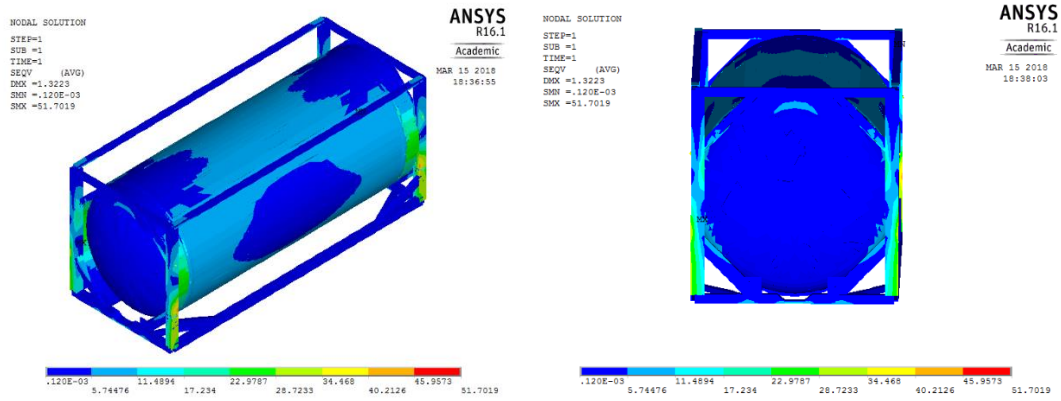

Figure 6- 1 Von Mises stress of static loading calculation

From figure 6-1 we find, maximum Von Mises stress occur at the location where vertical frames are connected to skirts. The maximum Von Mises stress is about 51MPa, which is much lower than yielding stress.

6.3 The quick calculation

From chapter 5 we know, fatigue damage can be calculated with respect to hotspots. Therefore primary stress along each specified paths must be obtained and the extrapolation method must be applied to calculate hotspot stress. To obtain correct result, a local model at the location of interest must be established. However, such a procedure can be much too time-consuming and can only calculate fatigue damage along limited paths at one time. Trifleet Leasing B.V is interested in a simpler way that can illustrate damage factor of each node on the global model directly. In other words, a way to calculate the damage factor at each node without establishing local models and plot it automatically. Therefore the quick calculation is presented to reach this goal.

In general, the quick calculation follows the procedures of fatigue calculation, but the calculation on local models are ignored. After the calculation on the global model, Von Mises stress at each node is extracted and used for data processing. The rain-flow counting method is applied to obtain constant amplitude stress,

which is used to calculate fatigue damage factor on each node. The full procedure is shown in figure 6-2

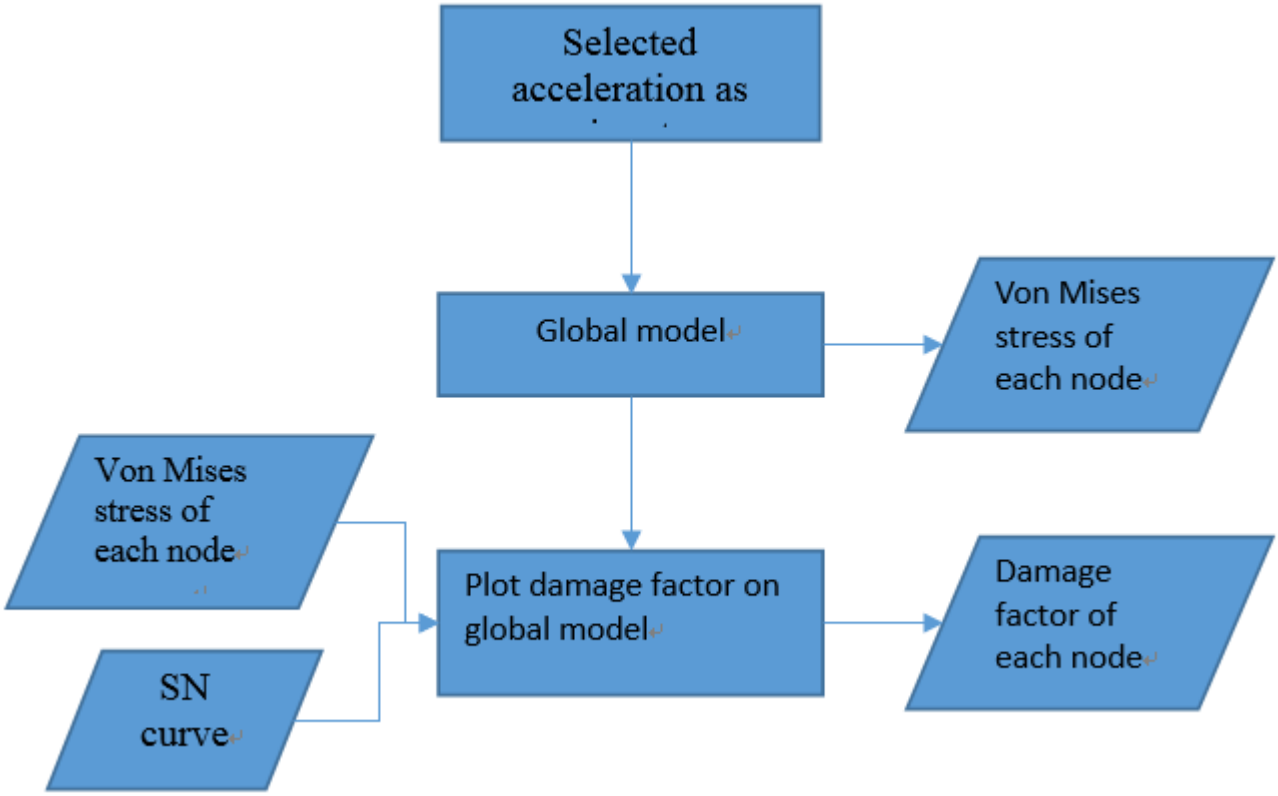

Figure 6- 2 Quick calculation flow chart

In comparison with the full calculation procedure, this quick calculation has a few drawbacks and the quick calculation result is inaccurate in some ways.

To begin with, the calculation result doesn't reflect the situation with local welds because local welding information is not included in the model. As the geometry changes, displacement and stress on each node changes too. Therefore, without welds, stresses at nodes on the global model can be different from their counterparts on the local model due to a change of geometry.

Secondly, the calculation result doesn't reflect the potential crack opening direction at each node. In FEM calculation, Von Mises stress doesn't specify the direction. It only shows the stress level, i.e. the magnitude. Thus Von Mises stress is always positive. Supposing that in a calculation, Von Mises stress is above the cut-off limit all the time and Von Mises stress direction and crack opening direction is same at the first step then opposite to each other in the second step, the calculation will take it as fatigue damage is induced at both steps. In other words, it couldn't recognize if the stress is contributing to the opening of the crack or against it.

Thirdly, substituting hotspot stress with Von Mises stress is inaccurate. In reality, at hotspots, the hotspot stress doesn't equal to the structural stress. In fact, the hotspot stress should be calculated through extrapolation method. Ignoring the extrapolation procedure would lead to an overestimation or underestimation of the stress, depending on the location of hotspot.

Last but not least, this quick calculation process can only calculate fatigue damage factor with respect to one SN curve. In this quick calculation, fatigue damage factor is plotted against node numbers. For nodes at different location of the model, due to the change of material or structure dimensions, different S-N curves should be used. However, since the node numbers in FEM model is arbitrary, the calculation program cannot tell which S-N curve should be used purely based on node numbers. Although this problem can be solved by

adding extra information to the calculation program, however, when the model is meshed differently, the location of each node will change. As a conclusion, it is difficult to store any locational information in node numbers, therefore calculation with multiple S-N curves is impossible.

In spite of so many drawbacks, a few quick calculations are performed to check the result and feasibility. The first calculation is conducted on the 26kl model developed by the previous student. In this model, the tank is modelled with shell element and frames are modelled with beam element. The input is extracted from samples provided by the Chinese manufacture mentioned in chapter 5. The x, y z accelerations are shown in figure 6-3

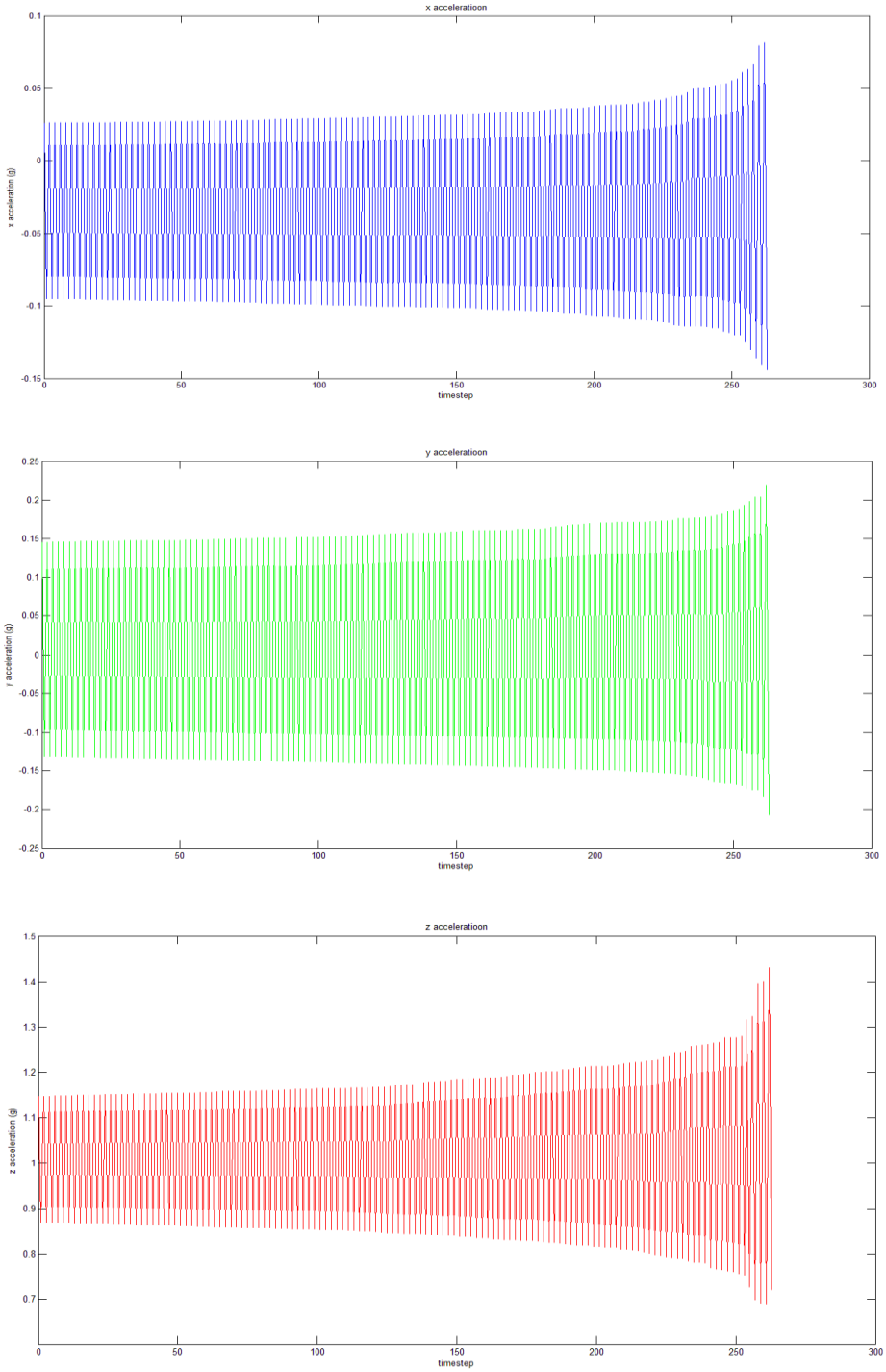

Figure 6- 3 Accelerations data from experiment

The input contains 300 timesteps corresponding to a 5-minute input. The samples are selected as such in order to guarantee the maximum acceleration range at each time step. The calculation result is shown in figure 6-4 and figure 6-5

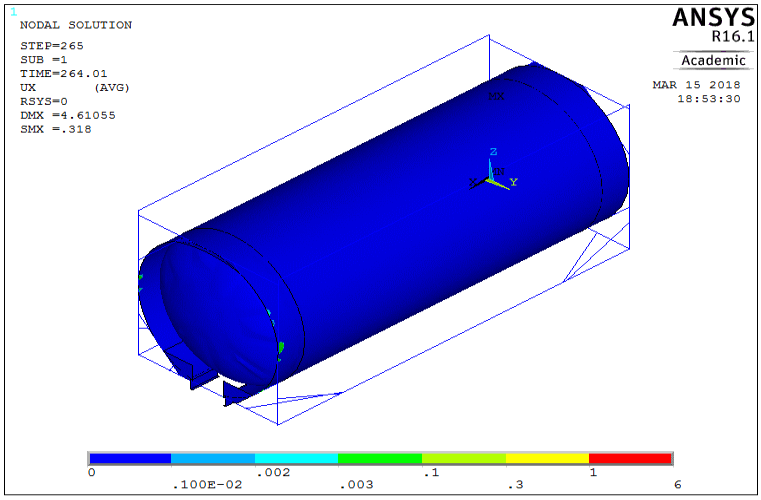

Figure 6- 4 Damage factor plot on model

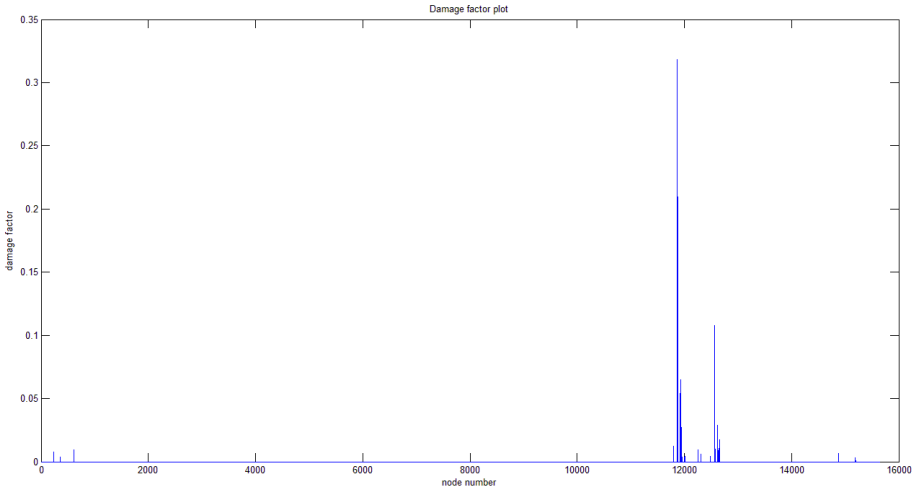

Figure 6- 5 Damage factor plot vs node number

Figure 6-4 shows that the most damaged area is the area that connects skirts and frames. However, that is not the case because Von Mises stress is different from hot spot stress, which verifies the drawback of quick calculation. The maximum damage factor is 0.3, which is much lower than 1, meaning no fatigue damage is done under this input. Figure 6-5 shows that for a lot of nodes, fatigue damage is 0. This can be explained from two perspectives. On the one hand, the fatigue damage could be 0. On the other hand, the element that are attached to those nodes are beam element, and nodal averaged Von Mises stress cannot be extracted.

In the second calculation, the same model is used while the inputs are slightly different. The x, y acceleration remains unchanged while the amplitude of z acceleration is doubled. Details of the process of the input is demonstrated in chapter 5. Since x and y acceleration remain unchanged, figure 6-6 shows the comparison between two z acceleration inputs.

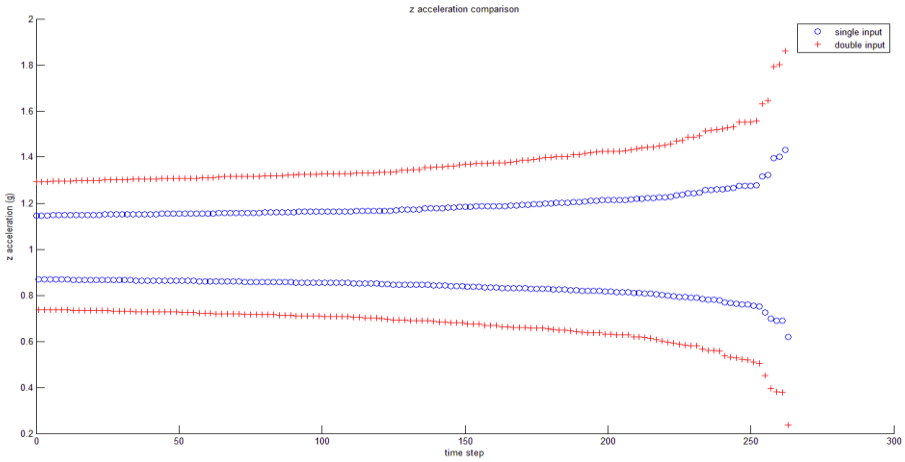

Figure 6- 6 Comparison between accelerations

The calculation result is shown in figure 6-7 and 6-8. A comparison of damage factor of these two calculations are presented in figure 6-9. With doubled input, damage factor increases as well. However, the critical location is still wrong. Also note that the nodes with damage factor of 0 doesn't necessarily show no damage at all. This could also result from a different element type.

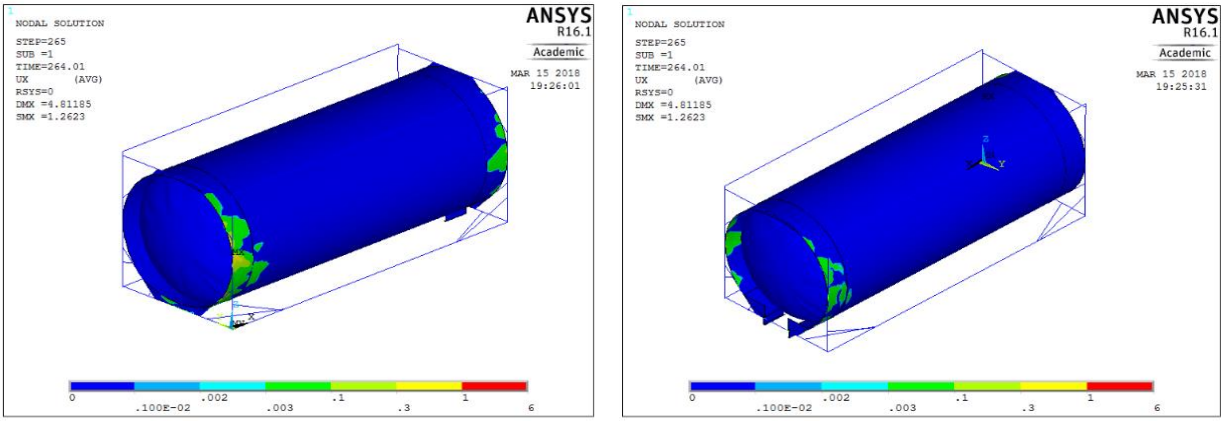

Figure 6- 7 Damage factor plot on model (front end vs rear end)

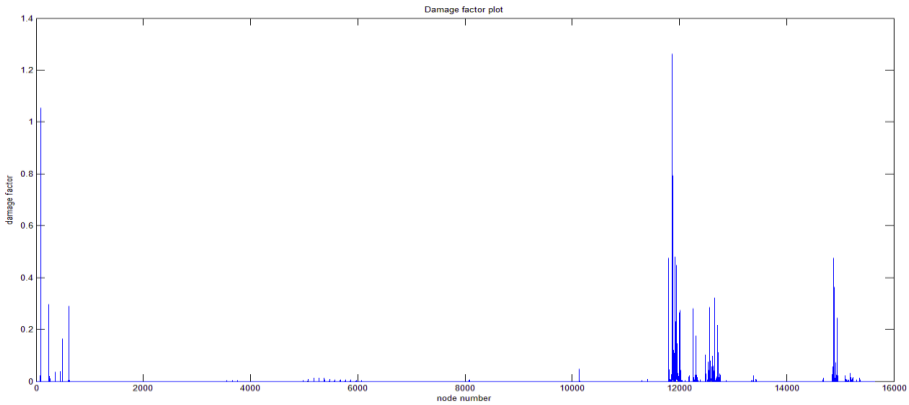

Figure 6- 8 Damage factor plot vs node number

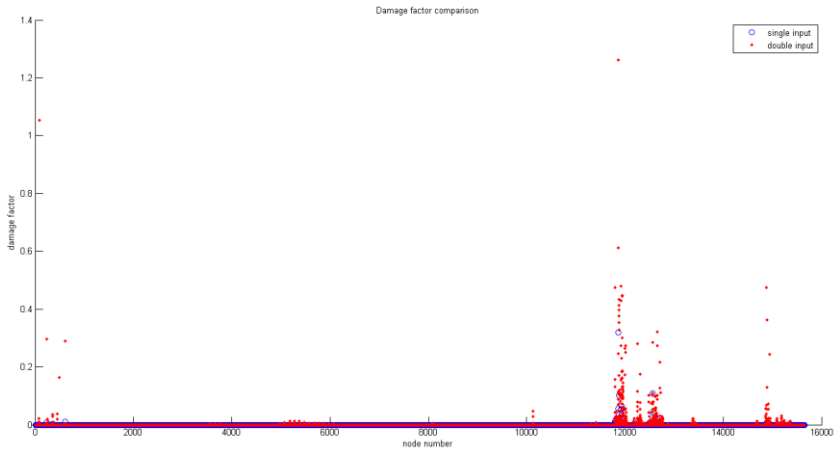

Figure 6- 9 Damage factor comparison between two inputs

6.4 Shifted loading calculation

Tanks containers are normally transported by gondola cars in railway transportation (figure 6-10). These gondola cars have proper dimensions so that tanks containers can be loaded and restrained properly. However, in reality, due to a lack of gondola cars, flat rail cars are often used in railway transportation of the containers (figure 6-11). Protrusions are often found along the width of flat cars, providing a different boundary condition for containers. When transported by gondola cars, containers are restrained properly on four corners. When flat railcars with humps are in use, additional supports are introduced to lateral frames on both front and rear end, while on the four corners, the constraints are loose, allowing the corners to move vertically. Such situation is called shifted loading. Trifleet Leasing is interested in the effect of shifted loading on both static falling calculation and quick calculation.

Figure 6- 10 Transportation of tank container by gondola car (normal loading)

Figure 6- 11 Transportation of tank container by flat car (shifted loading)

According to experience, the loaded area of shifted loading is considered to be 175mm to 250 mm away from the lateral center line of tank container. In FEM model, nodes within this area are selected on both ends. Then in quick calculation, the boundary condition become:

Within shifted loading area

$$Uz = 0;$$

At four bottom corners

$$Ux = 0$$
$$Uy = 0$$
$$Rotz = 0$$

In static falling calculation, nodes within this area of interest are selected and force acting on these nodes are calculated with respect to their distance to centerline and the equilibrium of force and moment. No restraints are on four corner bottoms.

Firstly, the calculation of shifted loading of static falling calculation is performed on the 26kl model developed by previous student. Information of this model is provided in chapter 6.2. The results are shown below.

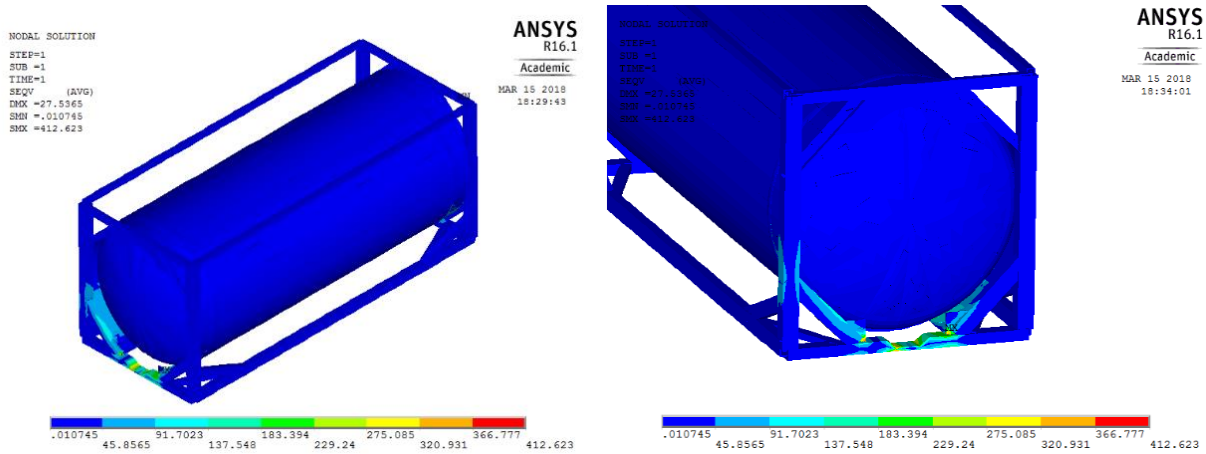

Figure 6- 12 Von Mises stress plot (shifted loading calculation)

Figure 6-12 shows that when the container is loaded with shifted loading, the area with maximum Von Mises stress shifts to the loaded area of shifted loading. This is because this shifted area become main source of restraint and stress naturally concentrate in this area. The stress level is much higher than normal loading, indicating that the shifted loading is more hazardous.

Then the calculation of shifted loading of quick calculation is performed on the same model with inputs from chapter 6.3. Results for single input is shown in figure 6-13. As loading shifts, the ‘critical area’ shifts as well. The new ‘critical spots’ are mainly around the flanges and connection of flanges and frames. The highest damage factor is 1.74, symbolizing that fatigue occurs. The overall trend matches with results from static loading. The accuracy still remains to be seen.

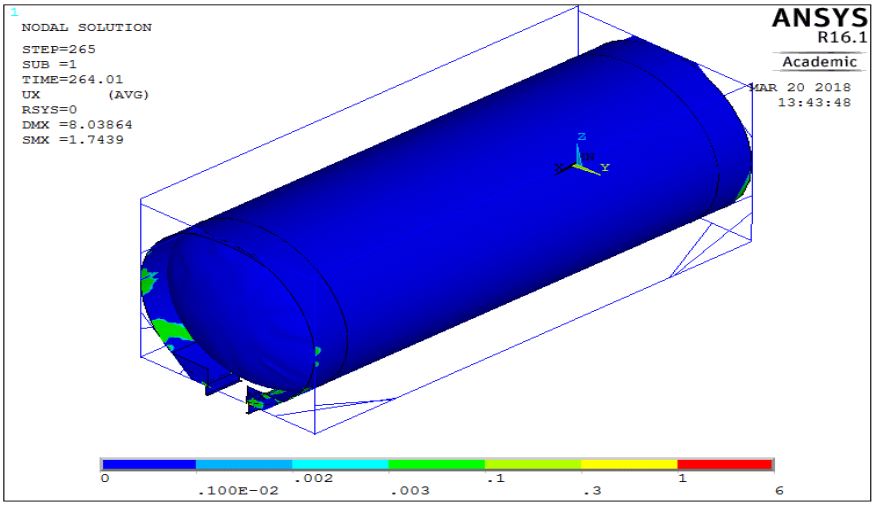

Figure 6- 13 Damage factor plot on model (single input shifted loading)

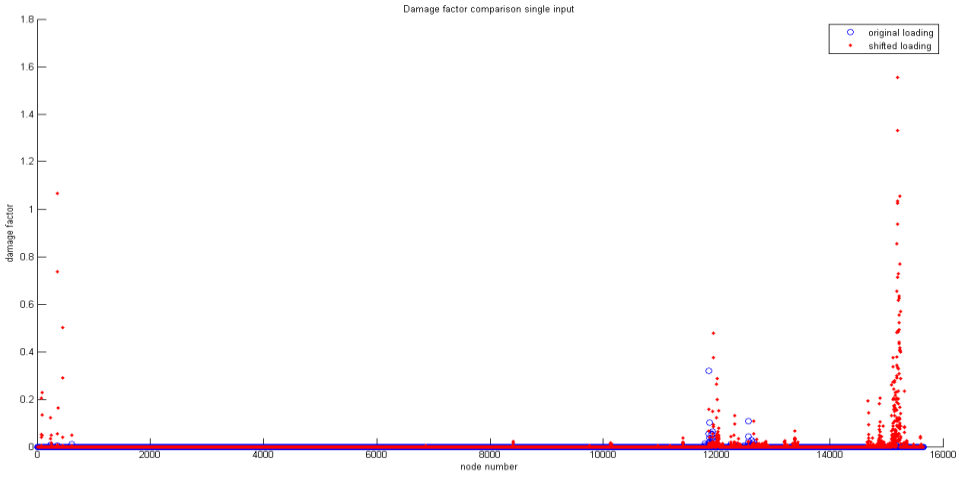

Figure 6- 14 Damage factor vs nodes comparison (single input)

Figure 6-14 compares the damage factor under two loading cases and single input. We can find that for nodes within the shifted loading area (node number 200-300, 12000-13000), as loading is shifted, stress level increases significantly, which is symbolized by an increment of damage factor. For nodes at other area, stress change isn't significant.

Then the same process is repeated for doubled input.

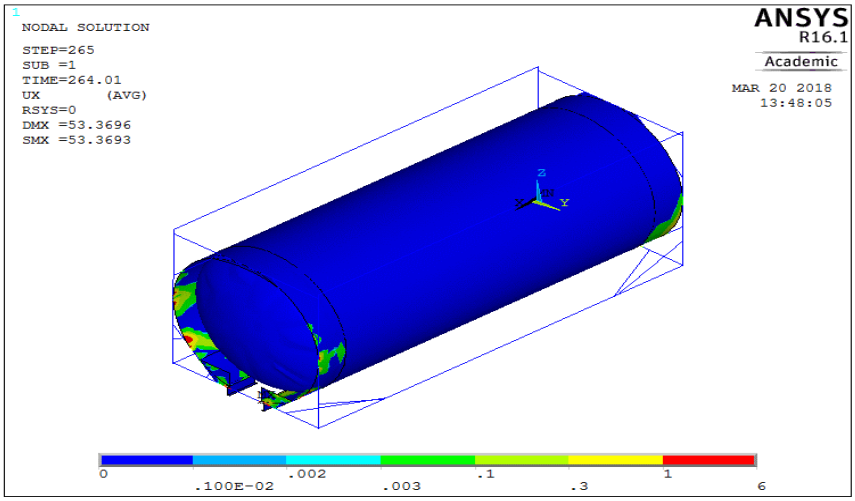

Figure 6- 15 Damage factor plot on model (double input shifted loading)

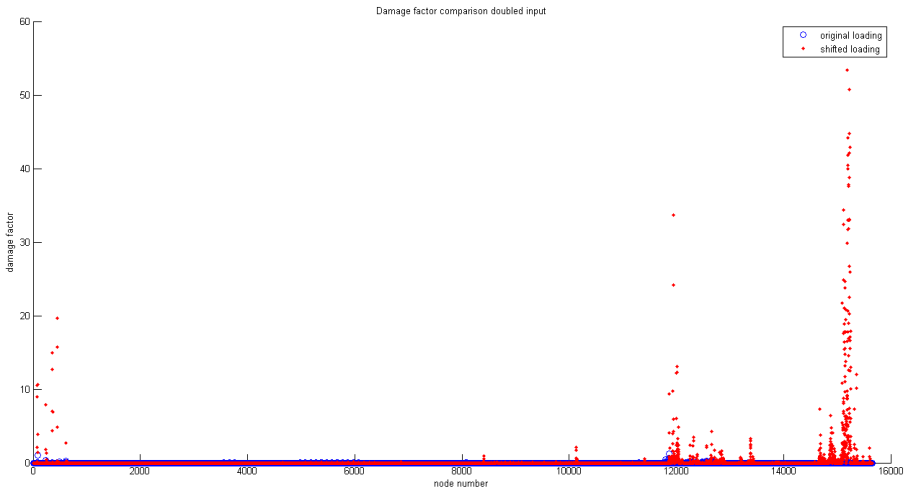

Figure 6- 16 Damage factor vs nodes comparison (single input)

Figure 6-16 shows a similar trend as figure 6-14. However, a damage factor of 53.37 is quite exaggerating. The critical area appears at the connection between skirts and frames. This error might result from two aspects. Firstly, different element types. To be specific, frames are modelled with beam elements while skirts are modelled by shell element. At the connection, due to different element properties, stress distribution is not continuous, which might cause a high stress level. Secondly, the choice of stress component. Since Von Mises stress is different from hot spot stress, under this circumstances, the difference between these stresses could be much larger. Therefore the fatigue damage factor in this section couldn't truly reflect the reality.

6.5 Recommendations for improvement

This study calculates the fatigue life of 26kl tank container with inputs from time domain. A few problems came up during the process and if some of them were solved in another way, the accuracy and applicability of the calculation could be improved. Thus a few recommendations are proposed for future improvement

The establishment of FE model

The validation of the calculation relies on the validation of the FE models. Results from chapter 4 shows that although the model is trustworthy in general, it is still far from perfection. For some static tests, the difference between FE calculation result and experiment is too large. One possible improvement is to set up the model without boolean operation. As it is shown in figure 5-6, a lot of odd-shaped elements are generated because of the boolean operation, which causes a lot of difficulty for meshing. When loaded with extreme loads, these odd-shaped elements will have high distortions that lead to failure of the calculations. Figure 6-17 shows the result of element check. Blue elements are acceptable while yellow elements are under warning. We can find that elements with warnings can be found at every connection. If the model is established completely with specified nodes and lines of specified length, the meshing would improve greatly, thus calculation with more severe situations can be performed. The accuracy of the calculations will improve as well.

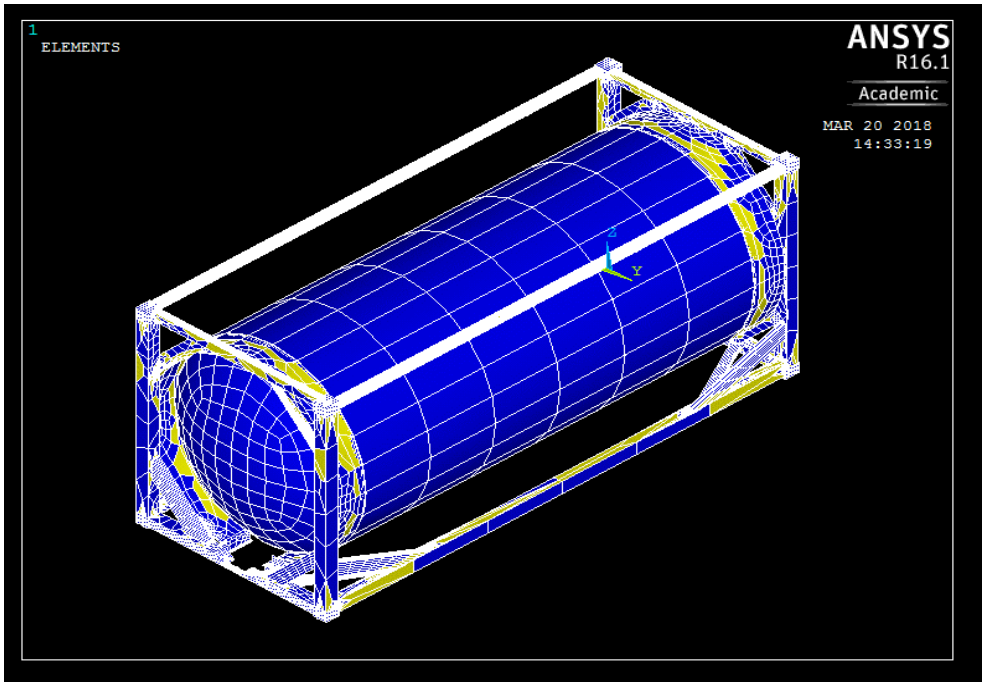

Figure 6- 17 Element status check

Transition between global model and local model

Another improvement can be made from the software package that is used to establish the models. To calculate fatigue life of tank container, one has to go through a transition from global model to local model. In ANSYS APDL, to find a perfect match of these two models, a lot of work has to be done manually (finding the matched nodes, export displacements from global model, import as boundary conditions for local model). This process can consume too much time and lead to inaccurate results. Therefore it is advised to use ANSYS Workbench instead because such steps are carried out automatically in that software. A better match of these two models will improve the accuracy of calculation greatly.

The domain of calculation

In this study, calculations are performed in the time domain. A transition from 5-minute input to 20-year estimation is achieved by random process and distribution of stress. However, the accuracy remains to be checked because a perfect estimation of stress distribution doesn’t exist and the random process can give an underestimation or overestimation of fatigue life. Therefore it is advised to carry out a calculation from frequency domain. In frequency domain, accelerations and stress for 5-minute and 20 year should give a higher resemblance. Calculation results can be more accurate and trustworthy.

Chapter 7 Appendix

7.1 Fatigue damage calculation on other lines

7.1.1 Hotspot 2 and Line 2

Hotspot 2 is located at the weld toe of the welding connecting the skirt and the vessel. This part is at the left bottom side of discharge area. Line 2 starts with hotspot 2 and it is parallel to the flange length. Nodes are selected at 0.4t, 1.0t and 1.4t away from the weld toe. The location of line 2 in global mode and local model are shown in figure 7-1

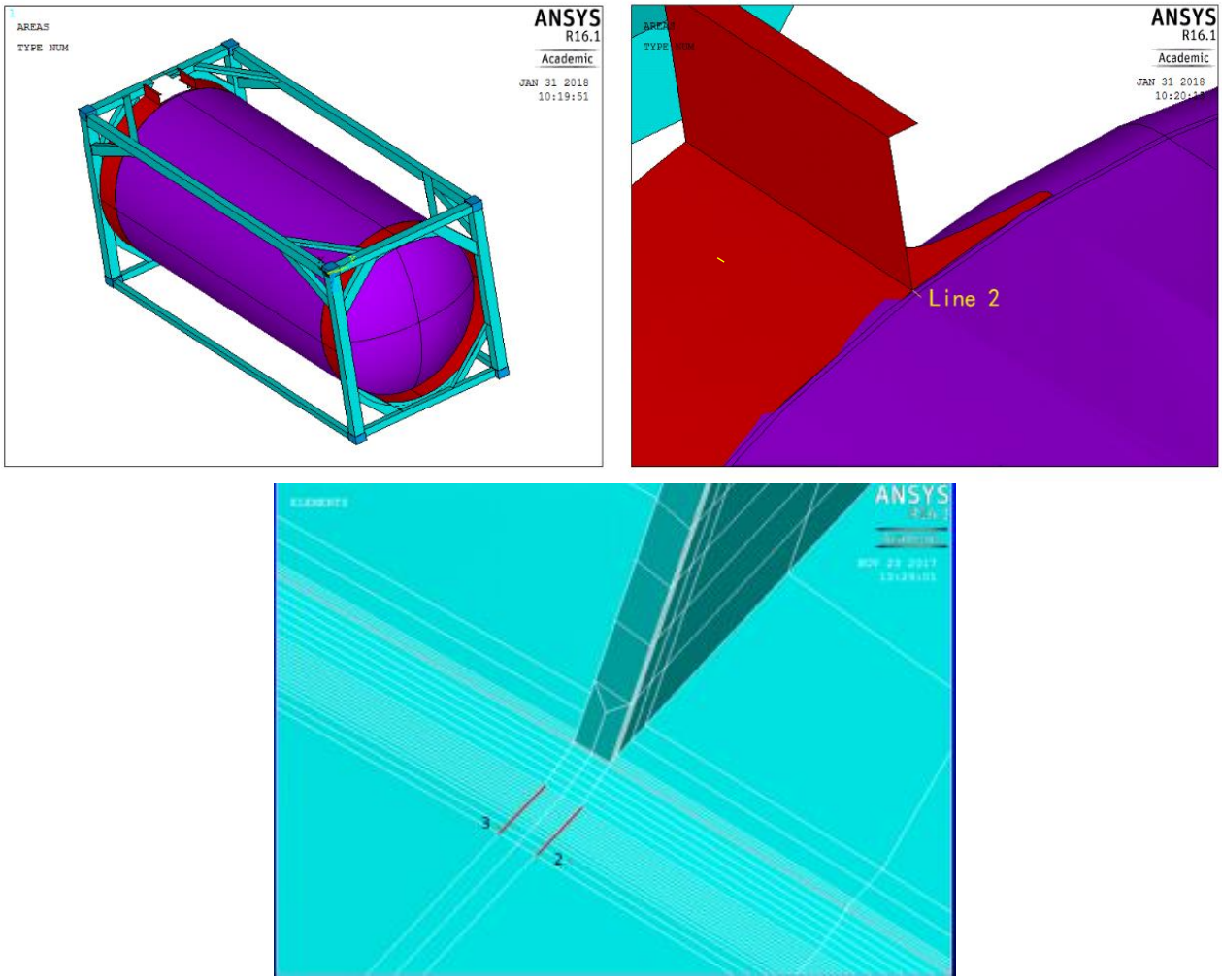

Figure 7-1 a) Bottom view of the global model
b) Location of line 2 in global model
c) Location of line 2 in local model

The analysis result is shown below

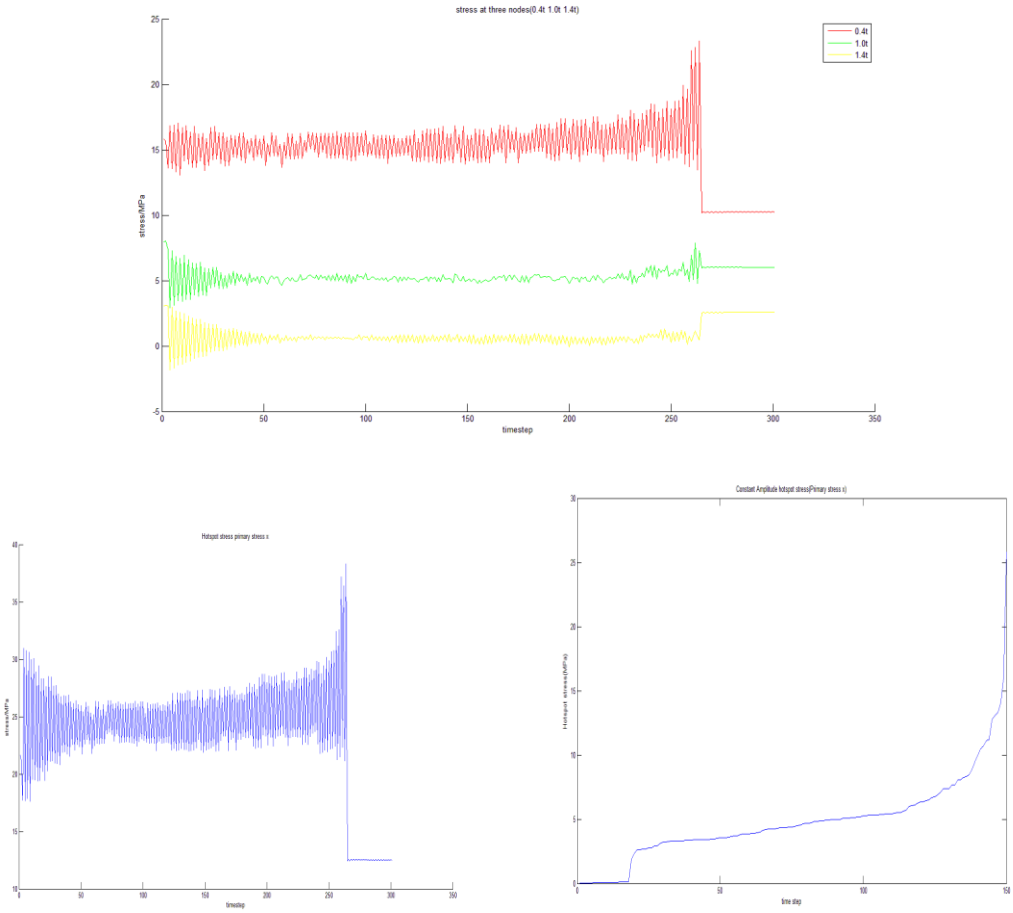

Figure 7-2 a) Primary stress at 0.4t, 1.0t, 1.4t (line 2)
b) Variable amplitude hotspot stress (line 2)
c) Constant amplitude hotspot stress (line 2)

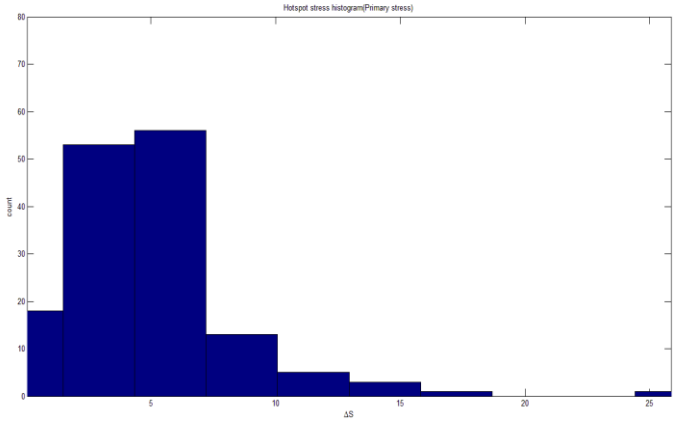

Figure 7-3 Histogram of CA hotspot stress (line 2)

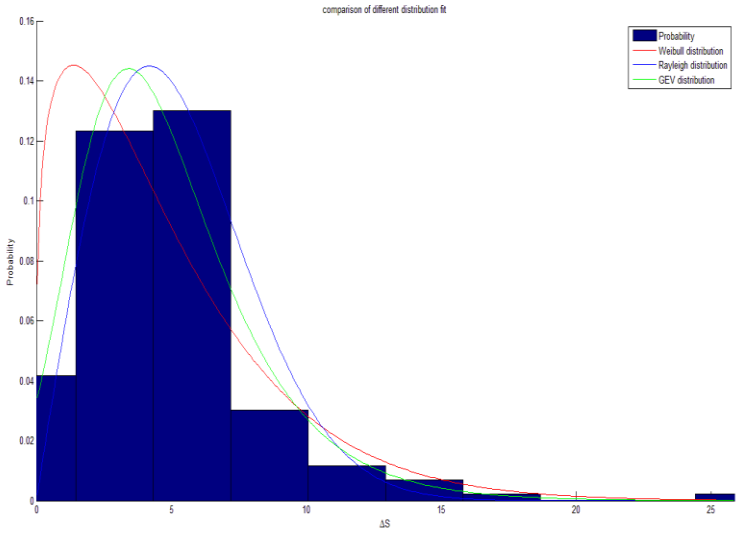

Figure 7-4 Comparison of PDF function

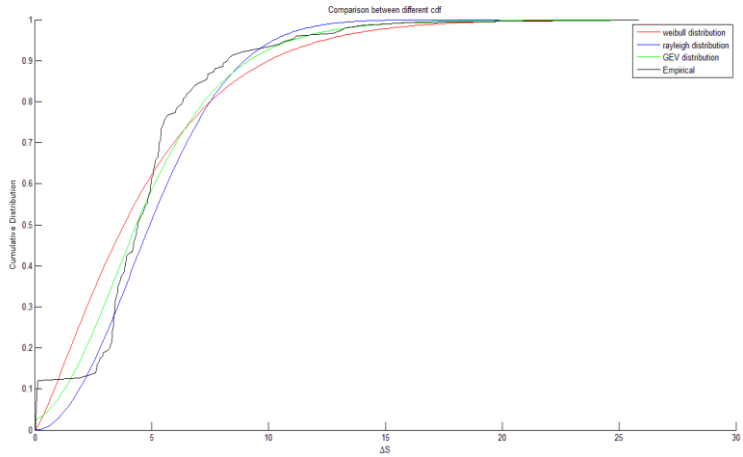

Figure 7-5 Comparison of CDF function

	Direct fitting	Random process fitting
Rayleigh distribution	0	0
GEV distribution	3.88e-4	0
Weibull distribution	0.0014	0

Table 7-1 List of damage factor (hotspot 2)

Figure 7-3 shows that the majority of the stress level is in low amplitude phase. Figure 7-2 shows that the maximum hotspot stress for the 5-minute input is 25MPa, which is lower than the cut-off limit. Thus we expect very little or zero damage at hotspot 2. From figure 7-4 and figure 7-5 shows that generalized extreme distribution is a better fit for the stress history. For high amplitude stress, Weibull distribution gives a relatively higher probability of occurrence while Rayleigh distribution gives a lower estimation. Therefore calculation result from GEV distribution is considered as trustworthy and the total damage along line 2 is 3.88e-4, which means no damage is generated at hotspot 2 within 20 years.

7.1.2 Hotspot 3 and Line 3

Hotspots are chosen at locations where there is a change of geometry. Hotspot 3 is adjacent to hot spot 2. It is also located at the weld toe of the welding connecting the skirt and the vessel. This part is at the left bottom side of discharge area. Line 3 starts with hotspot 3 and it is parallel to line 2. It is at the other side of the flange. Nodes are selected at 0.4t, 1.0t and 1.4t away from the weld toe. The location of line 3 in global mode and local model are shown in figure 7-6

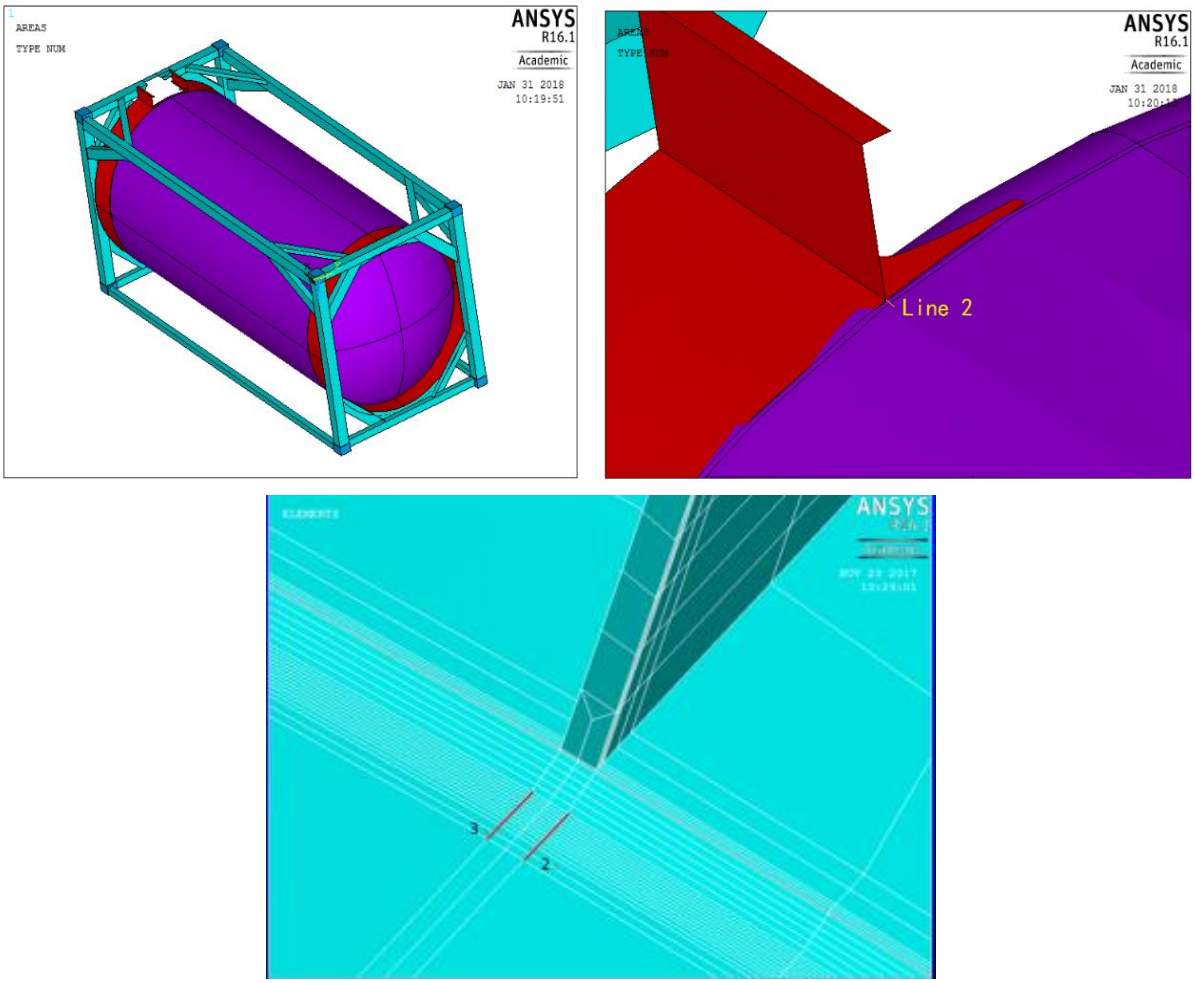

Figure 7-6 a) Bottom view of the global model
b) Location of line 3 in global model
c) Location of line 3 in local model

The analysis result is shown below

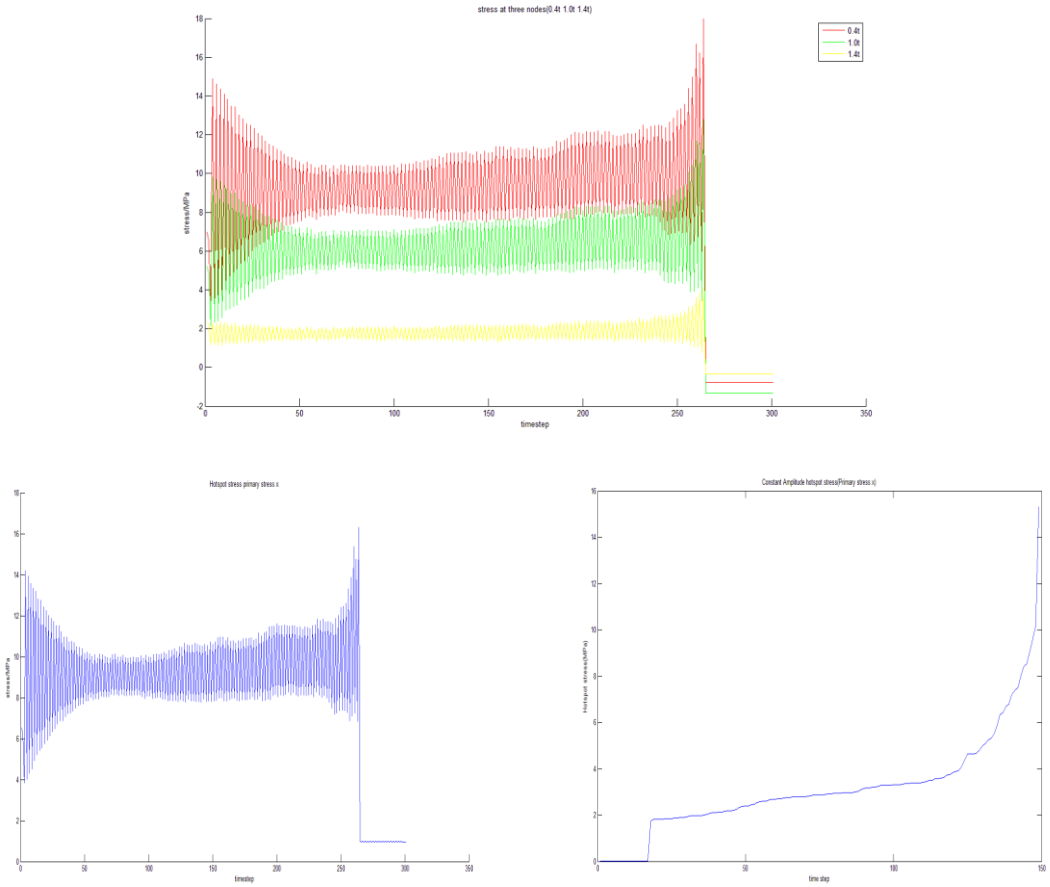

Figure 7-7 a) Primary stress at three nodes (line 3)
b) Variable amplitude hotspot stress (line 3)
c) Constant amplitude hotspot stress (line 3)

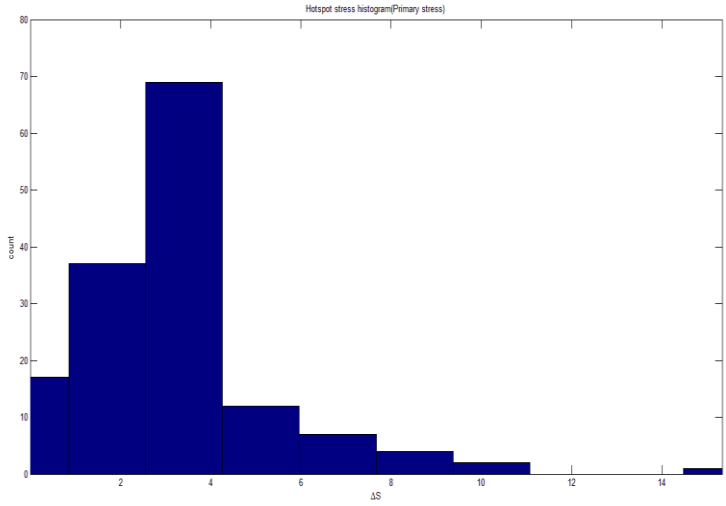

Figure 7-8 Histogram of CA hotspot stress (line 3)

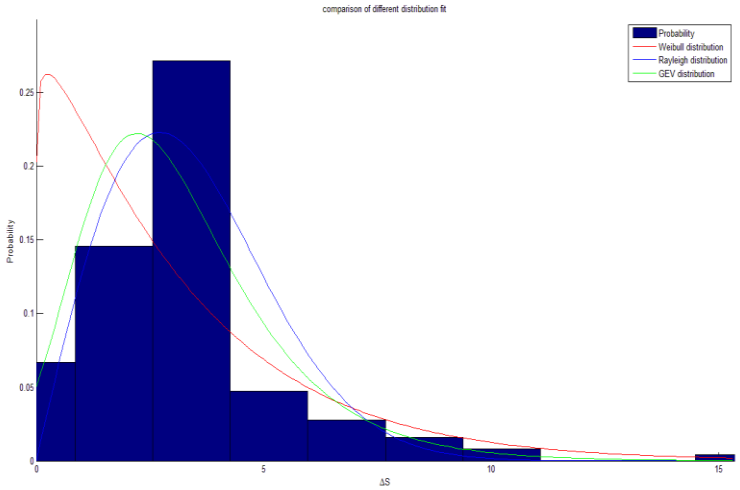

Figure 7-9 Comparison of PDF function

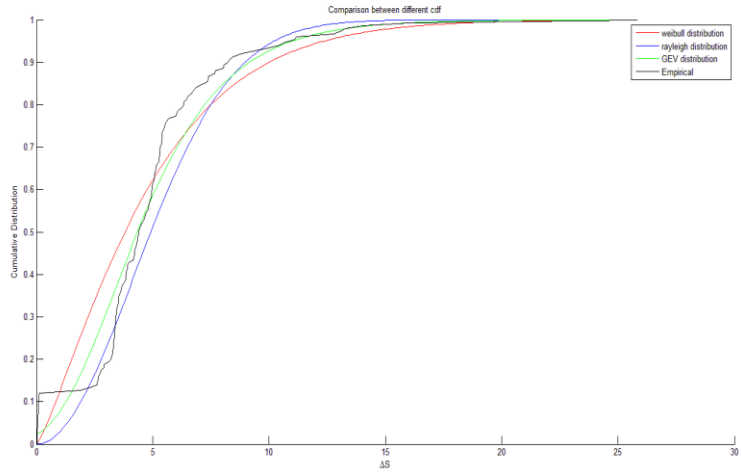

Figure 7-10 Comparison of CDF function

	Direct fitting	Random process fitting
Rayleigh distribution	0	0
GEV distribution	1.46e-6	0
Weibull distribution	2.27e-3	6.53e-4

Table 7-2 list of damage factor (hotspot 3)

Similar to the situation at hotspot 2, stress level concentrate in the low amplitude phase. Figure 7-9 shows that Weibull distribution is inaccurate in low amplitude phase and too optimistic in high amplitude phase. Raleigh distribution gives a relatively low estimation of high level stress. Thus calculation with GEV distribution is considered as trustworthy and the final damage is 1.46e-6, which means no damage is done at hotspot 3.

7.1.3 Hotspot 4 and Line 4

Hotspots are chosen at nodes where there is a change of geometry. Hence hotspot 4 is chosen at the edge of the local model. To be specific, this part is at the left of discharge area. Line 3 lies at the connection of the skirt and vessel. Nodes are selected at 0.4t, 1.0t and 1.4t away from the weld toe. This line looks horizontal but in fact, due to the slope and curvature of the surface, it is not horizontal. The location of line 4 in global mode and local model are shown in figure 7-11

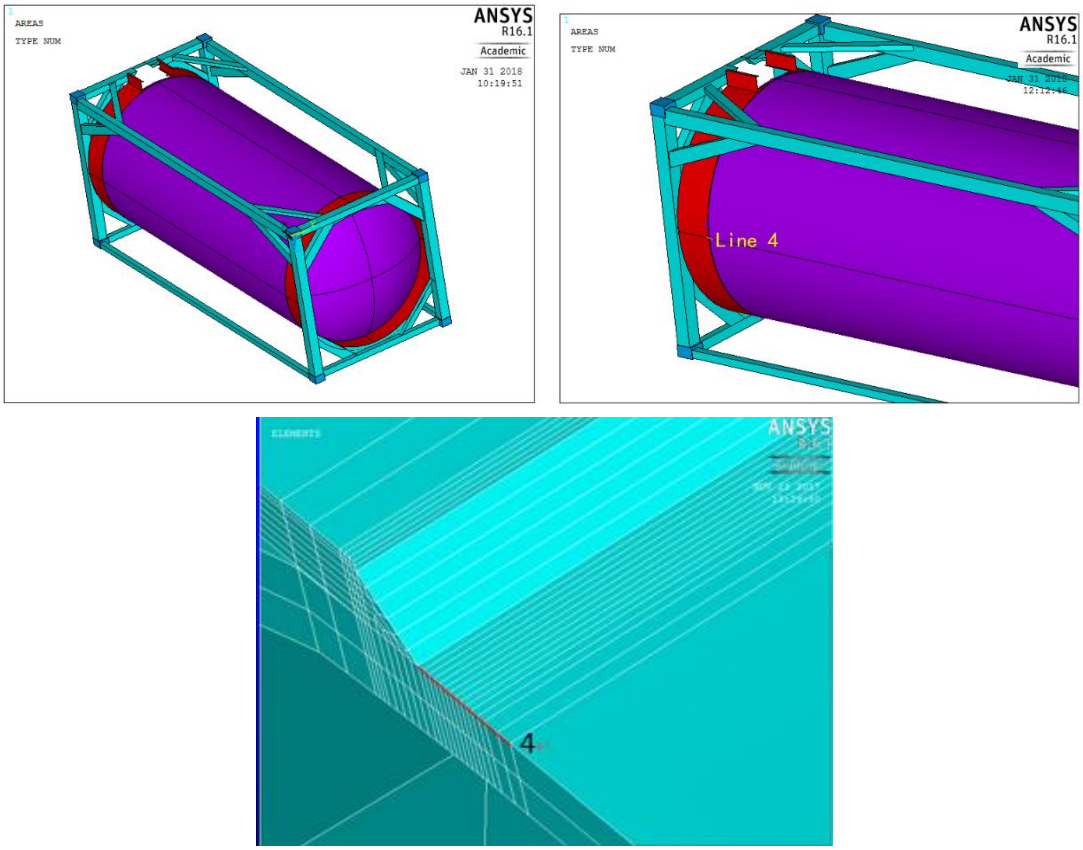

Figure 7-11 a) Bottom view of the global model
b) Zoomed-in view of location of line 4 in global model
c) Location of line 4 in local model

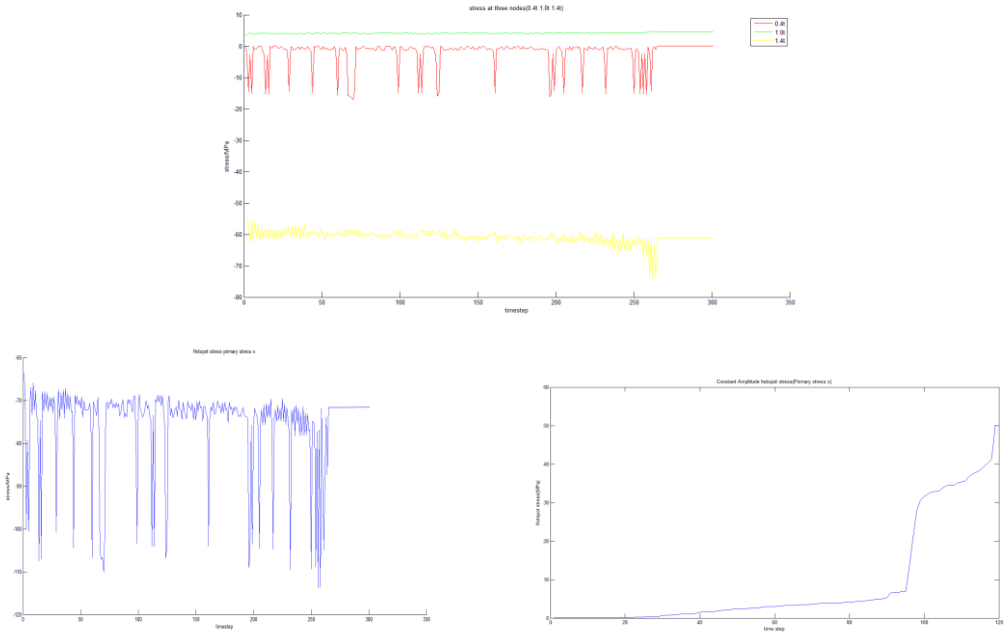

Figure 7-12 a) Primary stress at three nodes (line 4)
b) Variable amplitude hotspot stress (line 4)
c) Constant amplitude hotspot stress (line 4)

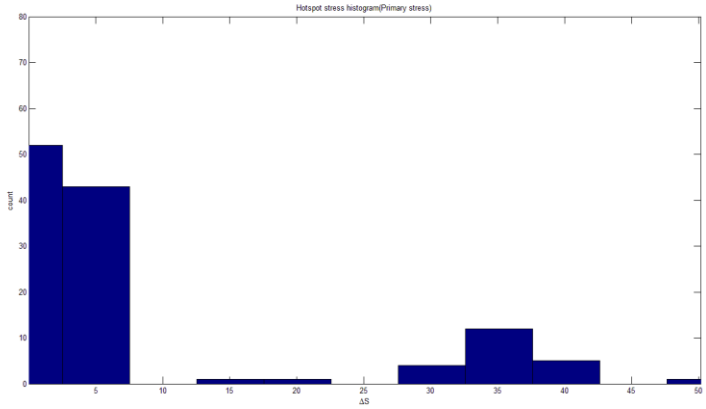

Figure 7-13 Histogram of CA hotspot stress (line 4)

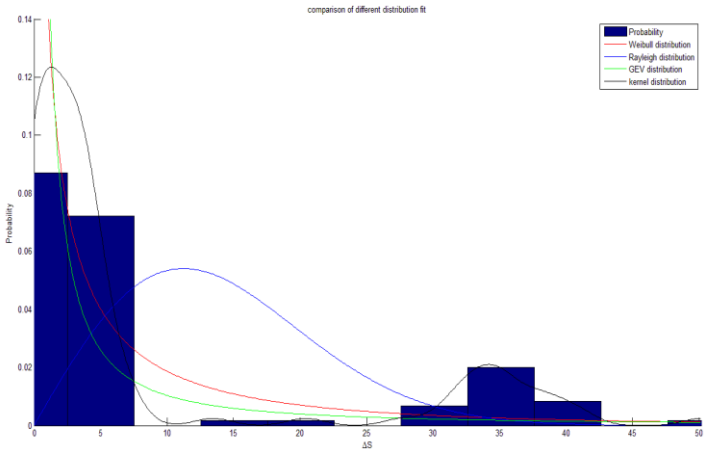

Figure 7-14 Comparison of PDF function

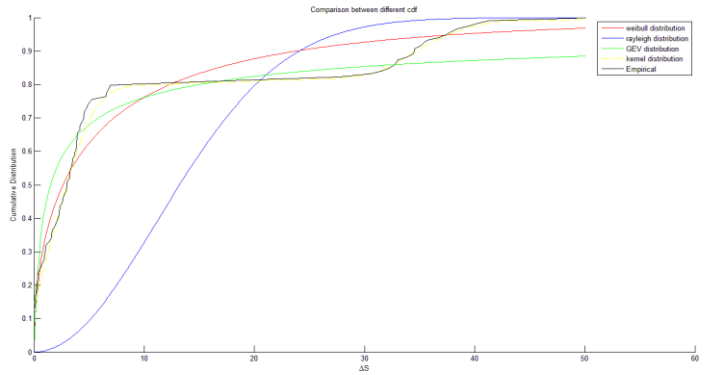

Figure 7-15 Comparison of CDF function

	Direct fitting	Random process fitting
Rayleigh distribution	0.1931	1.4e-4
GEV distribution	15.06	0.78
Weibull distribution	2.52	1.57e-4
Kernel distribution	1.11	0.2028

Table 7-3 List of damage factor (hotspot 4)

Due to the absence of material in the local model, the stress at hotspot 4 shows a different trend. The majority of the stress levels are in either low stress phase or high stress phase. Therefore kernel distribution is applied to reach a better fitting of the probability density function. Figure 7-14 and 7-15 supports this idea. The maximum constant amplitude hotspot stress is 50MPa and about 20% of all stress levels are above the cut-off limit. Thus we expect some damage at this hotspot. After kernel distribution fitting, the damage factor is 1.11, which is above 1. The conclusion is fatigue damage will occur at hotspot 4

7.1.4 Hotspot 5 and Line 5

Hotspot 5 is located at the weld toe of the welding connecting the skirt and the vessel. This part is at the left bottom side of discharge area. This hotspot is close to hotspot 1 but the orientation of line 5 is different from line 1. Due to the curvature of the surface, line 5 is not completely lateral. The location of hotspot 5 and orientation of line 5 are shown in figure 7-16

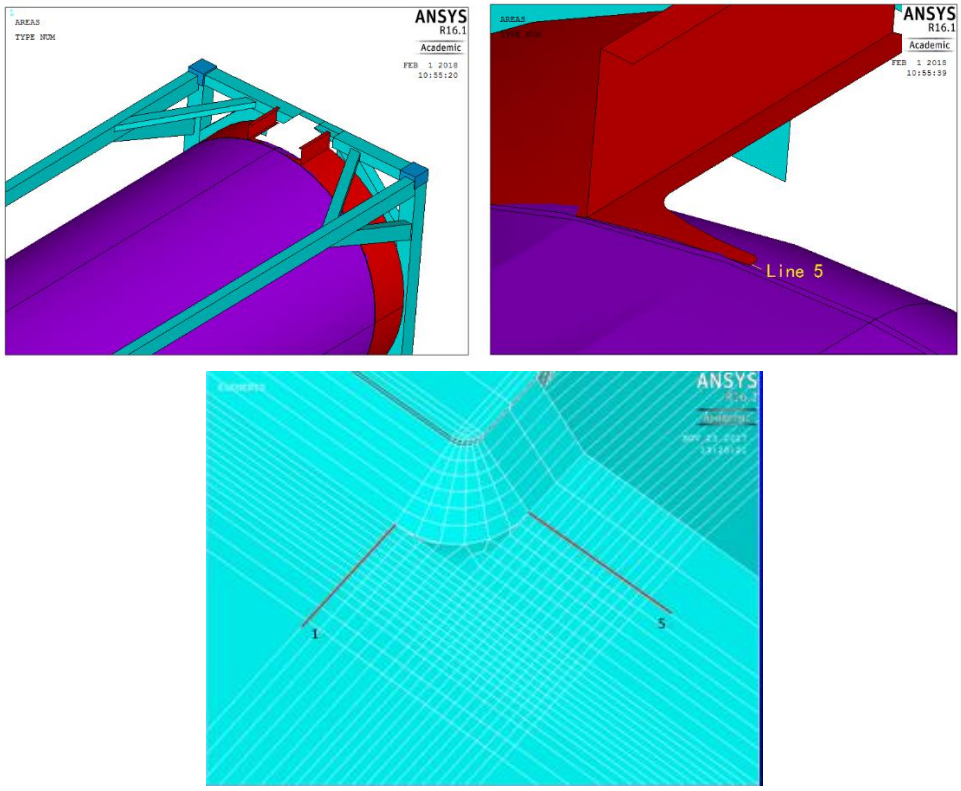

Figure 7-16 a) Bottom view of the global model
b) Zoomed-in view of location of line 5 in global model
c) Location of line 5 in local model

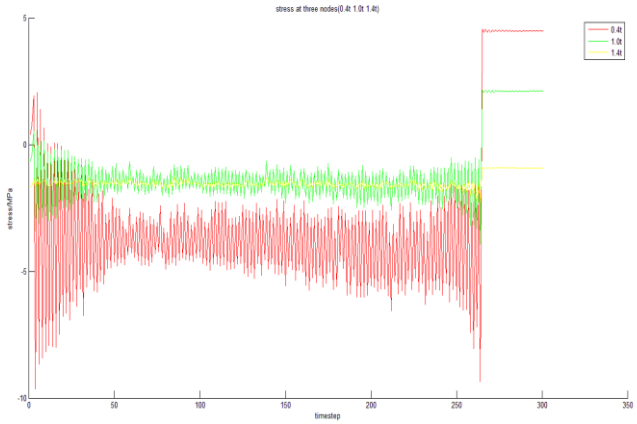

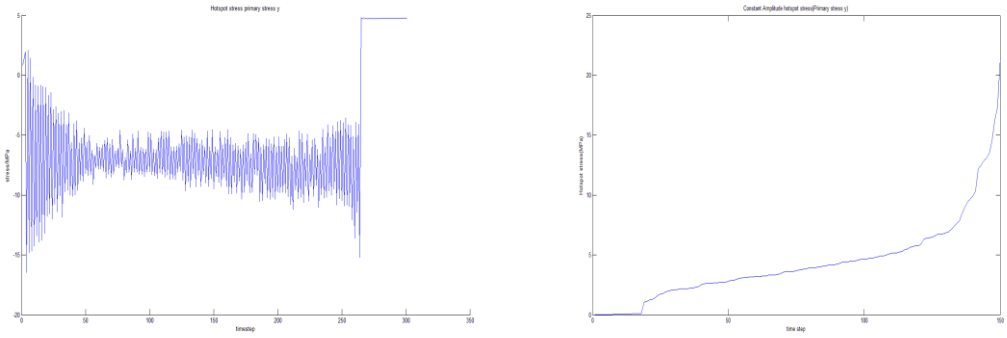

Figure 7-17 a) Primary stress at three nodes (line 5)
b) Variable amplitude hotspot stress (line 5)
c) Constant amplitude hotspot stress (line 5)

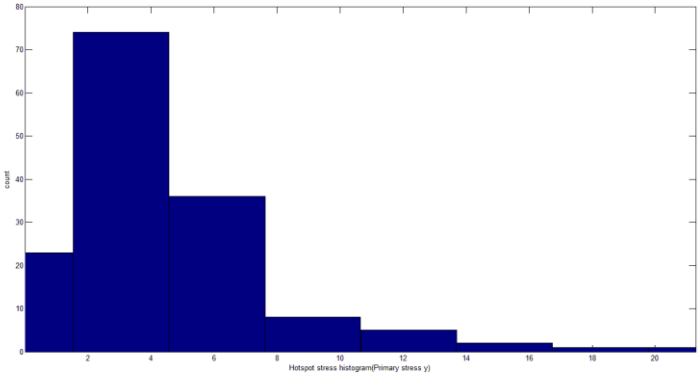

Figure 7-18 Histogram of CA hotspot stress (line 5)

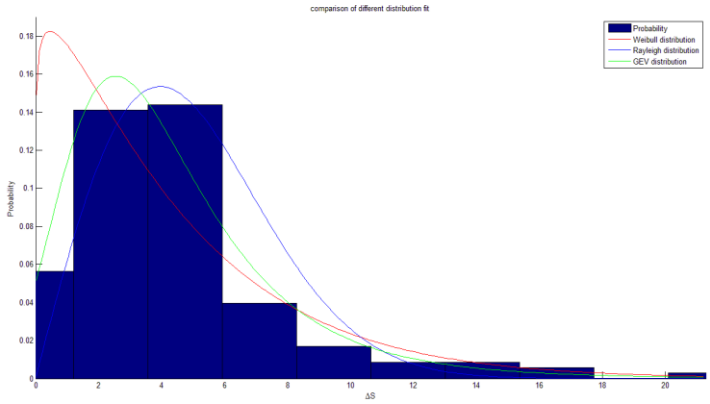

Figure 7-19 Comparison of PDF function

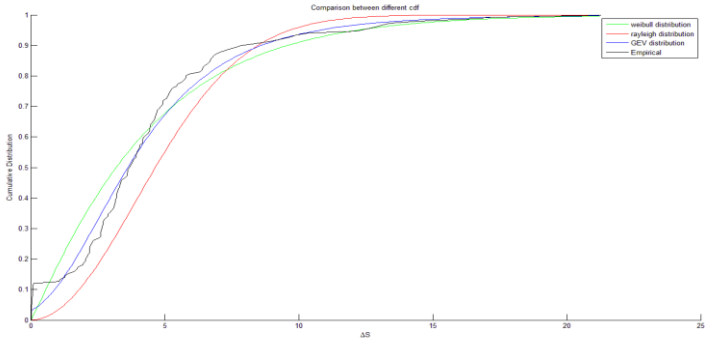

Figure 7-20 Comparison of CDF function

	Direct fitting	Random process fitting
Rayleigh distribution	0	0
GEV distribution	3.9e-3	0
Weibull distribution	0	2.19e-4

Table 7-3 List of damage factor (Hotspot 5)

Figure 7-19 and figure 7-20 shows result calculated with GEV distribution is more trustworthy. Therefore the fatigue damage is 3.9e-3, which implies no fatigue damage is caused at hotspot 5

Bibliography

American Bureau of Shipping (ABS). (1992). *Guide for fatigue strength assessment of tankers, Part 3 Steel Vessel Rules.* New York.

ASTM. (2005). *Standard Practices for Cycle Counting in Fatigue Analysis.* ASTM International.

BestendenJ.H. (2015). fatigue resistance of welded joints in aluminium high-speed craft: A TOTAL STRESS CONCEPT. Enschede, The Netherlands: Gildeprint.

Det Norske Veritas(DNV). (2008). *Fatigue Design of Offshore Steel Structures. Recommended Practice DNV-RP-C203.* Det Norske Veritas.

Fricke, W., Petershagen, H., & Paetzold, H. (1998). *Fatigue Strength of Ship Structures-Expample.* Hamburg, Germany.

G. Glinka, J. (1987, October). Rainflow counting algorithm for very long stress histories. *International Journal of Fatigue*, pp. 223-228.

HobbacherA. (2008). RECOMMENDATIONS FOR FATIGUE DESIGN OF WELDED JOINTS AND COMPONENTS. International Institute of Welding.

Karamanosa, S. A., Romeijn, A., & Wardenier, J. (2002). SCF equations in multi-planar welded tubular DT-joints including bending effects. *Marine Structures 15 (2002)*, 161.

Lloyd's Register SHI0816414 . (2008). *Prototype Test Report ISO Series 1 Containers(Form FC3).*

Rainflow-counting algorithm. (2017). Retrieved from https://en.wikipedia.org/wiki/Rainflow-counting_algorithm

Rajib Ul Alam UzzalAhmed and Subhash RakhejaWaiz. (December 2008). DYNAMIC ANALYSIS OF RAILWAY VEHICLE-TRACK INTERACTIONS DUE TO WHEEL FLAT WITH A PITCH-PLANE VEHICLE MODEL. Journal of Mechanical Engineering, Vol. ME39, No. 2.

Schijve, J. (2009). *Fatigue of Structures and Materials.* Springer Science+Business Media, B.V.